TECHNISCHE UNIVERSITÄT
BERGAKADEMIE FREIBERG
The University of Resources. Since 1765.

Faculty 3: Faculty of Geosciences, Geoengineering and Mining
Institute of Geophysics and Geoinformatics

Master Thesis

A thesis submitted in partial fulfillment of the requirements for the degree of Master of Science (M.Sc.)

Integrated Borehole Geophysics at the Kimberly borehole, ICDP Project HOTSPOT, Idaho

Franziska Naumann

Master of Science in Geophysics
Matriculation register: 53019

3rd December 2015

Topic registered on: 1st March 2015
Tutor/First Proofreader: Prof. Dr. Stefan Buske
TU Bergakademie Freiberg
Institute of Geophysics and Geoinformatics
Gustav-Zeuner-Str. 12
D-09596 Freiberg
Second Proofreader: Prof. Dr. Douglas R. Schmitt
Department of Physics
University of Alberta
Edmonton AB T6G 2E1
Canada

Abstract

The study area in the Twin Falls volcanic center is known for its high heat flow and geothermal gradient; therefore, the goal is to investigate the geothermal potential primarily with geophysical methods. To image the successive volcanism of the Snake River Plain, representative drill sites are selected. Using a 1.96 km deep borehole located in the town of Kimberly, Idaho, geophysical borehole logs, zero-offset and walk-away vertical seismic profiles are acquired to assess the hydrogeological boundaries of the volcanic province.

Borehole logs assist with subsurface rock characterization, determination of types and depth of fractures and the analysis of in-situ physical rock properties to support previous lithologic results. The geophysical well logs have been used to correlate the response of the physical properties with the correspondent rock type. Sondes, which measure the natural and spectral gamma radiation, magnetic susceptibility and neutron counts proved to be particularly helpful to differentiate between basalt, sediment and three rhyolite units in depth. Another attempt was the detection of fractures with logging tools like the dual laterolog, the borehole televiewer, the full waveform sonic and the caliper. In conjunction with core scans a large number of natural fractures have been discovered. The comprehensive analysis of all logs shows natural fractures or brittle zones for the deepest rhyolite unit between 605 and 1956 m depth. According to the present knowledge fractures are open and are associated with high porosity rock. However, no evidence could be found for drilling induced fractures and borehole breakouts at the Kimberly borehole. Temperatures measurements reveal a significant zone of possible water accumulation that is associated with the Snake River Aquifer. Although temperatures at depth are, according to the current knowledge, too low for geothermal power generation, a calculation of radiogenic heat productions offers a promising view.

The objectives of the seismic measurements at the Kimberly borehole are the correlation of reflections with geologic features near the borehole. For this, a vibroseis source was stationed with a 17 m offset close to the borehole while lowering the receivers in the well. Processing of the zero-offset seismic section included, in addition to the wavefield separation, an analysis on primary and multiple seismic events. Primary reflections are associated with a change in rock formation and therefore flow boundaries can be imaged.

The second type of vertical seismic profile that was acquired with sources along a line near the borehole was a walk-away VSP. For 8 different receiver depths large lateral velocity changes are observed, which make it necessary to apply static corrections.

Kurzfassung

Das Untersuchungsgebiet in der vulkanischen Umgebung von Twin Falls ist bekannt für seinen hohen Wärmefluss und geothermischen Gradienten; das Ziel stellt daher die Untersuchung des geothermischen Potentials mit Hilfe von geophysikalischen Methoden dar. Um den sukzessiv verlaufenden Vulkanismus der Snake River Plain abzubilden, wurden charakteristische Bohrstandorte ausgewählt. Mit Hilfe eines 1.96 km tiefen Bohrlochs, welches sich in der Stadt Kimberly, Idaho befindet, wurden geophysikalische Bohrlochmessdiagramme, Zero-offset und Walk-away vertikale seismische Profile erfasst um hydrogeologische Schichtgrenzen der vulkanischen Provinz in der Tiefe abzuschätzen.
Die Bohrlochmessdiagramme sollen bei der Charakterisierung der Gesteine im Untergrund, bei der Bestimmung von Arten und Tiefen von Kluftzonen und bei der Analyse von in-situ physikalischen Gesteinseigenschaften helfen um bereits bekannte lithologische Erkenntnisse zu unterstützen. Die geophysikalischen Bohrlochmessungen wurden genutzt um die Resonanz aus den Diagrammen mit den physikalischen Eigenschaften des Untergrundes zu korrelieren. Sonden, welche die natürliche sowie die spektrale Gamma Strahlung, die magnetische Suszeptibilität und die Neutronenanzahl messen, erwiesen sich besonders hilfreich bei der Unterscheidung zwischen den geologischen Einheiten Basalt, Sediment und Rhyolith. Ein weiterer Versuch schloss die Detektierung von Kluftzonen mit Bohrlochmesssonden wie dem Dual Laterolog, dem akustischen Bohrlochfernseher, dem Akustiklog und dem Kaliber ein. In Verbindung mit den Bohrkernbildern konnte eine große Anzahl an natürlich vorkommenden Kluftzonen und Rissen bestimmt werden. Die umfassende Analyse aller Bohrlochmessungen wies auf natürlich vorkommenden Kluftzonen und aufgelockerte Bereiche in der tieften Rhyolitheinheit zwischen 605 und 1956 m Tiefe hin. Nach jetztigen Kenntnisstand sind diese Kluftzonen offen und stehen in Verbindung mit hoch porösen Gestein. Allerdings konnten keine Hinweise auf Kluftzonen gefunden werden, die durch Bohrprozesse entstehen, oder die auf stärke Ausbrüche an der Bohrlochwand hinweisen. Temperaturmessungen deuten auf eine besondere wasserführende Zone hin, die mit dem Snake River Aquifer in Verbindung steht. Obwohl die Temperaturen in der Tiefe, nach jetztigen Kenntnisstand, zu niedrig für die geothermische Stromproduktion sind, verbirgt sich hinter der Berechnung der radiogenen Wärmeproduktion ein zuversichtlicher Ausblick hinsichtlich der bereitgestellten Wärme aus der Tiefe.
Das Ziel der seismischen Messungen in der Nähe des Kimberly Bohrlochs ist es die seismischen Reflektionen mit geologischen Merkmalen zu verknüpfen. Hierfür wurde eine Vibrosseis Quelle in einer Entfernung von 17 m vom Bohrloch positioniert, währenddessen die Empfänger im Bohrloch versenkt wurden. Die Prozessierung der Daten des Zero-offset vertikalen seismischen Profils schloss neben der Wellenfeldseparation auch die Analyse von primären und multiplen seismischen Ereignissen ein. Die primären Reflektionen können Änderungen der Gesteinsformation zugeordnet werden und helfen bei der Kartierung vulkanischer Fließeinheiten.
Der zweite Typ des vertikalen seismischen Profils, das Walk-away VSP, wurde entlang einer Strecke mit mehreren Qullen nahe des Bohrlochs durchgeführt. Für acht unterschiedliche Empfängertiefen wurden große laterale Geschwindigkeitsänderungen beobachtet, die einer statischen Korrektor unterzogen werden müssen.

Acknowledgements

First of all, I would like to thank my supervisor Prof. Dr. Douglas Schmitt for giving me the opportunity to come to the University of Alberta and get involved in such a great project. Through the stay in Edmonton, I have gained invaluable experience for my professional career. Thank you for your guidance and the continuous help during this study.

Special thanks also goes to my supervisor Prof. Dr. Stefan Buske, who guided this work with important scientific recommendations and imparted a broad knowledge of seismic during his teaching.

I want to thank the German Academic Exchange Service (DAAD) for providing me with the PROMOS scholarship, which allowed me to travel to Canada and let me gain this research experience. Furthermore, I would like to thank the National Scholarship Program of Germany (Deutschlandstipendium) for their financial support.

I would like to acknowledge GEDCO for providing the VISTA^{TM} seismic data processing software package, Advanced Logic Technology (ALT) for supplying the WellCAD software package, and GeoTomo for implementing with their Tomoplus package a traveltime tomography solution for the near-surface data of the Kimberly drill site.

Thank you Mom and Dad, for supporting me in this stage of my life, without the love and faith you put in me, I would not have come that far. You supported me by all means and acted always selflessly.
Special thanks go to my beloved fiancé, who always believed and encouraged me. Thanks for being so patient, you compromised so much during the last years of my studies.

Contents

List of Figures

List of Tables

Abbreviations, Acronyms and Symbols

α	Spreading angle
β	Direction angle
$\vec{H}$	Horizontal component of field vector (direction magnetic N)
λ	Thermal conductivity
$\vec{M}$	Induced magnetization
Φ	Porosity
χ	Magnetic susceptibility
$\vec{T}$	Earth total magnetic field vector
ρ	Rock density
τ	measurement period (time window)
τ-p	Radon transform
q	Heat flow
$\vec{Z}$	Vertical component of field vector
3-C	Three-component
A	Radiogenic heat production
API	American Petroleum Institute
c	concentration
Ca	Calcium
CALI (or CAL)	Caliper
cps	Counts per second
d	Diameter of the borehole
d_i	Invaded depth
DIP	Dipmeter
DIF	Drilling induced fracture
DLL	Dual laterolog
DOE	U.S. Department of Energy
DOSECC	Drilling, Observation and Sampling of the Earths Continental Crust
ESPA	Eastern Snake River Plain Aquifer or Eastern Snake River Aquifer
ESRP	Eastern Snake River Plain
FAC40 (or BHTV)	Televiewer, acoustic images
f_G	Frequency generator
f-k	temporal frequency - spatial frequency (frequency-wavenumber)
FWS	Full waveform sonic
GFZ	GeoForschungsZentrum
GR	Gamma ray
HMAX	Horizontal radial coomponent
HMIN	Horizontal transverse component
I	Inclination angle
ICDP	International Continental Scientific Drilling Program
J	Pseudogeometric factor

K	Potassium
ka	Thousand years
KB	Kelly bushing
K-L	Karhunen-Loeve
L	coil
LLD	Deeper laterolog measurement of the dual laterolog tool
LLS	Shallow laterolog measurement of the dual laterolog tool
Ma	Million years
masl	Meters above sea level
MSUS (or MS)	Magnetic susceptibility
N	Pulse rate
OSG	Operational Support Group
Pb	Lead
ppm	Parts per million
R	Resistivity
R_a	Apparent resistivity
R_t	True formation resistivity of non-invaded zone
R_{xo}	Resistivity of the invaded zone
SEG-Y	file format for storing geophysical data
SGR	Spectral gamma ray
SRP	Snake River Plain
SRSDP	Snake River Scientific Drilling Project
SRVP	Snake River Volcanic Province
SV	Vertically polarized shear wave
T	Temperature
t	Travel time
-TT	Time-alignment of VSP data along first-breaks
+TT	Time-alignment of VSP data along upgoing events
T_f	Formation temperature
T_m	Mean surface temperature
Th	Thorium
Δt	Interval travel time
U	Uranium
U.S. EPA	United States of America Environmental Protection Agency
USGS	United States of America Geological Survey
U of A	University of Alberta, Canada
$v_{Formation}$	Formation velocity
v_{fl}	Velocity of pore fluid
V_p	P-wave velocity
V_s	S-wave velocity
VSP	Vertical Seismic Profiling
VSP-CDP	VSP common depth point transformed data
WSPA	Western Snake River Plain Aquifer or Western Snake River Aquifer
WSRP	Western Snake River Plain
X	Horizontal component
Y	Horizontal component
z	Depth of temperature sensor
Z	Vertical component

Chapter 1
Introduction

This thesis comprises the analysis of vertical seismic profiling data and geophysical well logs acquired during the International Continental Scientific Drilling Program (ICDP) in the Snake River Plain in Idaho, USA. The main focus for this thesis lies in the subsurface characterization of a selected drill site – the Kimberly borehole – using a combination of geophysical methods and downhole logs, to assess the prospects of geothermal exploration for this well. As the drill site comprises a complex geological setting, expressed by large velocity and density contrasts, surface seismic imaging techniques are limited. For that reason, vertical seismic profiling overcomes those difficulties and helps by identifying geothermal resources in the uppermost 2 km in the selected drill location (Pujol, Fuller, & Smithson, 1989).
Kimberly provides a continuous record of high temperature rhyolite volcanism that characterizes the central and eastern Snake River Plain. Seismic imaging techniques shall help to identify major flow boundaries of the volcanic province.
This chapter aims to provide background information on objectives of the project, the study area of this thesis, the geothermal system across and beneath the Snake River Plain as well as the intent of geothermal energy development in this region.

1.1 Objectives of the project

The Snake River Geothermal Drilling Project - HOTSPOT - was initiated by the International Continental Scientific Drilling Program (ICDP) and further contributors such as the U.S. Department of Energy (DOE) and the U.S. Geological Survey (USGS) to obtain a better understanding of the long-term geological and thermal history associated with the transit of the Yellowstone Hotspot (Shervais et al., 2013).

This project is one out of many scientific drilling projects with international collaboration to acquire a better understanding of processes deep within the Earth and gaining information by drilling. The aim of the ICDP is, not only to provide an understanding of geoprocesses like earthquakes, volcanoes, the paleoclimate, and geodynamic processes but also to raise the awareness of potential future resources and societal challenges coming with it.

The three selected drill sites – Kimama, Kimberly, and Mountain Home – were chosen since they provide a broad representation of prominent geological features in the Snake River Plain. The project, HOTSPOT, lies within such a unique geological setting named the Snake River Plain (SRP) in the southern part of Idaho, USA. This region comprises not only complete volcanic sequences dating back 17 Ma (Hanan, Shervais, & Vetter, 2008) but also some of the highest geothermal heat flows and gradients as illustrated in Figure 1.1 in North America. Due to the geothermal anomaly outlining the major topographic Snake River Plain, it became a focal point of interest for the ICDP. The analysis of volcanic and tectonic features in the Snake River Volcanic Province (SRVP) shall help to explain the evolution of continental mantle and crust in the Idaho area. The specific nature of this region, characterized by rhyolite and basalt flows, calderas complexes, fracture zones and sedimentary layers, is the expression for an active mantle plume sitting deep in the intra-continental North American plate. The unique continental heat distribution offers high geothermal potential in this area which can be exploited for future generations.

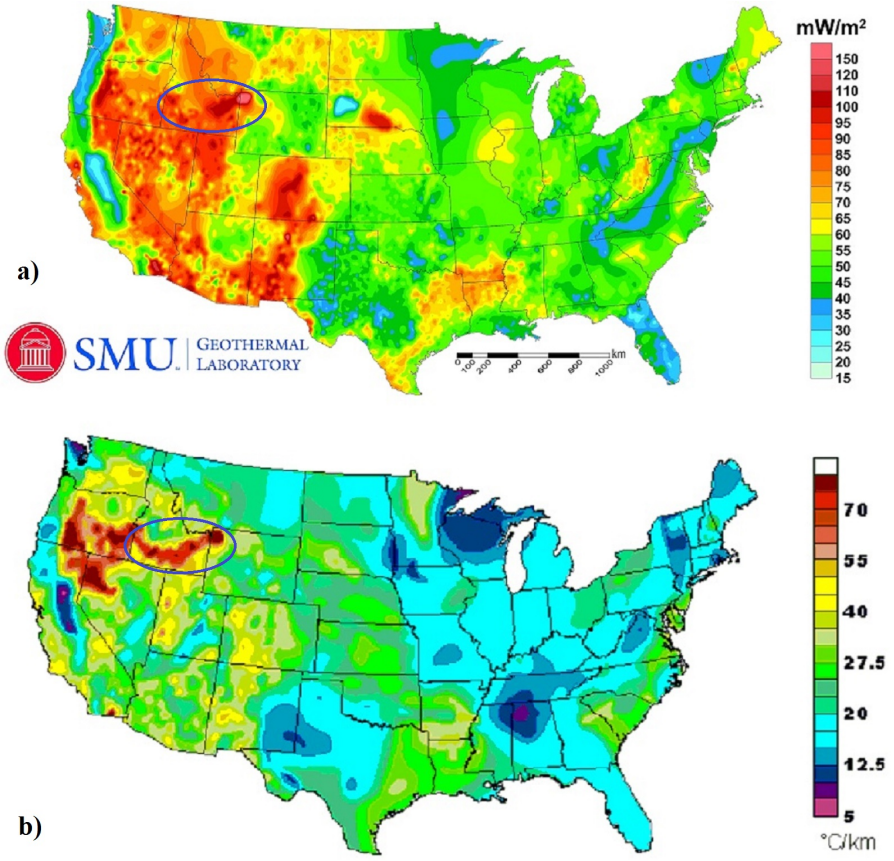

Fig. 1.1: a) Geothermal heat flow map of the United States (SMU Geothermal Lab, 2011) and the from a) derived b) Geothermal gradient map (SMU Geothermal Lab, 2011). The Snake River Plain is circled in both maps.

In Shervais et al. (2011) the major goals for the evaluation of geothermal potential in the central and western Snake River Plain were:

(1) To measure the high sub-aquifer geothermal gradient associated with the intrusion and crystallization of mafic magmas;

(2) The valley-margin settings where surface heat flow may be driven by the up-flow of hot fluids along buried caldera ring-fault complexes;

(3) A sedimentary basin adjacent to range-front faults in a large complex graben. (p. 1)

To study this region better, geological and geophysical techniques such as gravity and magnetics, surface seismic, vertical seismic profiling (VSP), borehole logging techniques, geochemical techniques and heat flow measurements are needed. Such means are necessary to determine the geothermal sources at depth while leaving only a minimal impact on the surface. In addition, borehole cores from every drill site were taken to map the continuous stratigraphy in every region. However this research project shall not only evaluate the geothermal potential, it shall also reveal possible limitations in the course of geothermal exploration and development.

1.2 Study Area

The area of interest, the Snake River Plain, stretches through the entire southern part of Idaho in a broad arc. Within the project HOTSPOT three selected deep holes were assigned to examine the geothermal potential of the Snake River Plain. The relief map in Figure 1.2 provides an overview of the spatial position of the boreholes.

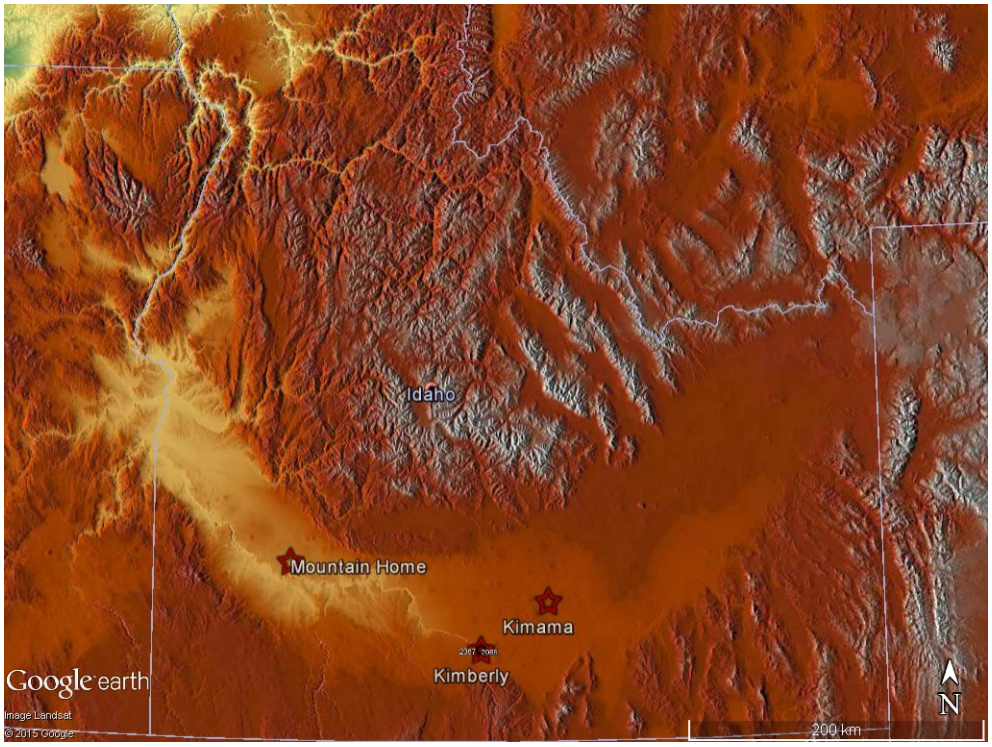

Fig. 1.2: Shaded relief-topographic map of the Snake River Plain within the US state Idaho derived from Google Earth. Red stars mark the drill sites of the ICDP HOTSPOT project.

The project commenced in 2010 with drilling first at Kimama (42° 50' 21.56", 113° 47' 47.66"), which is located on the axis of the central SRP. Kimama exhibits thick basalt flows, which originated from a series of vents. The special feature of this drill site is a basalt ridge that underlies the high topography to the east of the axial volcanic zone.
The stratigraphy of the Western Snake River Plain (WSRP) is best documented at the Mountain Home drill site (43° 4' 11.57", 115° 53'34.61") located near the Mountain Home Air Force Base, Idaho. Thus, Mountain Home provides record of old basalt units superimposed by lacustrine sediments. The evaluation of this well shall bring more insight in the geothermal potential of the WSRP to extent the previous geothermal exploration results.
In the framework of this thesis only the Kimberly borehole (42° 32' 59.39", 114° 20' 33.26"), located on the southern margin of the Snake River Plain is studied in detail. The study area including the deep borehole is located along the southwest margin of the Twin Falls volcanic complex and is approximately 10 km east of Twin Falls, Idaho. The borehole was completed in 2011 to a depth of 1956 m with reference to the Kelly bushing[1](KB) at an elevation of 1210 m above sea level (masl). The survey area is located northeast of the town of Kimberly along

[1]Kelly bushing = „The journal box insert in the rotary table of a drilling rig through which the kelly passes. Its upper surface is commonly the reference datum for well logs and other measurements in a well bore." (Sheriff, 2002, p.199)

a road, accessible via the State Highway 50. Two separate 2D surface seismic lines have been acquired closest to the well along farm fields, which are related to an agriculture research center. The walk-away VSP survey was determined in June 2011 along the northern part of the surface seismic line 2, but will be discussed and illustrated in more detail in Chapter 5. Its location offers a complete record of high-temperature rhyolites beneath a basalt and sediment cover. Figure 1.3 shows details of the topographic elevation map of the study area that emphasizes the increasing altitude to the southeast (Hanse Butte - outside the map) and the low terrain of the Snake River canyon to the north.

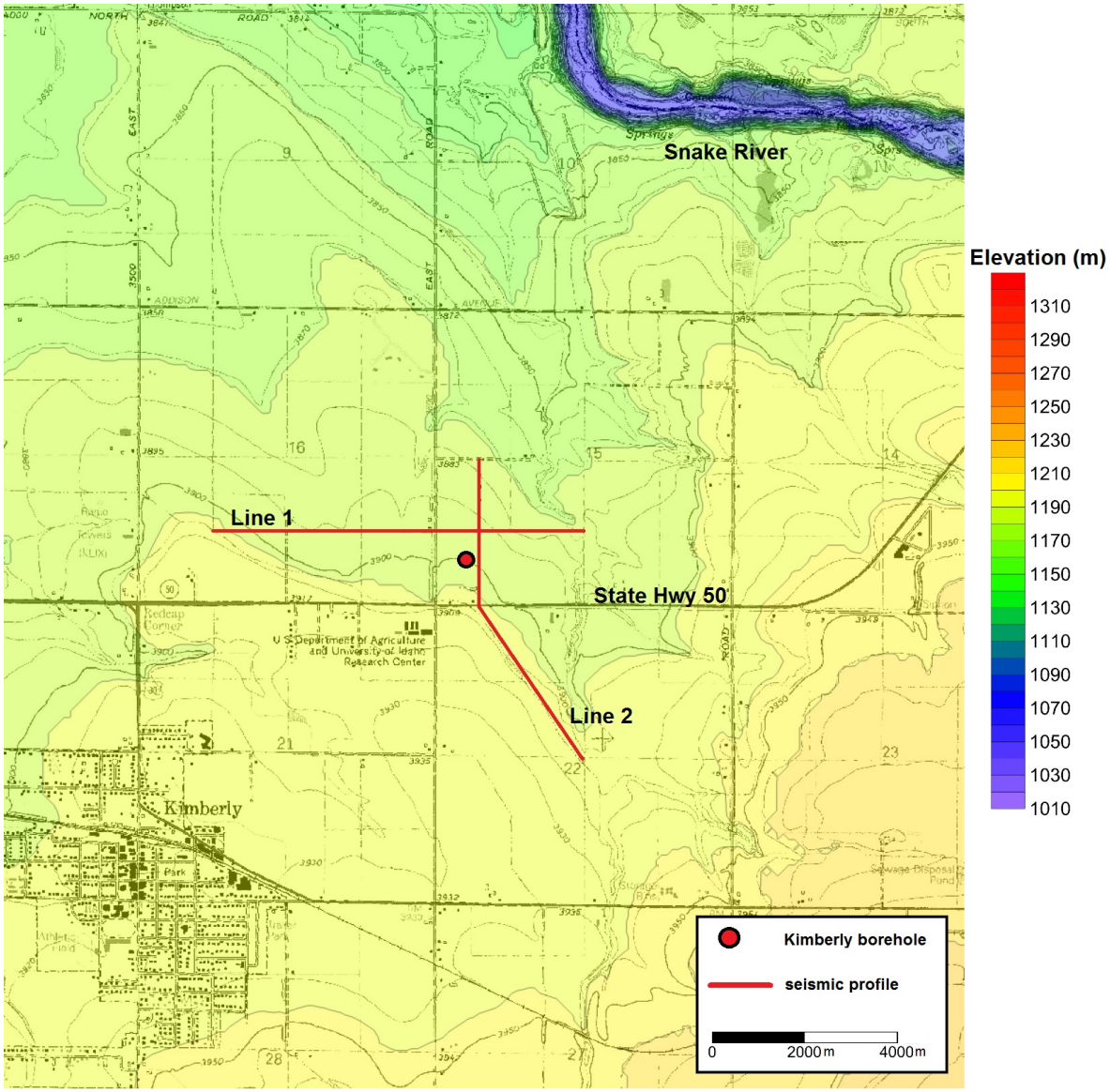

Fig. 1.3: Topographic map of the Kimberly site with corresponding elevation data from Idaho State University (n.d.). Seismic data acquisition took place along two separate lines perpendicular to each other.

1.3 Geothermal Potential of the Snake River Volcanic Province

Idaho's geothermal potential is high, not only because of the hydrothermal system of the Yellowstone caldera and their volcanic genesis, but also because of small scale hydrothermal systems, especially along the margins of the plain. These already provide geothermal power in form of direct use projects for space heating and greenhouses (Nielson, & Shervais, 2014; Fleischmann, 2006).

Temperature gradient and heat flow studies of the eastern Snake River Plain (ESRP) in shallow boreholes by Brott, Blackwell, & Ziagros (1981) show high heat flow values (> 80-100 mW/m^2) along the margins of the plain but low values (20-30 mW/m^2) dominate along the central axis. The opposite effect is exhibited in deep holes (> 1 km), where the axial site is characterized by high heat flow at greater depth. Based on those values, Blackwell (1989) suggested that the apparent hotspot movement is reflected by an eastward increase of heat flow from about 75-90 mW/m^2 to 90-110 mW/m^2 in the Snake River Plain. Brott et al. (1981) discussed that the ESRP heat flow pattern may be related to „the combined effects of high mantle heat flow, crustal thermal refraction and cooling of a large crustal intrusion." (p.2). For the ESRP a mean heat flow of 190 mW/m^2 was calculated but the determination of regional heat flows is moderated through cold groundwater circulations in the Snake River Aquifer (SRPA). The low values of heat flow in the central part of the ESRP are caused by surficial water circulating through the Snake River Aquifer, which is a massive groundwater aquifer system responsible for cold groundwater circulation beneath the plain. Generally the study of Brott et al. (1981) showed that below the aquifer the system stabilises and results in constant, positive gradients. The heat flow correlations of the eastern Snake River Plain are shown in Figure 1.4.

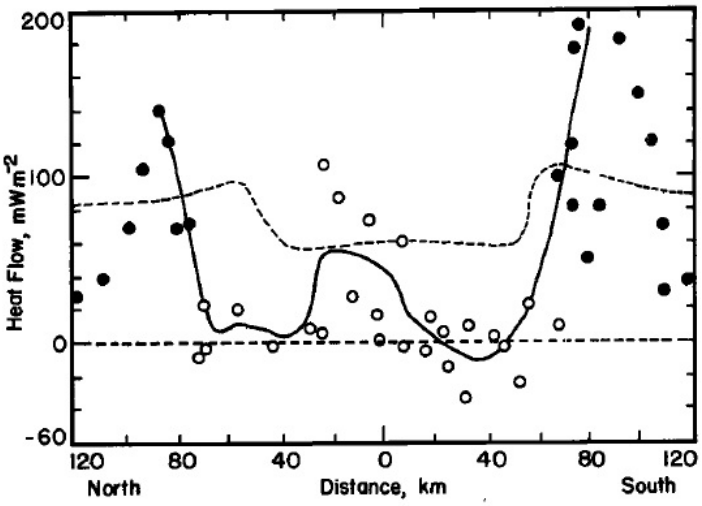

Fig. 1.4: Cross section of heat flow values for a profile extending 50 km east from a line between Arco and Pocatello in the eastern part of the Snake River Plain. The heat flow values are distributed in perpendicular distance from the axis of the Snake River Plain. Solid curve represents the smoothed eastern Snake River Plain heat flow profile calculated from open and solid circle values. The dashed curve is the theoretical heat flow profile of the western Snake River Plain modelled by Brott, Blackwell, & Mitchell (1976). Heat flow values from inside and outside of the Snake River Aquifer are presented as open and solid circles (Brott et al., 1981).

Although the WSRP shows a similar heat distribution (Figure 1.4 - dashed curve), low heat flow values are induced due to large-scale heat refraction of the underlying sedimentary basin,

which result from crustal thermal conductivity contrasts (Blackwell, 1989). The sufficiency of geothermal resources is defined by its intended use, namely as heat or electricity. Thus, for direct applications temperatures of 29°C are already sufficient. However, to generate power for the electric grid and for distribution, temperatures in excess of 100°C are necessary. Although only a small percentage of Idaho's heating is provided by geothermal resources, an increase in direct use projects as an viable heating alternative is possible. Electric production gained ground through the Raft River geothermal project, which started in January 2008 with a 13 MW net capacity. This project is the first geothermal binary operation for commercial use in Idaho. Additional areas with geothermal resource potential for electric power generation are located in the Basin and Range province due to high crustal heat flow. Until 2006, 745 geothermal wells and 308 hot springs were classified as target prospects for geothermal resource potential, whereby hot springs and shallow wells commonly provide temperatures of 65 to 93°C in the Snake River Plain. Thereby, resource assessments are only performed when temperatures are greater than 150°C and exploration depth is less than 3000 m but new technical developments in the past years softens this specification (Fleischmann, 2006).

Having a closer look at the geothermal resources of the Twin Falls-Banbury system, including the selected drill site Kimberly, temperatures between 30° to 70° C are characteristic in depths of < 900 m. In the 1930's the City of Twin Falls first encountered geothermal resources in a well and until now drilling reveals a low to moderate geothermal resource base. The basement rock is comprised of tertiary rhyolite of the Idavada Volcanic Group whose high permeability origins in the circulation of thermal water in tectonic and cooling fractures and the porosity of the non-welded ash-flow tuffs[2]. As numerous warm water wells occur in the vicinity of the borehole, Kimberly has a geothermal production potential (Street & Detar, 1987).

[2]Tuff = „A general term for all consolidated pyroclastic rocks." (Bates & Jackson, 1984, p.539)

Chapter 2
Geology

The Snake River Plain is a topographic depression extending 600 km in an east-west arc across southern Idaho (Bonnichsen, White, & McCurry, 2002). The Neogene plain is surrounded by high elevation terrain as the Owyhee Plateau in the south-west, the Columbia Plateau in north-west, the Idaho Batholith in the north, the Basin and Range province in the south- and north-east as well as the Rocky Mountain System in the east (Fig. 2.1). The development of the Snake River Plain is in every aspect – geological and structural evolution, crustal structure, age progression of volcanism, and other anomalous geophysical characteristics – unique (Leeman, 1982). The complex geology is the expression of the tectonic and magmatic evolution of the Snake River Plain volcanic province that evolved through several processes like extension and rifting as a consequence of crustal thinning and the migration of the North American Plate over a stationary, deep seated melting anomaly (mantle plume) (Bonnichsen et al., 2002; Leeman, 1982). As the lithospheric plate moved southwestwards over the deep thermal mantle plume, rhyolitic eruptive centers marked the track of the apparent hotspot movement (Shervais, 2001).

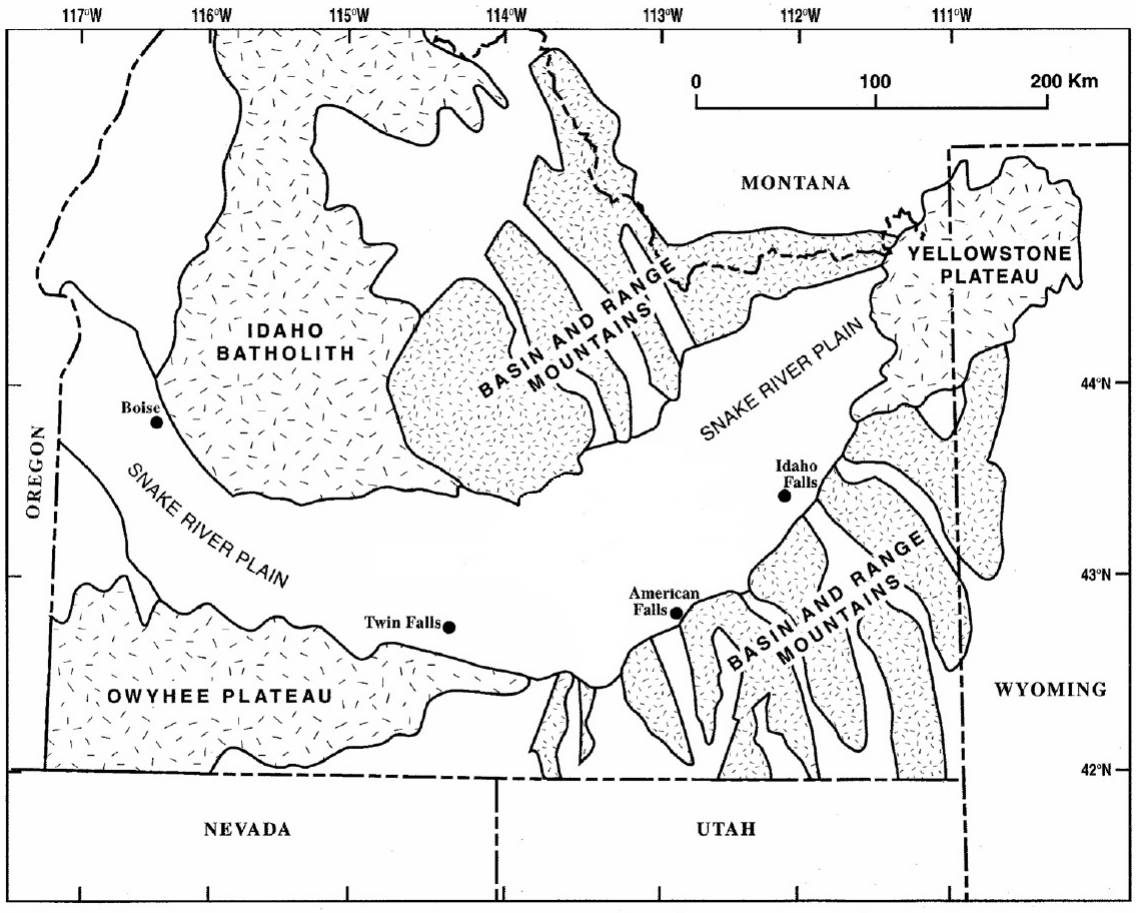

Fig. 2.1: Schematic map of southern Idaho with the Snake River Plain and adjoining mountain ranges. Figure adapted from Wikipedia (2010)

The hotspot volcanism started 16 Ma ago along the present Nevada-Oregon boundary and is associated with the Columbia River - Oregon Plateau flood basalts, which erupted ca. 14-17 Ma ago beneath the northern Basin and Range Province. This knowledge is consistent with a thinning in lithosphere beneath Oregon and Washington during that time. Due to the alternating migration rate and orientation of the North American plate during this SRP-Yellowstone style volcanism it is difficult to clearly identify the location where the hotspot initiated. At the beginning of the volcanism, 10 Ma and older, the North American plate migrated with an apparent rate of 7.0 cm/a in N.75°E direction. But for the last 10 Ma, the plate slowed down to an apparent rate of 2.9 cm/a and shifted to the new orientation of N.54°E. A further characteristic of the hotspot-related process is the topographic uplift of up to 1 km caused by the rising of the plume head. Thereby, the uplift expanded over areas with a north-south dimension of 1000 km and was accompanied with a subsequent subsidence as the hotspot passed. These results were derived from paleo-botanical estimates of the altitudes during the Cenozoic (Pierce, Morgan, & Saltus, 2002).

The Snake River Plain comprises two main parts: The north-east trending Eastern Snake River Plain as a topographic downwarp and the structural basin of the north-west trending Western Snake River Plain. As a transition zone the Central Snake River Plain, which also includes the Twin Falls volcanic center, is classified (Fig. 2.2). Although both terrains are topographically very similar, they differentiate in terms of volcanic history, stratigraphy and their crustal structure. The hotspot track in the eastern Snake River Plain is the direct link to the rhyolite volcanism followed by a thin carapace of basalt, but it is not linked in any way to the western Snake River Plain whose stratigraphy is comprised of fluvial and lacustrine sediments with interbedded basalts. The crustal thickness of the Snake River Plain is greater than the crust of the adjacent Basin and Range province. Whereas the upper crust beneath the plain is thinner than normal, reaching a thickness of 10 km for the ESRP and 6 km for the WSRP, the lower crust thickened to approximately 30 km for the ESRP and 38 km for the WSRP (Shervais, 2001). The crust of the western United States passes through a transition from oceanic crust in the west over inter-median crust to Precambrian continental crust in the east (Pierce et al., 2002).

2.1 Eastern Snake River Plain

The geologic and tectonic history of the ESRP is characterized by complex processes of magmatism and deformation, entailing extension and subsidence of the plain. The overall picture of the ESRP is shaped by Miocene-Quaternary volcanic and sedimentary rocks, but almost the entire Neogene to early Quaternary structures of rhyolites and sedimentary fills are concealed by younger basalt flows. Thus the ESRP is a bimodal (rhyolitic/basaltic) magmatic province. However, Quaternary volcanism did not take place in a uniform time transgression so that the model of a deep-seated mantle plume and other mantle processes play an important role in evaluating the geologic and tectonic history of the SRP (Rodgers et al., 2002).

The hotspot track is reflected in distinct rhyolitic volcanic provinces along the axis of the ESRP. Volcanic centers (Fig. 2.2) in the southwest – Owyhee-Humboldt, Bruneau-Jarbidge, and Twin Falls – manifest high-temperature rhyolites, whose low crustal magma generation arise from a younger, thinner and deeper crust as the northeastern magmas with varied trace element signature. Furthermore, the hotspot resided longer below the crust of the north-eastern volcanic centers Picabo, Heise and Yellowstone as a result of the eastward-thickening

craton. The transition between the SW-segment Twin Falls and the NE-segment of the Picabo volcanic center is reflected in its differing chemical and mineralogical composition (Hughes et al., 2002). Each volcanic center represents one or more major calderas, which resulted from ‚super volcano' class rhyolite eruptions with a size of over $\geq 1000\ km^3$ (Leeman, Annen, & Dufek, 2008). In addition, large ash flows, lava flows and smaller ignimbrites characterize the area.

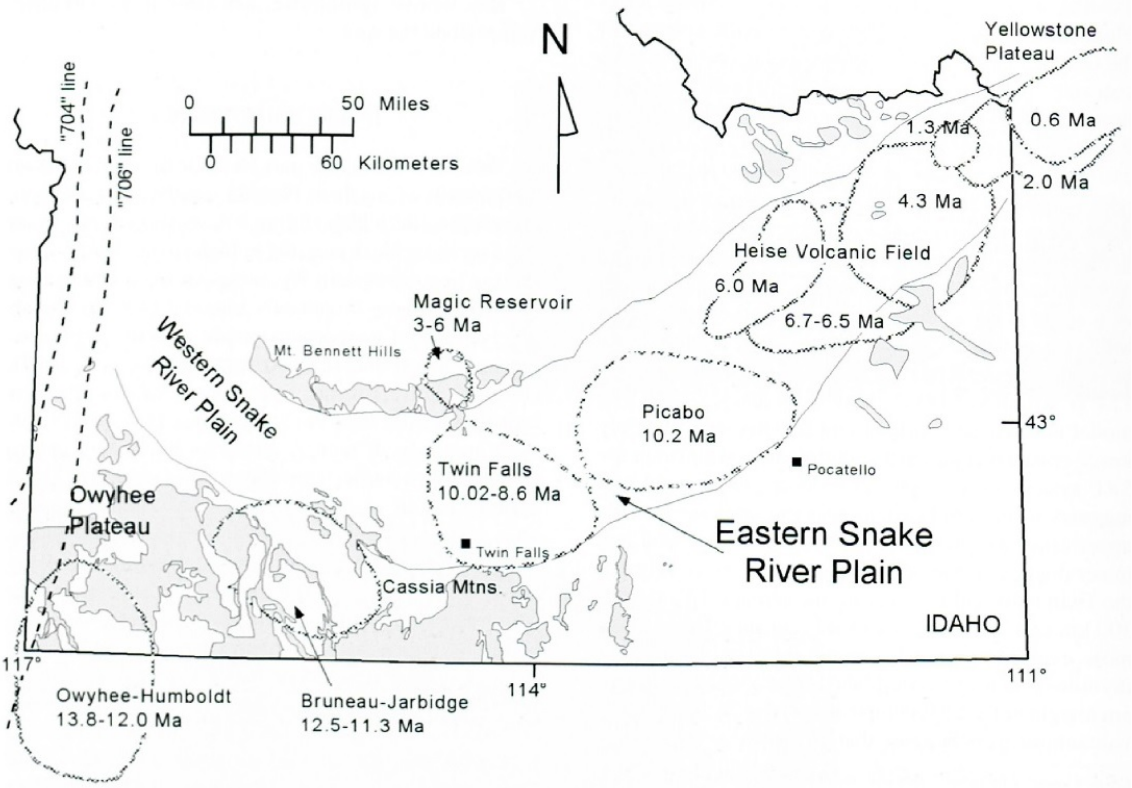

Fig. 2.2: Volcanic centers associated with the ESRP hotspot track (Hughes et al., 2002)

The rhyolites of the southwestern SRP centers, like Owyhee-Humboldt, Bruneau-Jarbidge, and Twin Falls, that formed at very high temperatures are typified with anhydrous phenocryst[1] assemblages as well as with rheomorphic [2] folding (Table 2.1). Such rheomorphic features emerge if gravitational forces cause the high-temperature rhyolite to flow and partially to coalesced. Due to a differing chemical and mineralogical composition of the northeastern volcanic centers Picabo, Heise, and Yellowstone, ignimbrites show rarely rheomorphism but weld to a densely extent. The reason for this is on the one hand the hydrous phases (biotite and amphibole) and on the other hand vapor-phase zones (Hughes et al., 2002). Table 2.1 and Figure 2.2 depict an overview of the locations of the volcanic centers and their ENE younger becoming rhyolitic units as well as a summary of the geochemical composition and mechanism.

[1] Phenocryst=„One of the relatively large and ordinarily conspicuous crystals of the earliest generation in a porphyritic igneous rock" (Bates & Jackson, 1984, p.381)

[2] Rheomorphism=„The process by which a rock becomes mobile as a result of at least partial fusion, commonly accompanied by, [...], addition of new material by diffusion." (Bates & Jackson, 1984, p.431)

Tab. 2.1: Summary of locations, ages, and eruptive mechanisms of six SRP volcanic centers. Adapted from Hughes et al. (2002)

Volcanic Center	Owyhee-Humboldt	Bruneau-Jarbidge	Twin Falls	Picabo	Heise	Yellowstone
Location	42°N 116°-117°W	42°30'N 115°-116°W	43°N 114°W	43°N 113°W	44°N 112°W	44°30'N 111°W
Age (Ma)	13.8-12.0	12.5-11.3	10.0-8.6	10.2	6.7-4.3	2.0-0.6
Minerals, common (& rare or accessory)*	Pl,Qtz,Sa, Pgt,Mag, (Opx,Zrn, Ap)	Pl,Qtz,Sa, Cpx,Pgt,Mag, (Fa,Opx,Ilm, Ap,Mnz,Zrn)	Pl,Pgt,Cpx, Qtz,Mag, (Opx,Sa, Ap,Zrn)	Pl,Qtz,Sa, Bt,Cpx, (Ap,Zrn)	Pl,Qtz,Sa, Cpx,Opx, Mag,Bt, (Zrn,Ap)	Qtz,Sa,Pl, Cpx,Cam,Fa, Mag,Ilm,(Zrn, Aln,Ap)
Anhydrous assemblage?	yes	yes	yes	no	no	no
Rheomorphism?	yes	yes	yes	no	no	no
Magmatic Temperature	> 1090°C	850°C - 1000°C	1040°C - 1100°C	not determined	est. $\sim$ 860°C	820°C - 900°C

*Mineral abbreviation (Kretz,1983): Qtz=quartz, Pl=plagioclase, Sa=sanidine, Pgt=pigeonite, Cpx=clinopyroxene, Opx=orthopyroxene, Mag=magnetite, Cam=clinoamphibole, Fa=fayalite, Ilm=ilmenite, Bt=biotite, Ap=apatite, Zrn=zircon, Mnz=monazite, Aln=allanite.

Hughes et al. (2002) illustrated in Figure 2.3 a simplified model of the magma genesis and evolution of the ESRP and factored in the geochemical and petrologic data for both segments separated along the 114°W longitude. In the southwestern part extension processes in the Basin and Range provinces helped silic magma, generated at temperatures in excess of 1000°C, to ascend through fissures and to erupt in the lower and middle crust. For the SW-type eruptions only minor subsidence in the form of crustal downsag due to the deep-crustal source eruptions occurred. As the crust thickens to the east and is not greatly affected by lithospheric extensions, magmas ascend in the upper crust and coalesce there. The northeastern mafic magmatism led to extensive ash eruptions accompanying caldera collapses.

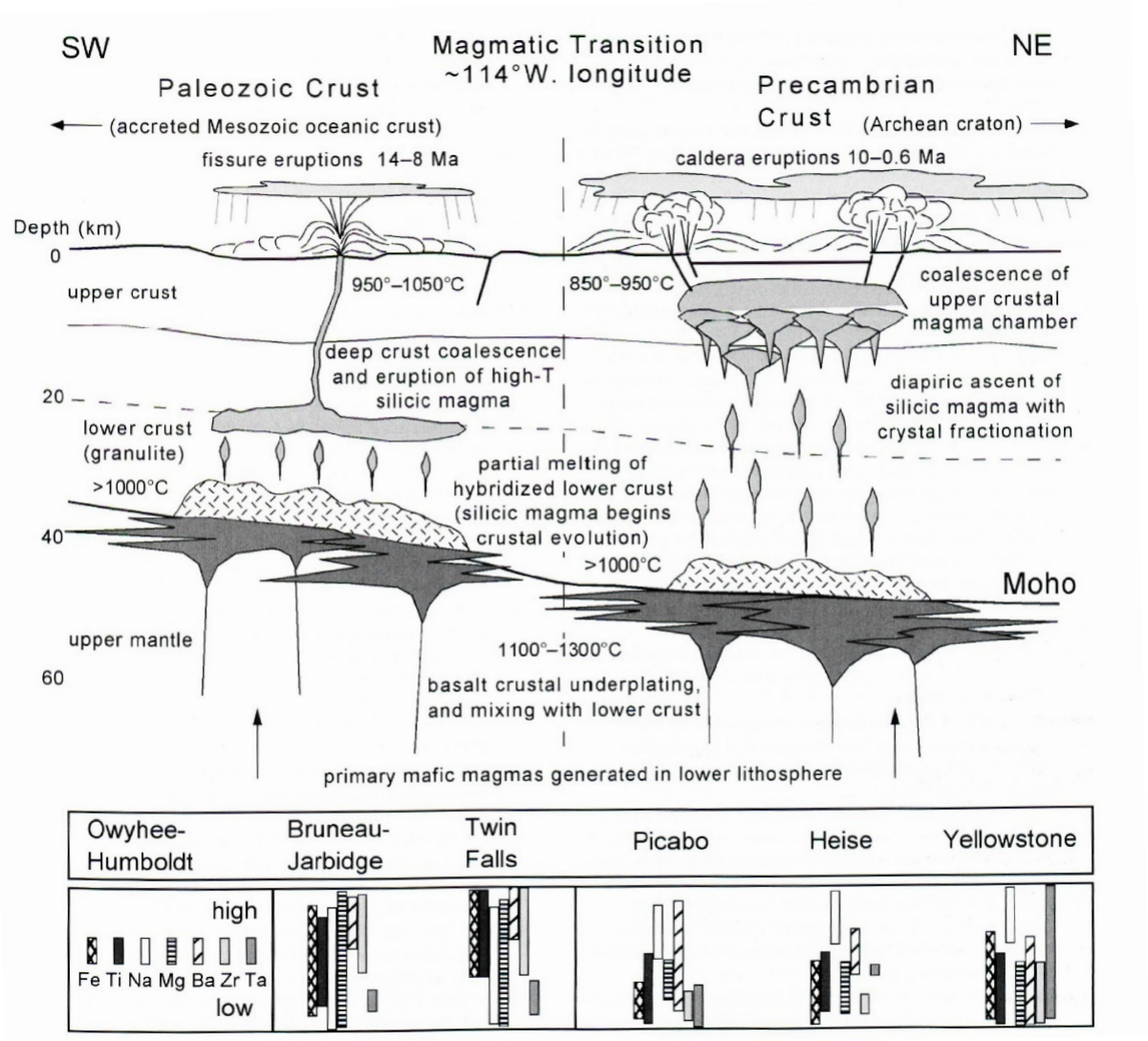

Fig. 2.3: Schematic model of the magmatic processes beneath the Eastern Snake River Plain with respect to the magmatic transition zones at longitude 114°W (Hughes et al., 2002).

Hanan et al. (2008) assume a 10 km thick layered mafic sill complex, which was built by intrusions of basaltic magma in the middle crust. The mid-crustal layer shows a seismic velocity of ca. 6.5 km/s and is situated between the felsic upper crust and the granulitic lower crust (Shervais, Vetter, & Hanan, 2006). This is supported by seismic measurements which reveal a low velocity zone of up to 200 km below the plain, which may correspond to a partially melted mantle (Hughes et al., 2002).

The subsidence mechanism is an expression of the hotspot causing thermal contraction, which is also evident by crustal densification of mafic magmas. The surface subsidence appears as a decline in elevation towards the west of the axis of the plain.

Faulting in the ESRP plays a minor role in comparison to faulting processes, especially parallel strike-slip faults, in the WSRP. The only prominent normal faults originated in middle and late Miocene are present along the margins of the eastern plain (Leeman, 1982).

After the enormous rhyolite eruptions and the drainage of the Lake Idaho, basaltic volcanism dominated the surficial rock layers of the Snake River Plain. The basaltic eruptions were

deposited in varying degree, which include for example 1.2-0.8 Ma old ferrobasalts (Bonnichsen & Godchaux, 2002). Figure 2.4 illustrates schematically the Quaternary-Holocene successions of magmatic and surficial processes of the ESRP. The majority of the volcanic landforms are associated with the basaltic plain-style volcanism, including coalesced shields with eruptive and non-eruptive fissures, more evolved eruptive centers with cinder cones and tuff rings. Furthermore, rhyolite domes and sedimentary interbeds shape the character of the landscape (Hughes & McCurry, 2002).

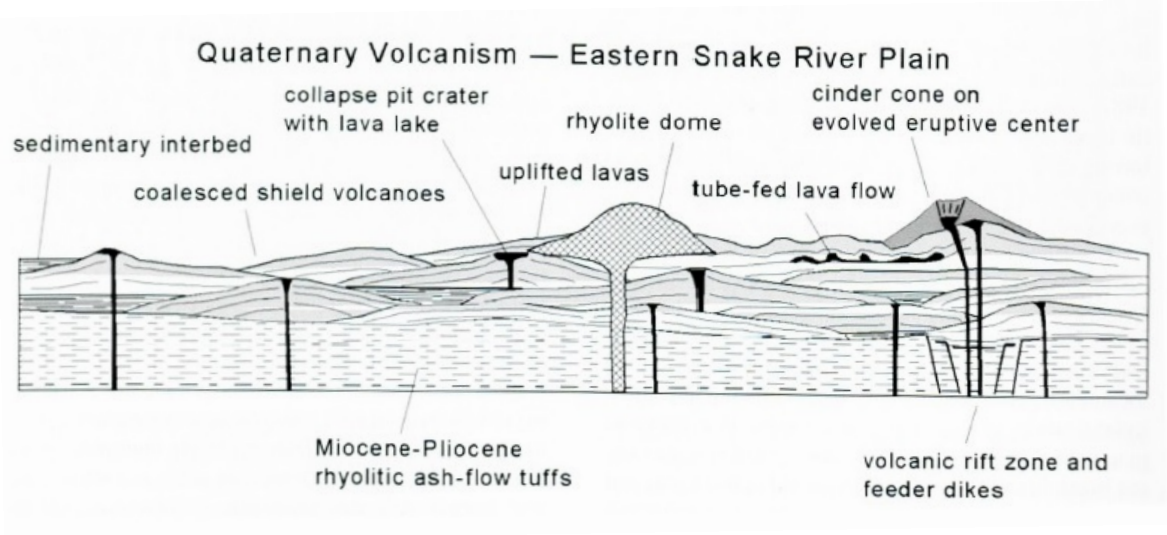

Fig. 2.4: Schematic diagram of basaltic plains-style volcanism on the eastern Snake River Plain (Hughes & McCurry, 2002)

2.2 Western Snake River Plain

In contrast to the hotspot volcanism dominated ESRP, the tectonic history of the WSRP is associated with extension processes of the Basin and Range province, forming an intracontinental rift basin. The WNW-ESE trending graben structure is a right-lateral extensional strike slip system, whose origin is found in the formation of the Oregon-Idaho graben about 15.3 ± 0.5 Ma ago and with the Adrian fault zone forming the southern margin of the WSRP. Moreover, various regional faults show parallel orientation to the western plain rift. This originates from the weakening lithosphere as the hotspot passed, causing a failure along those zones. However, the normal fault-bounded basin developed especially during the last 9.5 Ma, tilting towards the center of the basin. Not only the rift structure but also the involved subsidence supported the development of a Pliocene lacustrine system – Lake Idaho – between 9.5 to 1.7 Ma (Shervais et al., 2002; Wood & Clemens, 2002).

The volcanic activity in the WSRP, which took place in three stages, shows no clear link to the passage of the hotspot and associated volcanism. Rifting processes originated in rhyolite volcanism around 10-12 Ma ago and were followed by a sequence of basaltic volcanism 7-9 Ma ago (Shervais & Vetters, 2009). But the major part of the WSRP geology is comprised of Neogene 2-3 km thick sedimentary deposits in the basin. Thereby, parts of the earliest sediments originated from faulting processes and basaltic volcanism. Those deposits like mudstone, interbedded arkose or volcanic ash are attributed to the Chalk Hills Formation. As subsidence was in process, the basin was covered with a further sedimentary sequence, called the Glenns Ferry Formation, which is also the main formation providing the bedrock for the

WSRP aquifer. As the Lake Idaho drained, the third stage volcanic activity, the Pleistocene basaltic volcanism proceeded along a line of vents at ca. N. 70°W and overlayed the deltaic and lacustrine sediments. This last stage of alkali basalts occurred simultaneously with the basaltic volcanism of the ESRP (Shervais et al., 2002b).

2.3 Central Snake River Plain with Twin Falls Region

The central SRP comprises the area where the Owyhee Plateau, the western SRP rift system and the southwestern part of the eastern SRP converge. The Twin Falls regions is characterized by its basaltic cover over the northern and central parts of the plain and its pre-basaltic rocks shaping the highlands outside the southern margin (Bonnichsen & Godchaux, 2002).

As illustrated in the stratigraphic column in Figure 2.5, late Miocene densely welded ignimbrites dominated successions of the Cassia Mountains and the northeastern corner of the Bruneau-Jarbidge region in the southern part of the Twin Falls Region. The extension of those high-temperature ignimbrite sheets comprised several tens of kilometers. But in the eastern part of the Twin Falls region, some of the ignimbrites were overlapped by sequences of 10.2 Ma and younger layers, which erupted from vents of the Twin Falls volcanic field itself. In comparison to younger eruptions, e.g. at Yellowstone, ignimbrite eruptions of the Bruneau-Jarbidge repeated more frequently, but are also characterized with lulls of 200-400 ka. Geochemical analysis of central SRP rhyolites reveal SiO_2 contents of 71-76% (Bonnichsen & Godchaux, 2002; Leeman et al., 2008).

At the bottom of the Snake River Canyon in the Twin Falls area a succession of the so called Shoshone Falls rhyolite outcrops below various basalt flows. The Pleistocene basalt cover reaches in parts thicknesses of up to 1 km. Branney et al. (2008) assigned the Central Snake River Plain a special type of volcanism, which has a diverse characteristic as the typical silicic volcanism. Hence, Miocene rocks of the central SRP are allocated to the SR-type volcanism. This new defined type of volcanism is characterized by low velocities and high temperatures of around 900-1050°C (see magmatic temperature in Table 2.1). In particular, the silicic SR-type volcanism is dominated by large-volume silicic eruptions with low aspect ratio[3] rhyolite lavas whose assemblage differentiates from the common pumice-rich ignimbrites and Plinian eruptions. Generally SR-type volcanism is pumice lapilli poor, mostly represented by intensely-welded ignimbrites showing a high degree of rheomorphism. Solely > 40 rhyolite ignimbrite sheets have been detected by Branney et al. (2008) with thicknesses of up to 200 m in the central SRP. Most of those ignimbrite have low aspect ratios and therefore spread laterally up to tens of kilometers. In lithoidal and vitrophyre zones, flow banding and lamination occur.

[3] Aspect ratio: „Ratio of average thickness of flow to diameter of circle covering the same area as the flow.“ (Johnson, 1989, p.56)

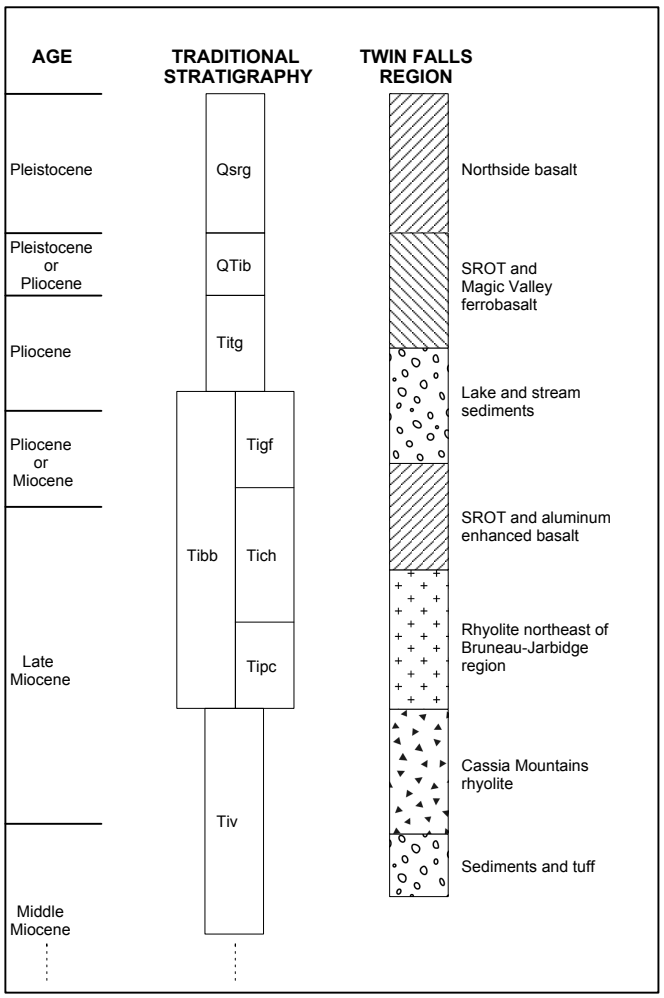

Fig. 2.5: Stratigraphic column of the Twin Falls region together with the traditional stratigraphy of southwestern Idaho. The traditional stratigraphic units are identified as follows: Qsrg - Snake River Group, QTib - Bruneau Formation of the Idaho Group, Titg - Tuanna Gravel and Tenmile Gravel of the Idaho Group, Tigf – Glenns Ferry Formation of the Idaho Group, Tich – Chalk Hills Formation of the Idaho Group, Tipc – Poison Creek Formation of the Idaho Group, Tibb – Banbury Basalt of the Idaho Group, Tiv – Idavada Volcanics, SROT – Snake River olivine tholeiite. Adapted from Bonnichsen and Godchaux (2002).

In the northwest of the drill site is the Perrine Bridge, providing a complete overview of the volcanic stratigraphy of the CSRP. The gorge, which was formed by the Snake River, outcrops 6.25 Ma Twin Falls rhyolite in a depth of over 120 m. The subsequent layers consist of a thick section Hub Butte Basalt and a thinner Flat Top Butte Basalt section. Between the volcanic sequences thin wedges of lacustrine and deltaic sediments (Pliocene Glenns Ferry Formation) indicate that the Twin Falls area was influenced from the distant Lake Idaho (Shervais et al., 2005).

2.4 Mantle Plume Paradigm

Mantle plumes are known as the main forces in plate movements and heat release. Their constituent parts, plume head and plume tail, are involved in the generation and modification of plate boundaries as well as in imprinting a rift structure in the lithosphere (Shervais, 2001). Studies by Bonnichsen et al. (2002) estimated for the Snake River Plain a plume head of 400 km diameter at the first stage.

Although the model of the Snake River-Yellowstone Hotspot is widely accepted there are still some controversial aspects restraining this idea. Firstly, geochemical analysis of the most common elements, trace elements and He-isotopes of basalts indicated a deep, sub-lithospheric mantle source that is similar to the source of ocean island basalts (Hanan et al., 2008). Whereas, the Snake River Plain basalts are more iron rich than normal basalts of oceanic origin (Shervais, 2001). However, the composition of radiogenic isotope does not precisely clarify the origin of the hotspot volcanism as the „ancient cratonic lithosphere will superimpose its inherent isotropic composition on sublithospheric plume or asthenospheric melts.“ (Hanan et al., 2008). As little is known about chemical dynamics of mantle plumes in continental crust (Shervais, 2001).

Humphreys et al. (2000) detected with the help of teleseismic events zones of anomalously high temperatures at 410 km and 660 km in the mantle. This suggests that the mantle is hot and abundant enough to produce basaltic melt, which ascents under adiabatic conditions. Moreover, those parts of basaltic melt are depleted and show high velocity anomalies in the mantle and lower velocities for only partially molten mantles. The model derived from the teleseismic images indicates a relatively viscous and buoyant residuum, which may be coupled to the North American plate. Basically, both variants – the unusual lithospheric trend as well as the tectonic history with reference to the subduction zone of the Cascade Mountains – show advocacies and contradictions (Humphreys et al., 2000).

2.5 Snake River Aquifer

Beneath the Snake River Plain extends an immense groundwater reservoir with a thickness of up to 400 m, containing as much water as Lake Erie. Similar to the two portions of the Snake River Plain, the aquifer beneath the plain is separated along Salmon Falls Creek into the Eastern Snake River Plain Aquifer (ESPA) and the Western Snake River Plain Aquifer (WSPA) due to different hydrologic and geologic conditions (Grey & Link, n.d.; Wikipedia, 2010). In the following the ESPA shall be addressed in particular as it underlies the volcanism of the eastern plain and plays a significant role in the study area of Twin Falls.

The aquifer is supported by permeable zones of basalt, through which water can seep from the top to bottom of the lava flows in columnar jointing. In particular, rubble zones with interconnected pore space and fractured zones, which were created through cooling processes, provide a conduit for the groundwater flow (Grey & Link, n.d.; Smith, 2004). Smith (2004) stated that especially along the axial ridges of the basaltic lava flows the high permeability and porosity can be traced back towards its vesicular state with high concentrations of gas bubbles. Interbedded sedimentary layers serve as impermeable zones below the water table so that the Snake River Aquifer is defined as an unconfined aquifer.

The water recharges from infiltration of streams and irrigations water as well as from snow melt in the highland north of the plain with a temperature of 8°-9°C and drains from there southwestwards to the Snake River and other streams as illustrated in Figure 2.6. The area

of discharge is located at Thousand Springs, west of Twin Falls and to a smaller amount at American Falls Reservoir (Shervais et al., 2005). Hereby, discharge zones have temperatures of 14°-15°C (Nielson, Delahunty, & Shervais, 2012).

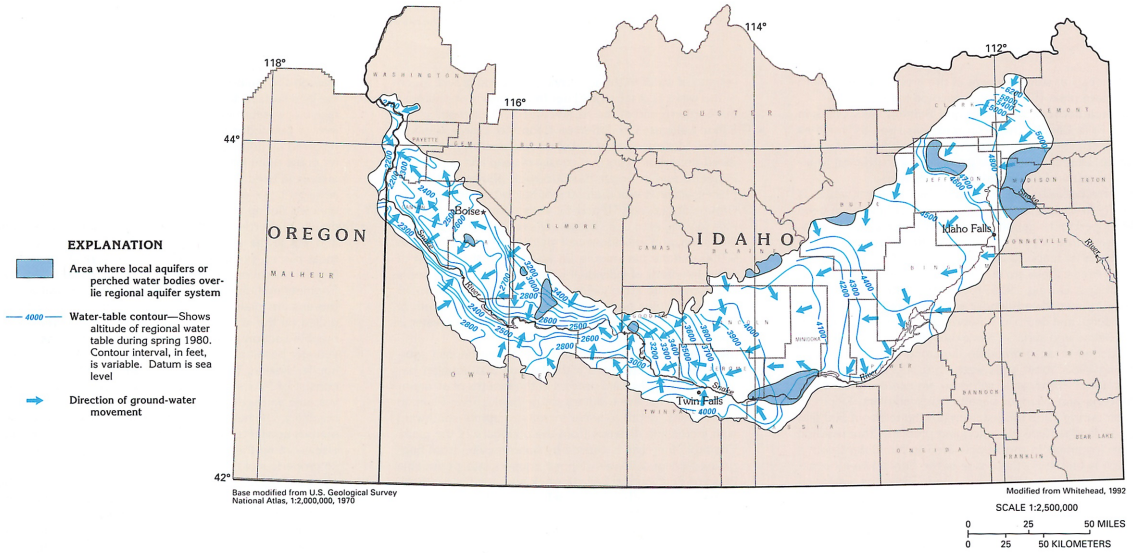

Fig. 2.6: Map showing major flow-directions and water tables of the Snake River Aquifer (USGS)

All in all, the ESPA is an essential key element of southern Idaho's drinking and irrigation water supply and is essential for its economy. The U.S. Environmental Protection Agency (U.S. EPA) assigned the ESPA in the year 1991 as a sole source aquifer to keep it under protection for contamination. Therefore, the EPA defines „a sole or principal source aquifer as one which supplies at least 50 percent of the drinking water consumed in the area overlying the aquifer. EPA guidelines also stipulate that these areas can have no alternative drinking water source(s) which could physically, legally, and economically supply all those who depend upon the aquifer for drinking water." (U.S. Environmental Protection Agency, 2015).

Chapter 3
Geophysical Well Logging

After drilling, geophysical borehole measurements are carried out to obtain detailed information about the subsurface stored in highly resolved logs. The subjects of investigation are in-situ physical properties of the rocks in the direct vicinity of the borehole, e.g. petrophysical parameters like porosity, saturation and permeability. The challenge of interpreting various geophysical logs is in the determination of those inferred physical parameters, describing the undisturbed formations, from directly measured ones like resistivity, interval transit times and natural radioactivity.

Geophysical well logging can be placed in two categories: On one hand, passive methods that measure the natural physical parameters and fields (temperature, natural radioactivity, electric self-potential), and on the other, active methods, that perturb the physical fields (electrical and acoustic) and then measure the physical response of the formation with a sensor. Active methods are used to determine for example the bulk density from gamma-gamma ray logs or the electric resistivity from electrical logs.
Downhole logging for the Snake River Scientific Drilling Project (SRSDP) at the three distinct sites Kimberly, Kimama and Mountain Home was part of an extensive study to understand the geothermal system across the Snake River Plain. In addition to the 6 km core documentation from all drill sites, preserving detailed records of sedimentary and volcanic units, the objective for wireline logging in the Snake River Plain is to identify natural fractures, which may serve as fluid flow pathways. Furthermore, geophysical logging shall help locate lithologic boundaries at depth, analyse rock properties and extend geological interpretations.

This chapter concentrates on the geophysical log analysis of the 1956 m deep Kimberly well in the Twin Falls region in Idaho. It starts with an overview of the individual wireline logging methods used in the Kimberly well, and will include an interpretation section. The main focus will be directed towards the detection of fractures, rock characterization, quantitative determination of rock properties, heat production, and acoustic properties to evaluate the geothermal potential for this well.

3.1 Borehole Logging

Openhole logging at the Kimberly well was carried out by the Operational Support Group (OSG) of the ICDP in June 2011, obtaining a broad spectrum of geophysical logs. Prior to this a commerical provider made measurements with the neutron and gamma-gamma density log through the drill string only. Borehole data was generated in form of continuous point measurements by pulling the logging tool to the surface. Logging measurements at the Kimberly well included the following sondes parameters: Caliper, temperature, magnetic susceptibility, full vector magnetic field, resistivity, total natural gamma radiation, spectral natural gamma logging, neutron logging, full waveform sonic and ultrasonic borehole televiewer imaging. The borehole consists in the upper 213 m of a cemented cased section. Whereas the open hole section below the casing was divided in a HQ drilling section (98 mm bit size) and NQ section (77 mm bit size), which are used as protective guides for the wireline logging sondes. Figure 3.1 provides a summary of the geophysical logging at the Kimberly well to a maximum logging depth of 1900 m. A complete summary of logging operations is listed in Appendix A.

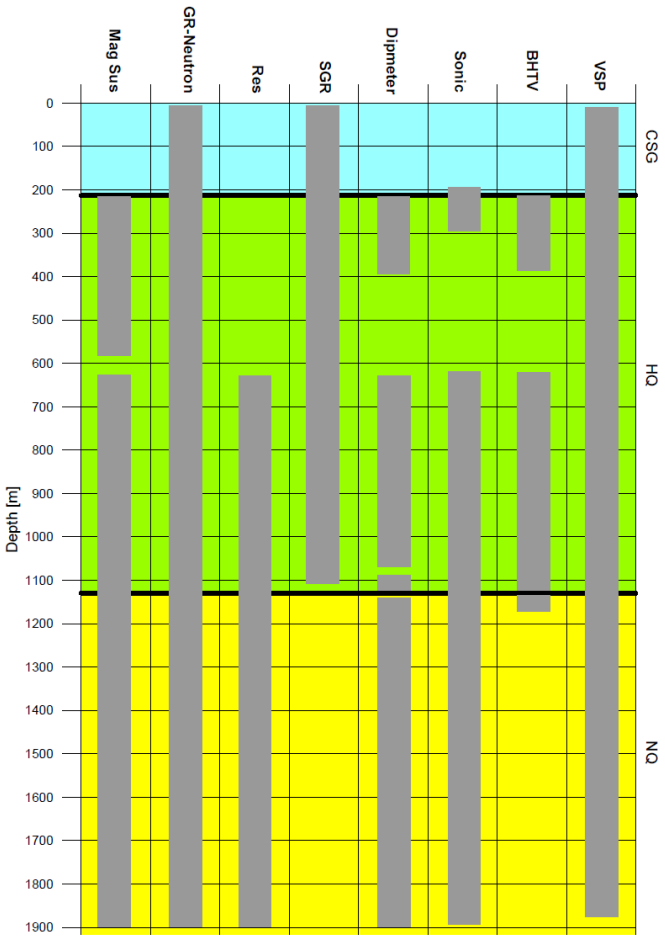

Fig. 3.1: Geophysical Logging Summary at Kimberly. Casing (CSG), coring (HQ,NQ) and geophysical borehole investigations are marked according their logging depth.

The vertical resolution of the sondes reveals the ability to differentiate layers with certain physical contrasts from one another, and to define its position in depth (Table 3.1). All measurements in this thesis are referred to the top of the pipe drive (KB) with an elevation of 1.75 m above ground elevation (1210 m). The following sub-sections provide the theory behind the different logging measurements, give insight in the measuring process and define the physical parameters measured.

Tab. 3.1: Vertical resolution for sondes used at the ICDP HOTSPOT program (Kück, n.d.).

Measuring method	**Theoretical vertical resolution (cm)**
Total natural gamma ray (GR)	20
Spectal natural gamma ray (SGR)	20
Magnetic susceptibility (MS)	20
Full waveform sonic (BS)	50
Resistivity (DLL)	80
Dipmeter (DIP)	1
Borehole televiewer imaging (FAC40)	0.05
Caliper, orientation, total magnetic field (DIP)	5

3.1.1 Temperature (T)

As a passive method, the measurement of subsurface temperature is the first survey that is undertaken during the downward movement of the sonde. Disturbances to the temperature profile, due to turbulence and mixing of borehole fluids, have to be avoided. Hence the temperature is the first measurement undertaken. However, one must always bear in mind that drilling has substantial influence on the thermal environment. Further, the logging speed has to be kept low for the sensor to equilibrate with the surroundings. A temperature profile provides information about thermal anomalies reflecting temperature contrasts between the formation fluid and the borehole fluid. Subsurface temperature increases with depth described by the thermal conductivity λ and the terrestrial heat flow q. The parameter of interest is the geothermal gradient T_z which is the rate of increase in temperature with respect to depth:

$$T_z = \frac{\Delta T}{\Delta z} = \frac{T_f - T_m}{z_2 - z_1} = \frac{q}{\lambda} \tag{3.1}$$

$T_f \ldots$ formation temperature (°C)

$T_m \ldots$ mean surface temperature (°C)

$z_1, z_2 \ldots$ depth of sensor

Changes in the geothermal gradient can imply lithologic boundaries and thermal water influx, which can be caused by fracture zones and permeable formations (Käppler, 2014). Temperature measurements are integral for interpreting the temperature dependent resistivity data.

The absolute temperature measurement at the Kimberly well was carried out by two different sonde types: MP sonde and MS sonde. The Slimhole MP sonde provides the equilibrium temperature of the mud, as well as pressure and mud resistivity. The temperature measurement of the MS Sonde however, serves as a replacement when no data collection with the MP sonde was possible. Besides, the temperature measurement of the MS sonde is meant to correct the magnetic susceptibility values for temperature. Due to combined running of MS and SGR with slow logging speeds of <2 m/min, the MS temperature matches very well with the true MP temperature measurement (Kück, 18.03.2015, pers. comm.).

3.1.2 Caliper (CALI)

The caliper log is designed to determine the borehole diameter d and the borehole geometry. In addition, it reveals the condition of the borehole and is used to provide corrections for other geophysical borehole measurements (e.g. gamma-gamma density log). The caliper measure-

ment in the Kimberly well has been performed with an electro-mechanical 4-arm dipmeter tool (DIP) from the ICDP-OSG. Thereby, the four arms are clamped against the borehole wall and the spreading angle α between the arm and the tool body is measured in the corresponding azimuth in upward movement (Figure 3.2.b).
There are several different types of caliper tools, ranging from a single-arm caliper, which is mostly included in other geophysical borehole tools, to three-, four-, six and multifinger-calipers, whereupon the shape of the borehole can be determined more precisely with increasing number of arms. In contrast to the three-arm caliper, the measurement of d using the 4-arm dipmeter tool is based on two orthogonal azimuths and therefore compensates the misalignment in a deviated borehole (Käppler, 2014). Caused by the ovaloid borehole shape, it can be assumed that a major and minor axis consequently are measured (Hallenburg, 1984). Caliper extensions can be linked to fissured and soluble rocks, which result in open fractures and borehole breakouts. The reason for borehole enlargements goes back to the missing supportive effect of the surrounding rock when the borehole is drilled. This is reflected in increasing stresses along the borehole wall (Reinecker, 2003), and is illustrated in Figure 3.2.a).

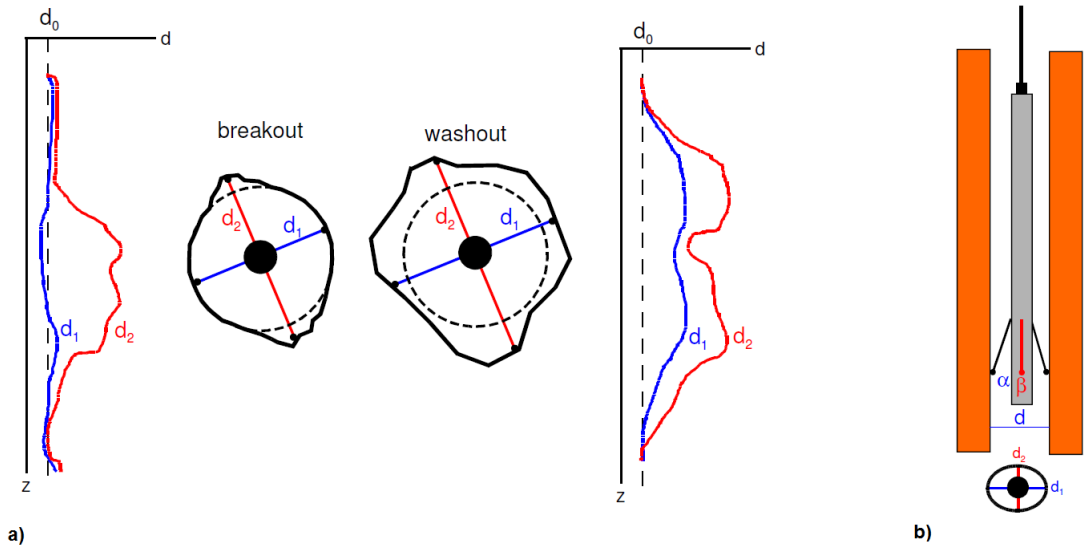

Fig. 3.2: a) Types of enlarged boreholes and their caliper response, b) Schematic of a 4-arm caliper (Käppler, 2014).

Especially in sections with expanding clays or in permeable sections with mud cake construction, the opposite effect, caliper narrowing, is observed. Hence, a caliper log serves as a first assessment for potential fractures, but only acoustic imaging tools such as the borehole televiewer (section 3.1.9) help to cover a 360° all-round view of the geometrical size and shape of the borehole.

Particularly when it comes to the exploitation of hydrocarbon reservoirs, caliper measurements help to set up the comparison of the planned well path with the actual well path. From the angle of inclination I and the direction angle β the coordinates for final borehole depth can be determined and further calculations may provide the true formation depth, position and thickness of the horizons. To comply with those objectives, inclination (DEVI_DIP), direction angle (DAZI_DIP) and the three components of a total magnetic field are measured with the DIP sonde. The determination of the angle of inclination is based on triaxial electronic

accelerometers measuring the decrease of gravity of a mass by deviation from the vertical. The dipmeter consists of a build-in triaxial fluxgate magnetometer whose arc-tangent component ratio of T_y and T_x yields the azimuth to magnetic north β (Käppler, 2014). The caliper recorded by the separately running dipmeter consists of four radii measurements resulting in two caliper curves.

3.1.3 Magnetic Susceptibility (MS)

The MS sonde measures the magnetic susceptibility κ, which characterises the magnetic properties of rocks and magnetic sensitive materials. The magnetic susceptibility serves as the dimensionless ratio between the inductive magnetization $\vec{M}$ and the magnetic field strength $\vec{H}$ (Käppler, 2014). As already mentioned, a three-component magnetometer inside the dipmeter tool measures the absolute value of the magnetic flux density of the Earth magnetic field vector $\vec{T}$ (nT) and its components Z, H.
The magnetic sensor is basically a coil located inside an electrical bridge circuit surrounded by a non-magnetic, non-conductive casing. The Wheatstone Bridge measures the change in electrical impedance due to the change in inductance in one of its arms. Furthermore it can be shown that the change in source frequency required to return the circuit to its original state is proportional to the inductance in one of its arms. Finally the known geometry of the coil inductor tells us that the inductance is proportional to the magnetic susceptibility, as illustrated in Figure 3.3. First, a frequency generator f_G produces an alternating voltage with a frequency of about 1000 Hz and voltage is applied on coil L. During the upward movement of the sonde in the borehole, the inductivity of the previously balanced bridge changes due to the different magnetic susceptibility of the rocks. By changing the frequency with the frequency generator (rheostat), the balance can be restored and this resistor change or frequency change results in the magnetic susceptibility κ (Krammer, 1990; Mwenifumbo & Mwenifumbo, 2012).

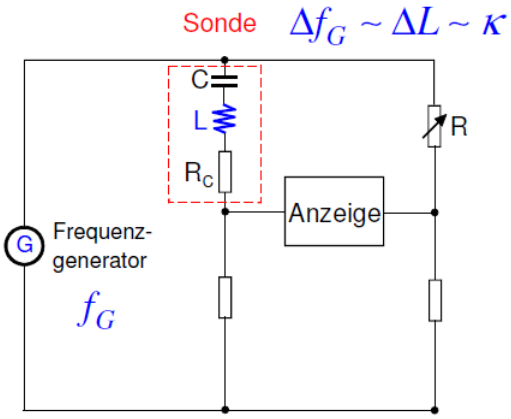

Fig. 3.3: Construction of an electrical bridge circuit to measure magnetic susceptibility (Käppler, 2014).

Rock-forming minerals can be classified as paramagnetic, diamagnetic or ferro (ferri-, antiferro) magnetic minerals. Para- and diamagnetic minerals tend to show low susceptibilities, whereas minerals with ferromagnetic content like iron-titanium (Fe-Ti) oxides are the most important and abundant types showing a high rock susceptibility. Generally, igneous rocks show an increase in susceptibility from acidic towards alkaline rocks, and in terms of sedi-

ments, κ-values do increase with clay content (Käppler, 2014). However, magnetic properties like the magnetic susceptibility vary largely for every rock type and span therefore over orders of magnitude, as Figure 3.4 illustrates.
Specific rock characteristics emerge generally from the geologic genesis and gross mineralogy, therefore magnetic susceptibility is not a good indicator to infer lithological changes. But alteration zones, especially along fractures, can be detected by using magnetic susceptibility measurements as they indicate significant magnetic anomalies (Schön,2011)..

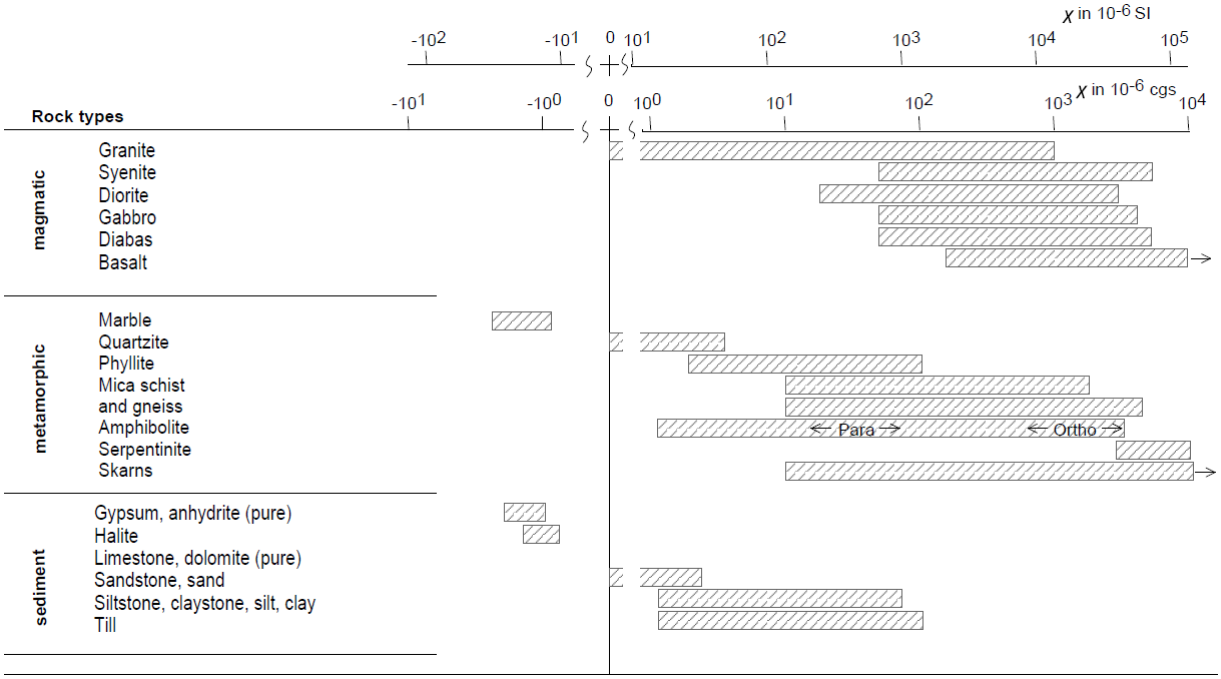

Fig. 3.4: Middle value range of magnetic susceptibility for several types of rocks. Adapted from J. Schön (1983).

Magnetic susceptibility depends on the borehole diameter (bit size), so that chart based corrections are needed to be applied. Those corrections were already carried out by the processing team of the GFZ.

3.1.4 Resistivity (R)

Electric resistivity measurements are active methods obtaining the apparent resistivity R_a (Ω·m) of a non-invaded formation. The borehole and its surrounding rocks are inhomogeneous media separated in several zones with specific resistivity, as illustrated in Figure 3.5. The electric current sent from the current electrode through the borehole subsections to the potential electrode describes the weighted apparent specific resistivity R_a. The objective of resistivity logging is the determination of the true formation resistivity R_t in the undisturbed formation, assuming a homogeneous full-space.
The basic requirement to complete resistivity measurements is a water-based (salt) mud, which functions as a conductor for electricity. For the Kimberly well a dual laterolog (DLL) was used as a focused resistivity system. The advantage of this focused electrode device is a high vertical resolution caused by additional control currents introducing a current laterally and therefore forcing the current to flow in the formation in terms of a flow plate. It can be

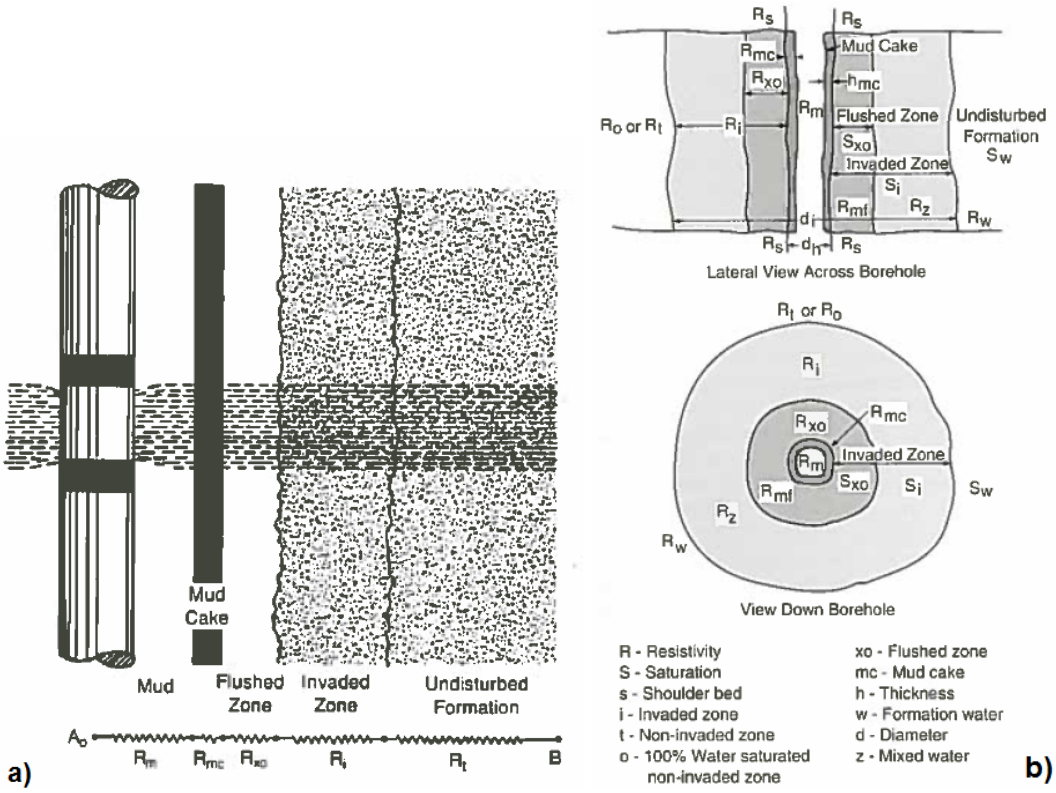

Fig. 3.5: a) Current path of a focused laterolog as it passes through the rock formation (Bigelow, 1995). b) Schematic illustration of formation parameters (Bigelow, 1995).

assumed, due to the deep-reading capability, that the apparent resistivity is approximately equal to the true resistivity of the non-invaded formation. From the true resistivity, rock properties like the porosity, the water saturation level of the pore space and the volume of the clay, can be concluded (Käppler, 2014).

Figure 3.6 shows the dual laterolog providing deep investigation (LLD) and shallow investigation resistivity measurements (LLS). The depth of investigation is controlled by the long guard electrodes A1, A2, A1', A2', which focus the current of the current electrode A0 in the formation. The return electrodes A1', A2' of the shallow laterolog are located inside the device and create only a short investigation depth. Whereas, the large distance between emitting and return electrode of the deeper laterolog minimize the influence of adjacent formations due to the deeper investigation depth. As long as no change of the formation resistivity occurs, the potential difference between long guard electrodes and A0 is zero. The monitoring electrodes M1, M2, M1', M2' are designed to allow no exchange of both currents (Bigelow, 1995; Shazly & Tarabees, 2013).

For the applied log, an invasion depth of about 190 cm for the deep resistivity measurement has been achieved, whereas shallow investigations cover an invasion depth of 60 cm. Laterolog generally achieves good results in coal, limestone and hard-rock environments (Hallenburg, 1984) and is therefore suitable for lower porosity, and high-resistivity formations (Bigelow, 1995).

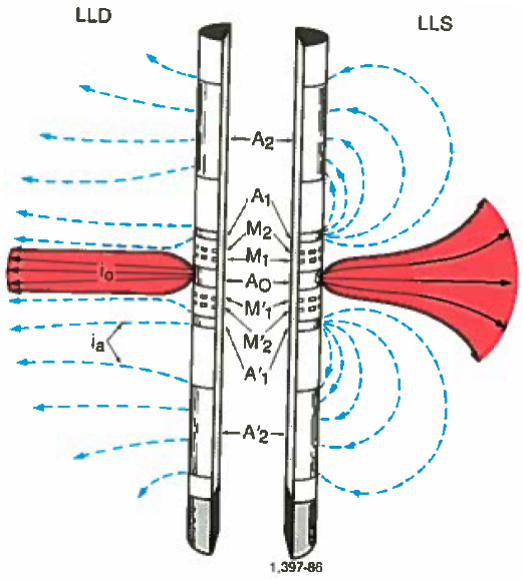

Fig. 3.6: Dual Laterolog - calculated path of stream lines of the deep (LLD) and shallow (LLS) laterolog. The measured current is displayed with stripes (Schlumberger, 1991)

The focused current is a linear combination of the resistivity R_{xo} of the invaded zone and true resistivity R_t of the non-invaded zone. Both zones are normalized with the pseudogeometric factor $J(d_i)$, reflecting the weighted part of the invaded depth (d_i) dependent resistivity from the overall resistivity.

$$R_a = J(d_i)R_{xo} + (1 - J(d_i))R_t \tag{3.2}$$

The shallow focused log will require a higher pseudogeometric factor $J(d_i)$ than the deeper resistivity unit (Käppler, 2014). The pseudogemetrical factor can be read from special pseudogemetrical factor versus invasion diameter charts, as represented by Schlumberger (1991). Generally laterologs are affected to a minor degree by borehole size and bed thickness, but depending on the investigation depth both properties may be influenced differently (Bigelow, 1995). For the measured resistivity at the drill site corrections in this way were not necessary to apply.

Rock forming minerals act as isolators because of their high specific resistivity; but if conductive minerals occur such as oxides, base metal sulphides or graphite, an extremely low specific resistivity is observed (Käppler, 2014). The resistivity is also affected by the conductivity of pore water including salinity of pore water and saturation of pore space. Since through fractures conductive drilling fluid can migrate into the rock formation, resistivity logging is useful for fracture detection in resistive rocks like igneous and metamorphic rocks (Mwenifumbo & Mwenifumbo, 2012). In fractured or porous water-bearing rock, this fact shows up as a decrease in resistivity (Schön, 2011). An overview about the specific electrical resistivity for the most common rock types is presented in Figure 3.7. Besides the rock type, the resistivity depends also on pore structure geometry, the resistivity of the formation water and the amount of water present (Schlumberger, 1991).

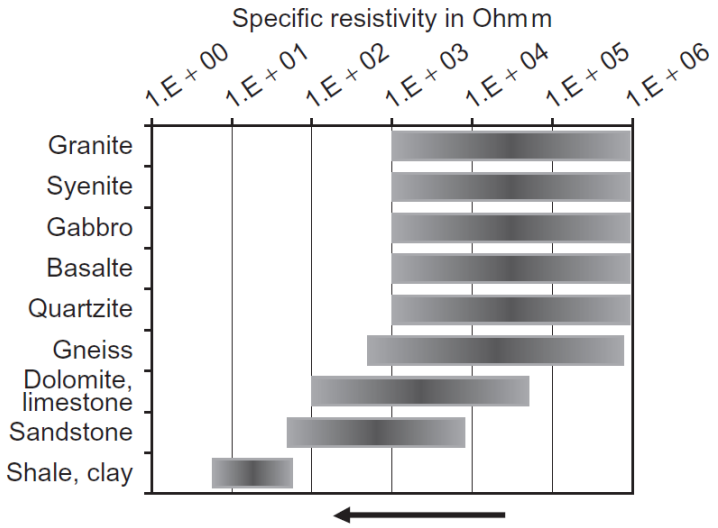

Fig. 3.7: Specific electrical resistivity range for a selection of rock types. For water-filled pores and fractures the arrow does show a decrease in resistivity (J. H. Schön, 2011).

3.1.5 Natural Gamma Ray (GR)

Natural gamma ray logging belongs to the radiometric borehole measurements recording the natural gamma radioactivity of the formation. The origin of the natural gamma radiation goes back to the naturally occurring radioactive elements uranium (^{235}U,^{238}U), thorium (^{232}Th) and potassium (^{40}K) from the formation (Käppler, 2014). Gamma ray logs measure the scattered radiation as a result of the atomic physical Compton Effect, in which atoms loose energy with each collision. Subsequently, the energy-degraded gamma ray will be absorbed by means of the photoelectric effect (Schlumberger, 1991). A detector then records the scattered natural radiation caused by the atomic interactions. In the Kimberly well, the gamma ray detector consisted of a scintillation counter with a sodium iodide (NaI) crystal. The exact operation of gamma ray detectors will be described in the following subsection.

The measurement of the natural gamma ray is based on distinct energy levels resulting in three different principles: Integral measurement, whereupon this survey is referred, selective measurement and the spectral measurement over the whole energy spectrum (section 3.1.6). The measured parameter is the pulse rate N, i.e. the number of detected events per observed time τ, which presents ‚counts per second' (Käppler, 2014). To unify nuclear measurements worldwide, the American Petroleum Institute transferred GR (cps) to the standard unit GR (API). At the University of Houston, Texas, a special calibration pit was designed to establish a standard calibration procedure after the difference in radioactivity between a radioactive cased block section and a non-radioactive one, is equal to 200 API units (Bigelow, 1995). The radioactive decay is a stochastic process, whose statistical fluctuations are also represented in the gamma ray logs. To obtain highly-significant logs, an acceptable logging speed and a sufficiently large observing window τ need to be chosen (Käppler, 2014).

Generally, the natural radioactivity of igneous rocks increases from alkaline to acidic rocks and is mainly affected by uranium- and thorium-bearing minerals (Schön, 2011). The radioactivity of sedimentary rocks is determined by the content of clay present; the higher the percentage of clay the more natural radioactivity is measured.

Gamma ray logs are useful to classify the lithology of sedimentary formations and particularly to determine the shale content of sediments. Moreover, by means of lithostratigraphic marker horizons, a well correlation can be established (Käppler, 2014).

Bücker and Rybach (1996) developed an equation with which the radiogenic heat production, based on total gamma ray measurements, can be calculated in a linear form. The equation 3.3 offers the advantage to determine a simplified heat production when there is only an integral gamma log available.

$$A = 0.0158(GR - 0.8) \tag{3.3}$$

The gamma ray log for the Kimberly well is composed of several sections, because no sonde revealed a complete sampled depth section of the borehole. For the cased section ($<$ 214 m) SGR-MS 018 logging was used for gamma-ray detection. The gamma-ray profile in the open hole section consists of measured results from the telemetry-sonde MS 049, DLL 015, DLL 026, DLL 02. Detailed descriptions about those logging profiles are presented in Appendix A. Natural gamma log, as further interpreted in the log analysis section 3.2, shows measured data without correction of casing effects.

3.1.6 Spectral Gamma Ray (SGR)

In contrast to the total natural gamma ray (GR), gamma ray spectroscopy (SGR) measures the energy spectrum of each of the three radioactive elements potassium, uranium and thorium, and determines their concentration. The natural radioactivity of ^{40}K, detected via monochromatic gamma ray radiation at 1.46 MeV, is the result of its decay into the stable ^{40}Ca element. The decay processes of ^{238}U and ^{232}Th involve multiple steps ultimately leaving behind the stable isotopes lead ^{206}Pb and ^{208}Pb, respectively. The energy spectra of the uranium and thorium decay series lead to a more complex distribution of gamma ray energies (Figure 3.8), but with characteristic peaks of 1.74 MeV and 2.61 MeV due to the bismuth 214 and thallium 208 decay (Käppler, 2014).

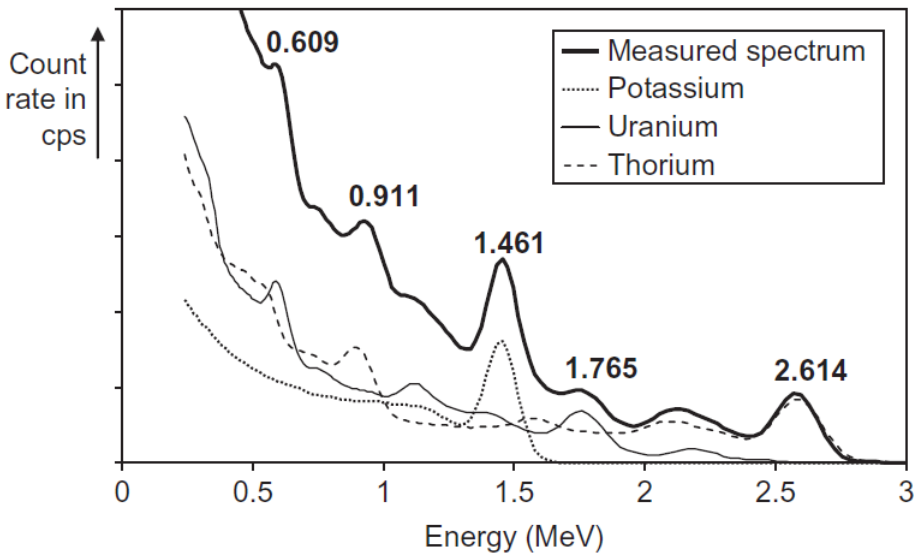

Fig. 3.8: Energy spectra of natural gamma radiation with K, U, Th contents for a shaly formation (J. H. Schön, 2011).

In the Earth's crust, potassium, uranium, and thorium are represented with an average concentration of 2.6 %, 3 ppm and 12 ppm respectively. The measured potassium concentration is always indicated as a percentage (%), because of their abundance in nature (Schlumberger, 1991). Table 3.2 reflects the frequency of radiogenic elements for common rock types. The listed radiogenic concentrations of rhyolite, basalt and sandstone give an overview of the gamma ray distribution in the survey area.

As for the measurement of the total natural gamma radiation, a scintillator detector is used, which consists in this case of a caesium iodide (CsI) crystal optically coupled to a photomultiplier tube. When the SGR-sonde passes through the borehole, ionized radiation of the formation will enter the crystal. Due to the crystal lattice, the electrons are trapped and produce free electrodes as they move around. If they collide with impurity atoms like thallium, they impart their energy and activate the thallium impurity. By emission of visible light, those decompose to their initial state. The photomultiplier tube detects this light and transforms it into an electrical pulse (Ellis & Singer, 2007).

The element specific energy spectra overlap with the total spectrum observed in measurement. The decay processes are additive and scattering processes within the apparatus cause a smearing of the overall curve (Fig. 3.8). Hence, corrections of radioactive element interactions need to be applied. Borehole size and mud weight are also factors requiring corrections (Käppler, 2014; Schlumberger, 1991).

In addition to lithologic structuring of sedimentary formations, spectral gamma ray logs are important indicators for clay, and are able to determine the type and volume of clay. They allow to identify and evaluate radioactive minerals by means of their potassium and thorium concentrations. Schlumberger (1991) developed a cross-plot in which potassium und thorium concentrations are matched with known minerals. It appears that high potassium concentrations are typical for glauconitic sands, micaceous sands, as well as illite clays, whereas bentonite correlates with high concentrations of thorium. However, due to mixtures of clay minerals, a precise mineral classification within Schlumberger's identification chart is not guaranteed.

A further area of application of gamma ray spectroscopy with reference to geothermal energy production is the determination of radiogenic heat production A. Bücker and Rybach (1996) introduced a formula to calculate the radiogenic heat production by using the concentrations of the radioactive elements measured by the SGR sonde:

$$A = 10^{-5}\rho(9.52c_U + 2.56c_{Th} + 3.48c_K) \tag{3.4}$$

$A \ldots$ heat generation in $\mu W/m^3$

$\rho \ldots$ rock density in kg/m^3

$c_U, c_{Th}, c_K \ldots$ uranium, thorium and potassium concentration

All these fields of application are further discussed and employed in the interpretation section (Section 3.2). The entire spectral gamma ray log of the Kimberly borehole was corrected for drill pipe attenuation and hole size below 213 m by the OSG processing group.

Tab. 3.2: Compilation of potassium, uranium and thorium contents for some rocks. Reference key: BA-Baker Atlas (1985); Sch-Schlumberger (1982); Kae-Käppler (2014), Schoen - Schoen (1983). Adapted from Schön (2011).

Rock Type	**K in %**	**U in ppm**	**Th in ppm**	**Reference**
Intrusive				
Granite	2.75-4.26 3.4-4.0	3.6-4.7 4-7	19-20 15-40	BA Schoen
Granitic rocks (average)	4.11	4.35	15.2	Sch
Gabbro, diabase	0.7 0.46-0.58	0.6 0.84-0.90	1.8 2.7-2.85	Schoen Sch
Extrusive				
Rhyolite	4.2 2-4	5.0 2.5-5	 6-15	BA Sch
Basalt	1.0	0.7	2.3	Schoen
Alkali basalt	0.61	0.99	4.6	BA, Sch
Plateau basalt	0.61	0.53	1.96	BA, Sch
Sediments				
Sandstone (range, mean)	0.7-3.8 1.7	0.2-0.6 2.9	0.7-2.0 10.4	BA Schoen
Argillite, clay, argillaceous schist	2.7	4.0	11.5	Schoen
Limestone	0.3	1.6	1.8	Schoen
Gypsum, anhydrite	0.02	1.0	1.0	Schoen

3.1.7 Neutron Logging

The main application of neutron logs is the determination of the apparent porosity of the formation. Neutron measurements use the neutrally charged neutrons, which have a mass similar to that of a hydrogen atom, to detect water in the pores or oil filled formations. Three different types of neutron signals (logs) can be distinguished according to the energy level of the detected neutron: thermal neutrons (En $<$0.025 eV), epithermal (0.025 eV $<$ En $>$ 100 keV) and fast neutrons as GR interaction (En $>$ 100 keV). The measuring system consists of a neutron source emitting high-energy neutrons and at a certain distance a detector that measures the slowed down neutrons. The energy loss is due to interaction processes of the neutrons and hydrogen atoms in the formation. Therefore, the more hydrogen a formation contains the less neutrons are counted in cps-unit at the detector (Käppler, 2014; Schlumberger, 1991). The working principle described above is illustrated in Figure 3.9.
Hydrogen functions as an efficient absorber due to its small mass and large scattering cross section (Ellis & Singer, 2007). Helm-Clark, Rodgers, and Smith (2004) defined neutron log applications, which are useful to define features in basalt or in other rock types. Thus, neutron logs provide insight into fracture zones, alteration, flow breaks, interbeds, and the thickness of an existing aquifer.

The porosity is very sensitive to pore space and mineral composition, additionally the presence of low-density hydrocarbons and shale also disturb the accurate determination. If clays are highly saturated with water, porosity may be calculated incorrectly. Therefore, the determination of porosity is only successful when no shale is present, the matrix lithology is

known, and liquid-filled pores exist. Otherwise, porosity does not yield to accurate results (Ellis & Singer, 2007).

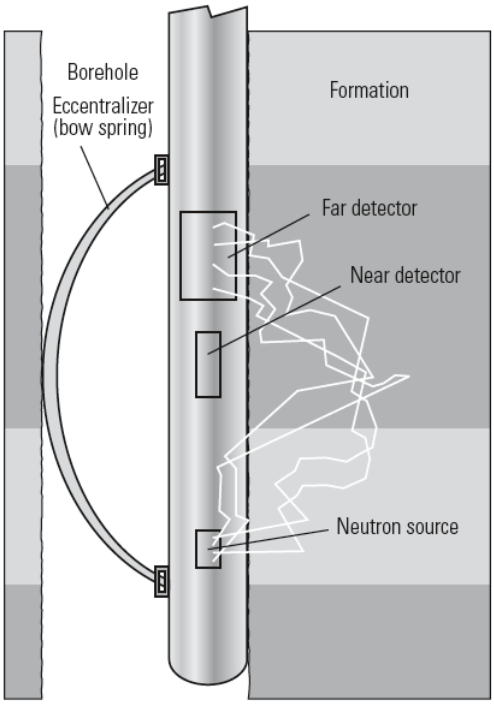

Fig. 3.9: Schematic of thermal logging tool, showing the functionality of the sonde (Ellis & Singer, 2007).

3.1.8 Full Waveform Sonic (FWS)

During the geophysical borehole logging program at the Kimberly well, a full waveform sonic has been acquired to determine the acoustic travel times in the form of full sonic waveform pictures. As an acoustic measurement, the formation in the open hole is examined with elastic refracted waves. Simple sonic logs (DT) just yield the travel times for compressional waves, but, by taking a probe as the BS-sonde, compressional wave (p-wave), shear wave (s-wave), and Stoneley waves are obtained. In this case, the acoustic logging tool consists of one transmitter and two receivers with piezoelectric transducers each having a resonant frequency of 15 kHz. To ensure a good acoustic coupling the wellbore must be water-filled. The principle of the full waveform sonic is illustrated in Figure 3.10.
The interval travel time Δt (slowness), indirectly recorded in the full waveform sonic picture, equals the difference in arrival of an elastic wave at the receivers. In the way of using two or three receivers, the sonic log compensates for borehole effects and sonde tilt. From the individual times stored in the waveform picture and the known receiver spacing of 0.5 m ($\overline{E1E2}$), the formation velocity can be calculated with equation 3.5 and 3.6.

$$\Delta t = \frac{t(E2) - t(E1)}{\overline{E1E2}} \tag{3.5}$$

$$v_{Formation} = \frac{10^6}{\Delta t} \tag{3.6}$$

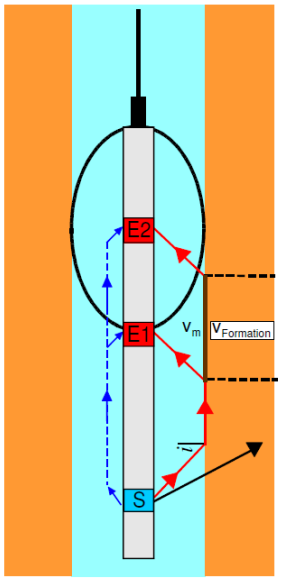

Fig. 3.10: Schematic of an acoustic logging tool (Käppler, 2014)

Due to the direct measurement in the borehole, sonic logs provide accurate time-to-depth correlation, which support surface seismic records. Since the velocity is pressure dependent, zones with anomalous high pressures can be identified (Bigelow, 1995). After calculating the acoustic travel times, parameters like permeability or porosity can be derived. M.R.J. Wyllie (1956) developed a relationship between the sonic velocity (acoustic travel time) and the porosity in a time averaged equation:

$$\frac{1}{v_p} = \frac{1-\Phi}{v_{p,ma}} = \frac{\Phi}{v_{fl}} \tag{3.7}$$

$$\Delta t_p = (1-\Phi)\Delta t_{p,ma} + \Phi \Delta t_{fl} \tag{3.8}$$

$$\Phi = \frac{\Delta t_p - \Delta t_{p,ma}}{\Delta t_{fl} - \Delta t_{p,ma}} \tag{3.9}$$

v_p ... compressional velocity of the formation

$v_{p,ma}$ ... compressional velocity of the pore free rock matrix

v_{fl} ... velocity of pore fluid (water)

Φ ... fractional porosity of the rock

The classification of velocities for specific rock types takes place over a wide range of velocities (Figure 3.11). For igneous rocks, an increase in velocity from acidic (felsic) to basic (mafic) rocks is observed. For sedimentary rocks, it is common that denser (low porosity) rocks have higher velocities, whereas porous rocks tend to show a decrease in velocity. Therefore, porosity and pore fluid influence the strongly influence the velocity (Schön, 2011). An additional benefit of sonic logging is the detection of fracture zones, which is characterized by a decrease of compressional and shear-wave velocities. Furthermore, the lowering in amplitude for all three waveforms is an indication for the presence of fractures (Mwenifumbo & Mwenifumbo, 2012).

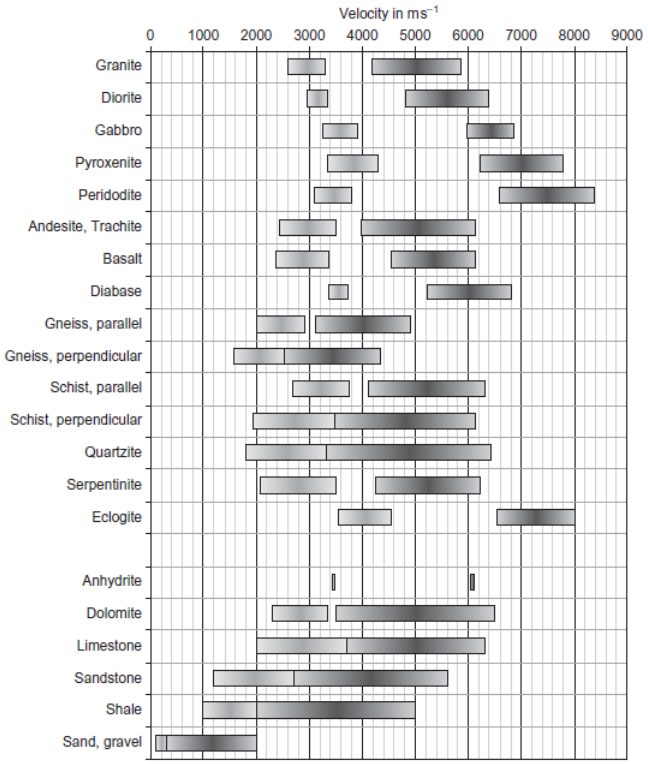

Fig. 3.11: Compressional (higher bar) and shear-wave (lower bar) velocities for common rocks (J. H. Schön, 2011).

3.1.9 Borehole Televiewer (FAC40)

The borehole televiewer (BHTV) yields images for the full 360 ° of the borehole by scanning it with an ultrasonic beam. The reflected signal from the interface between borehole fluid and borehole wall is characterized by transit time and amplitude. The borehole televiewer images (FAC40) obtained in the Kimberley well are created by a the rotating transducer with a frequency of 1.4 Hz. By transferring the signal on a cathode-ray tube screen, the azimuthal position for every borehole depth is presented, and gives the interpreter indications for structural and lithologic features (ALT sàrl, 2002; Hallenburg, 1984).

The orientation system consists of three-axis fluxgate magnetometers and three accelerometers allows the determination of the accurate position of the tool within the borehole (Williams & Johnson, 2004). Using logging speeds of just 1-3 m/min and a high vertical resolution of 5 mm, the borehole televiewer can achieve a high resolution independent of depth. In contrast to optical televiewers creating photographs of the borehole wall, the acoustic televiewer can be used in turbidly drilling fluid (Käppler, 2014). The most common applications for the borehole televiewer are the analysis of breakout events, the detection and evaluation of fractures, monitoring of Earth stress fields, lithological interpretation, detection of thin beds and bedding dips (Williams & Johnson, 2004). Although the televiewer is normally employed in the open hole section, it can be used for casing inspections. The information obtained by the caliper log can be extended to a higher resolution by the televiewer. If a fracture is present, as indicated in Figure 3.12, the reflected signal will emerge as a sinusoidal feature on the televiewer output. From the measured diameter of the borehole (cal) and the height (Δz) of the sinusoidal curve the dip of the fracture plane can be determined.

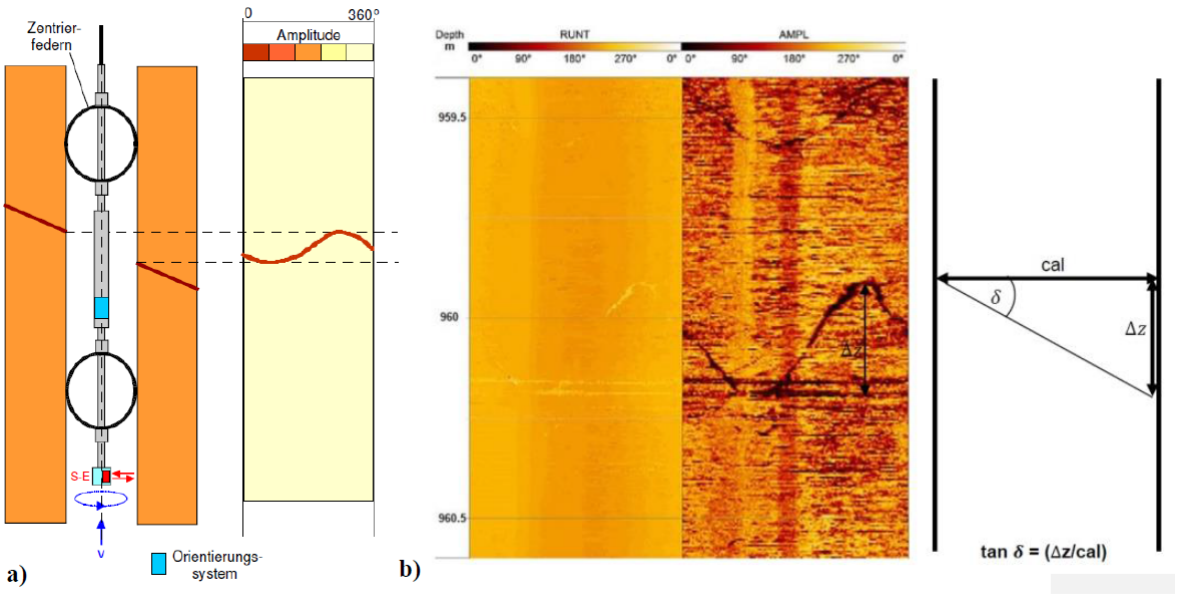

Fig. 3.12: a) Schematic of acoustic borehole televiewer detecting a subvertical fracture (Käppler, 2014). b) Sinusoid curve of natural fracture on a 360° view of the BHTV image. This image was taken from the Kimberly BHTV image logs in WellCAD at 959.5-960.5 m.

Problems may derive if the acoustic televiewer is decentralized, then amplitudes and transit times appear vertically striped. Furthermore, the aperture of the natural fractures may be increased by the drilling process (Williams & Johnson, 2004).

3.2 Logging Analysis

Within the ICDP HOTSPOT project, the collected geophysical logging data has already been processed by Jochem Kück (GFZ). Nevertheless, those results shall be extended with lithologic results by Christiansen et al. (n.d.) and Knott et al. (n.d.), and be subjected to a detailed analysis and interpretation with a particular focus on fractures. In this context, caliper extensions, a decrease in bulk density, a decrease in resistivity, a delay in travel times, as well as sinusoidal or straight line features on the borehole televiewer images are possible log responses concluding to fractures (Schlumberger, 1991).

Prior to interpretation, all logs were aligned with respect to the depth measurement of the GR-Master log. This reference log is based on the natural gamma ray response of the telemetry-sonde, consisting of several open hole logs and one cased hole log. According to the processor Kück (18.03.2015), depth corrections were carried out on parts where alignments matched, but below 630 m the uniform GR profile makes it difficult to correlate the data accurately.

3.2.1 Rock Characterization

Through the extended core sampling at the Kimberly well covering the open hole from 214-1957 m drilling depth, we obtained a good overview of the lithology. It is aimed to compare the results from the core sampling with the geophysical log response, to derive further statements on mineral composition, alteration, and allocation to geological formations. The results concerning the interpretation of the geophysical bore hole logs are summarized in Figure 3.14.

Through the passing of the hotspot in the Twin Falls area 10 to 12 Ma ago, the oldest volcanic rocks, such as pyroclastic deposits and ash flow tuffs, belong to the Idavada Group. This also includes the Twin Falls rhyolite (Shoshone rhyolite), comprising mostly of the basement in this area, which is exposed 6.5 Ma years ago about 3 km NNW of the drill site in the Snake River Canyon at Shoshone Falls. Between the eruptive phases, this formation was overlayed with fine-grained lacustrine sediments like mudstone, siltstone or shale. Those sedimentary layers are associated with the Pliocene Glenns Ferry Formation. However, at a few places, flows of the Twin Falls rhyolite did also overlay the sediment. The second type of volcanism found in this region is represented as basalt flows covering and intercalating with sedimentary layers (Shervais et al., 2011).

The Kimberly well is an extract of this volcanic and stratigraphic history in the Twin Falls area exposed in three main rock types: Basalt, sediment and rhyolite (three units). The basaltic flow units are characterized by low natural gamma radiation with < 20 API, which can be distinguished quite well from sedimentary layers and rhyolite. For the spectral parts of the natural gamma log, very low concentrations of uranium and thorium were measured. In particular, the spectral signature is dominated by the potassium content; those observations are generally observed in basalts (Helm-Clark et al., 2004). The neutron log shows a very significant response as the neutron flux increases from the top to the bottom of basalt flow. This observation is also seen in logs of the Columbia River Basalt and in saturated basalt flows on the eastern Snake River Plain. Helm-Clark et al. (2004) interpreted this increase in neutron flux as a decrease in porosity for saturated basalt flows. In the upper 109 m occurring plain basalt is the result of local shield volcano eruptions (Christiansen et al., n.d.). Because this section was not cored, Christiansen et al. (n.d.) presumes that this flow may be correlated to other olivine tholeiitic basalts from Hansen Butte and older vents.

By the abrupt increase in natural gamma and potassium radiation, the following rhyolite

section of almost 130 m thickness can be differentiated from the basalt flows. From core photos, televiewer results, and interpretations by Knott et al. (n.d.), the lower 5 m rhyolite can be classified as auto-brecciated[1] basal vitrophyre[2]. This brecciated unit, as well as the 2 m thick loess layer at the top of the underlying basalt, is characterized by low velocities and an increasing caliper. A photograph of the rhyolite-loess transition is displayed in Figure 3.13 a). The reason why the section immediately below the cement casing to the loess-basalt contact shows a sudden increase at the natural and spectral gamma ray logs remains unanswered. A possible justification may be a different mineral composition and grain size, as for the rhyolite above. The loess-basalt contact, represented in a rapid decrease of gamma radiation, is shown in Figure 3.14. Geochemical analysis of this rhyolite lava flow by Christiansen et al. (n.d.) revealed the highest Fe-Ti oxide concentrations from all rhyolite intersections and showed plagioclase, K-feldspar, pigeonite and augite components. Based on this result together with the characteristic gamma ray response, this rhyolite will be classified as rhyolite 3 in this thesis. As described before, this flow indicates correlation to the Shoshone Falls rhyolite, which erupted on sediment and basalt intercalations from an older caldera. Research done by Helm-Clark et al. (2004) shows that other logs collected in the eastern Snake River Plain, also detected high gamma counts within the interbeds, related to loess deposits near the Moon National Monument. A presumption might be that the lower rhyolite 3 and the loess interbed are related to similar features observed in the Eastern Snake River Plain. However, the thin loess section is resolved too poorly to draw conclusions.

The subsequent inter-bedded strata of basalt and sediment between 238 and 426 m represents the filling of the Twin Falls Caldera, whereas low gamma ray responses of < 15 API are related to basalt flows from the olivine tholeiite type including phenocrysts of plagioclase and olivine. All in all, the natural gamma values for basalt are in agreement with the natural gamma ray range of 5-50 API for basalt, found by Helm-Clark et al. (2004).

The intercalated sedimentary layers show typical gamma ray values of 100-150 API. Both sedimentary layers, 269-292 m and 355-426 m, are parallel-laminated, marly structured sandstones and mudstones interpreted by Shervais et al. (2013) as lacustrine sediments often occurring in the intra-caldera lakes of the Snake River Plain as noted by Christiansen et al. (n.d.). The relatively high values of GR and SGR indicate sediments with clay-rich content. The transition between sediment and rhyolite is quite blurred and the identification as a sediment horizon is only supported by consistent potassium values; the total gamma ray and the uranium and thorium values do fluctuate strongly but generally increase with depth.

A different eruptive rhyolite unit referred to as rhyolite 2 by Knott et al. (n.d.) between 426 and 605 m is indicated by high gamma ray values of 200-250 API. A continuous rise in natural gamma radiation and magnetic susceptibility from the top of the rhyolite to 468 m are associated with auto-brecciation that is more hydrothermally altered near the top of rhyolite 2. An highly hydrothermally altered layer of rhyolite is shown in Figure 3.13 b). The consistent GR, SGR and MSUS logs from 469 to 597 m provide indication for a change in the rhyolite 2 structure, which Knott et al. (2013) described as flow-banded lithoidal rhyolite. Geochemical analysis classified this type of rhyolite as silica rich (Christiansen et al., n.d.).

[1] Autobrecciated lava = „A viscous, commonly silica-rich, lava flow with a congealed crust which has been broken up and fragmented by the continued movement of molten lava within the flow interior. Stressed and deformed by the movement, the crust may fracture in a brittle manner, producing angular, smooth-faced blocks able to weld together if they are hot enough but which otherwise become incorporated into the moving interior of the flow.“ (Allaby, 2008)

[2] Vitrophyre = „Any porphyritic igneous rock having a glassy groundmass.“ (Bates & Jackson, 1984, p.554)

Based on the strong decrease of natural and spectral gamma radiation, beginning at 597 m depth with a minimum between 605 and 616 m, the core-sampled sedimentary layer (Figure 3.13 d)) may be comprised of different grain sizes and mineral compositions. By comparing the sedimentary layers with each other, it can be stated, according to the core photographs, that the low API response is associated with decreased clay content. Christiansen et al. (n.d.) stated that the sediment accumulation in this section may be caused by collapse of the 1340 m thick underlying rhyolite tuff.

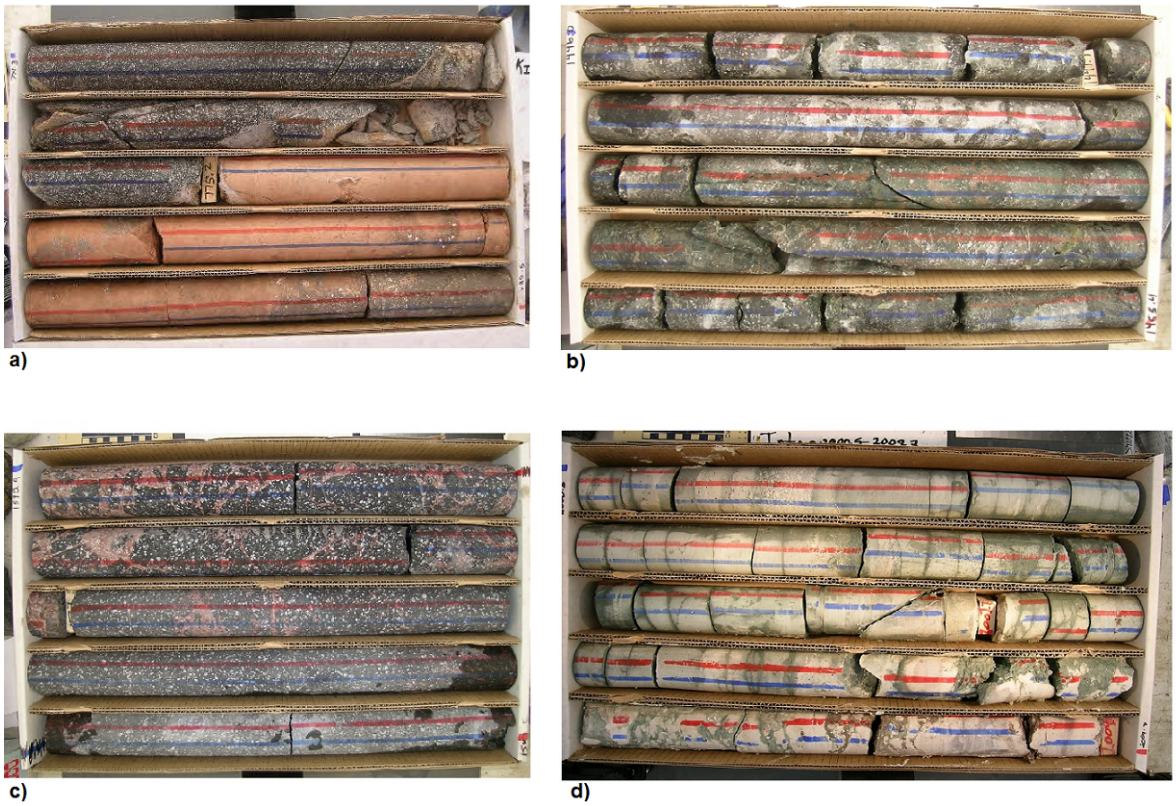

Fig. 3.13: Selected core boxes of the Kimberly well showing distinct lithological and textural features. a) Loess section at 236.28-238.41 m, b) Auto-breccia hydrothermal altered at 441.26-444.31 m, c) Autobrecciated vitrophyre at 468.48-471.62 m, d) Parallel-laminated, fine lacustrine sediments at 609.75-612.56 m

Both the total magnetic field and the GR logs provide proof of the uniform rhyolite section below 616 m until total drilling depth, referred as rhyolite 1. The first 24 m of the rhyolite 1 are again auto-brecciated and hydrothermally altered, implied by a rise in GR. Bore hole cores revealed a densely welded rhyolite ignimbrite with lithoidal zones containing sparse vitric lapilli(1-5 mm size). Furthermore, folding with an increasing angle with increasing depth is visible (Knott et al., n.d.).

Whole-rock chemistry by Christiansen et al. (n.d.) revealed that all three rhyolite units are within-plate rhyolites (A-type rhyolites) showing similar geochemical compositions as other rhyolite in the central Snake River Plain. Geochemical measurements exhibit high TiO/MgO and Fe/Mg ratios, high concentrations of alkalies and moreover with the high concentrations of Nb,Y, and Zr the classification of three distinct eruption units was proven. Kimberly rhyolite 2 showed, in comparison to the upper and lower rhyolite 3 and 1, a richer silica concentration that allows reference to a more evolved rhyolite. These results, indicating three eruptive units, are also supported by paleomagnetic inclination measurements (Christiansen et al., n.d.).

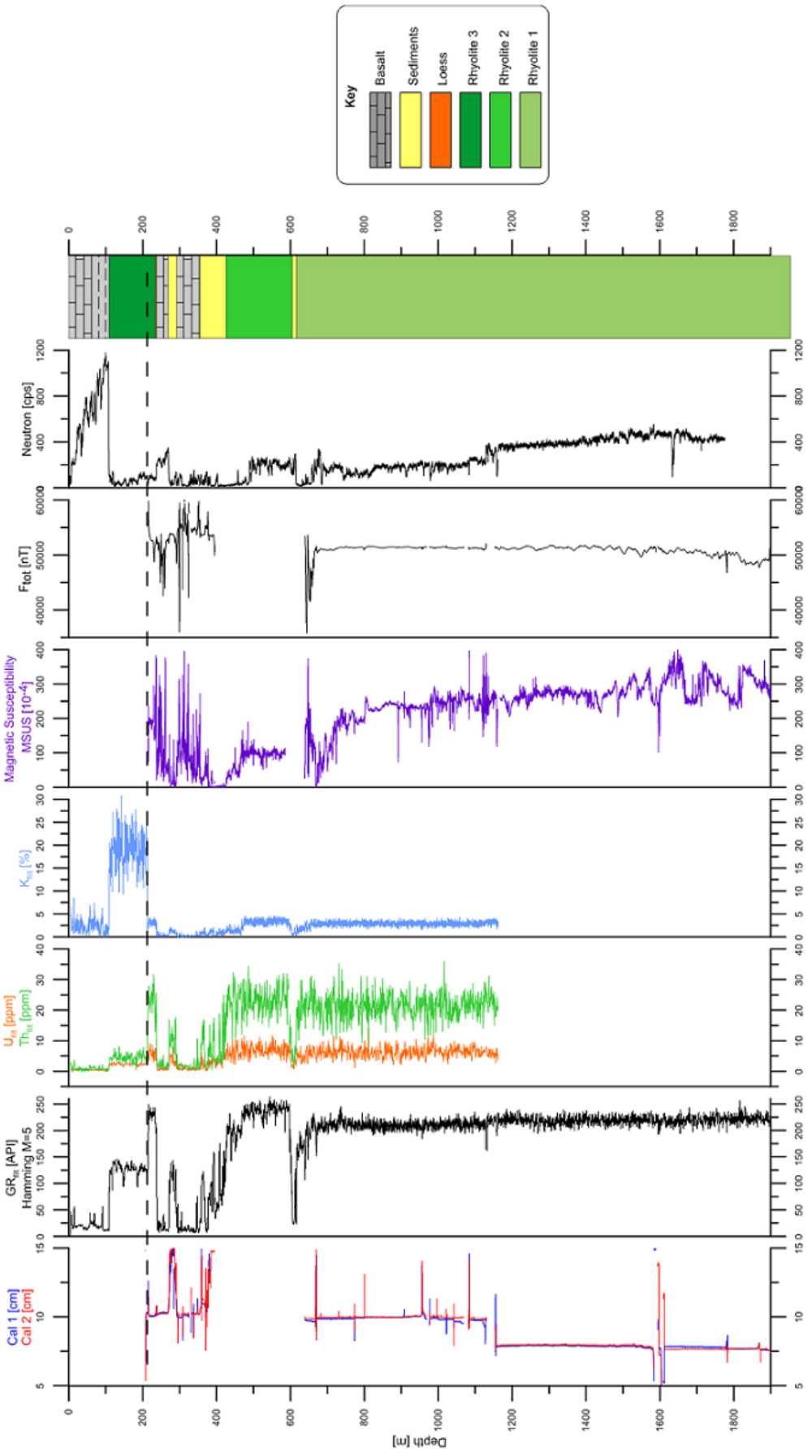

Fig. 3.14: Geophysical borehole logs acquired at the Kimberly drill site and concluding lithology log. Total and spectral gamma ray logs were filtered with a 5-point Hamming window.

3.2.2 Fracture Detection

The detection of fractures is a procedure managed most precisely when geophysical well logging methods are combined. Only if e.g. planar features are observed, both in acoustic image logs and core scans, conclusions about the morphology, orientation and aperture of the fractures are possible. A strong decrease in resistivity and acoustic velocity does indicate that a bigger fracture or a possibly broader brittle zone may exist, where fluid migration can occur.

With the help of the geophysical software package WellCAD^{TM} by Advanced Logic Technology (ALT), quantitative information about the character and the orientation of the fractures were derived. The identification of fractures was based mainly on the depth sections, which were covered by borehole televiewer and full waveform sonic logging runs. Therefore, depth sections between 211-388 m and 635-1128 m were sampled in detail and provide information about the fracture state in three different lithologic units.

The orientated image logs of the FAC40 can reveal three main fractures types: Natural fractures, drilling induced fractures (DIF) and borehole breakouts.

Natural fractures, which were already illustrated in Figure 3.12, can be interactively picked by the structure log in WellCAD^{TM}. Here, a curve can be fitted to the observed sinusoidal feature (or sometimes horizontal feature) and information about the depth, dip angle, azimuth (strike) and aperture is stored. Figure 3.16 illustrates fracture and flow-banding orientation in form of a rose diagram for the two main depth sections, where acoustic televiewer images have been acquired. Dipping angles scatter over a wide range but about 75% of the natural fracture events lie within a dipping angle range from 15° to 65° at depth between 211-388 m. A similar relationship is seen for dipping angles at depth of 635 to 1160 m, whereas (mean) dipping angles in this case generally grow with an increase in depth (Table 3.3).
For both depth sections higher dipping angles can be attributed to step dipping vertical fractures, extending vertically sometimes over several decimeter. Flow-banding in the sediment and basalt section is associated with weakly dipping features, covering a range of 11° to 30°. Although flow-banding for the rhyolite 1 was associated with comparable small dip features, some layered textures are characterized by steep dipping angles. Knott et al. (n.d.) also confirms the distinct foliation of the thick rhyolite section with a varying degree of dip. From the analysis carried out in this thesis and supported by Knott et al. (n.d.) it appears that foliation below the vitrophyre at around 650 until 770 m is dominated by various changes in high and low dipping events. Knott et al. (n.d.) notes that this may be due to rheomorphic folding of the layered texture. Moreover, the azimuthal distribution of the textural layering alternates from east striking to northwest striking events back to east striking events in the upper rhyolite 1 unit. The remaining lower part of rhyolite 1 indicates low or sub-horizontal layering (Knott et al., n.d.).
The strike regime of the fractures in the Kimberly well appears to be very complex (Figure 3.16). For most of the features examined, the direction of their strike is E-W, respectively ENE-WSW.
As part of the detection of natural fractures, open and gouged-filled fractures were distinguished. For open fractures the true aperture was determined, yielding an aperture of $<$ 1cm for almost all counted features. Only single fractures with adjacent fissured rocks showed apertures of up to 6 cm.

Tab. 3.3: Statistical overview of fractures geometry interpreted from FAC40

Top depth (m)	Bottom depth (m)	Counts	Mean dip angle	Min-Max dip angle	Mean strike	Min-Max azimuth	Type
211	388	85	40.69	6.67-80.61	185.27	4.67-358.05	Natural Fracture
211	388	8	3.81	11.65-30.11	164.18	36-349.22	Bedding
635	1160	318	57.16	5.51-86.77	167.37	0.06-359.81	Natural Fracture
635	1160	118	49.41	13.61-86.64	164.71	0.92-358.41	Bedding

Drilling induced fractures (DIF) are characterized by narrow zones along the borehole axis and are often separated by 180° or sub-parallel. As natural fractures, DIFs occur on the amplitude images of the BHTV as sharp low reflectivity zones. Drilling induced fractures are created when the surrounding stresses exceed the normal stress regime. This tensile failure is orientated in maximum horizontal stress direction (Tingay, Reinecker, & Müller, 2008). Corresponding to the applied stresses, four types of core fractures are known: Petal, centerline, petal-centerline and core edge fractures, which are schematically illustrated in Figure 3.15.
Some very prominent drilling induced fractures were visible in the acoustic televiewer images, however, this detection was not supported by images of core scans. Therefore, drilling induced fractures were not included in the interpretation.

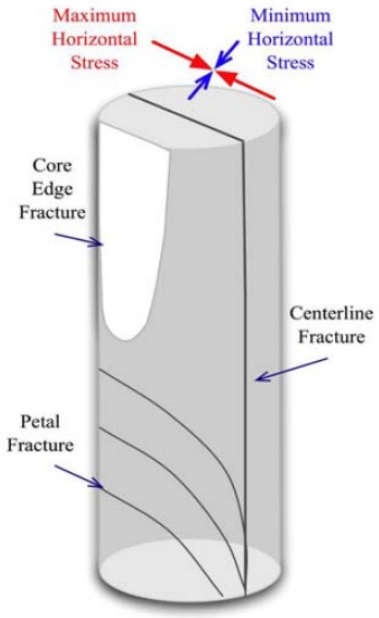

Fig. 3.15: Schematic of centerline, petal and core-edge drilling induced fractures and the direction of the main two horizontal stresses (Patlan, n.d.).

Borehole breakout, referred as stress-induced enlargement of the borehole radius, is another feature, which is sometimes seen in BHTV images as zones of low amplitude. A rough surface along the enlargement of the wellbore is typical, as conjugate shear plane intersect each other and are developed in minimum horizontal stress direction (Tingay et al., 2008).

Although image resolution was good for most of the sampled sections, sedimentary and brittle zones were sometimes poor in quality and hard to interpret. The sinusoidal curve fitting was complicated in zones with more complex fractures. Therefore, some dips and strikes scatter, resulting in a wide range of orientations of events. As sub-vertical natural fractures are highly dipping, and drilling induced fractures are vertically aligned, both fracture types are sometimes hard to distinguish.

But fractures are, as already mentioned in section 3.1.4, represented by decreased resistivity values of the dual laterolog. In the case of open fractures, the response of the dual laterolog will be lowered and by the ratio of shallow and deeper laterolog to one another, the type of fracture, vertical or horizontal, can be derived. In the case of shallow and deeper resistivity separation (R_{LLD}>R_{LLS}) a vertical fracture can be assumed, whereas a sharp decrease in R_{LLD} indicates a horizontal oriented feature (Shazly & Tarabees, 2013).

As dual laterolog measurements were only obtained below 640 m, statements regarding the confirmation of natural fractures in the sediment and basalt sections, represented in declines in resistivity, cannot be confirmed. In general, fissured zones, seen in BHTV images for the massive rhyolite flow, show decreases in both shallow and deep resistivity measurements. At a depth of 1077.5 until 1127.5 m shallow and deeper resistivity drift apart confirming the existence of subvertical fractures in this section. However, the dispersed resistivity logs do not indicate specifically remarkable fractures. The most striking resistivity decreases are seen at depths of 644-656 m, 668-672 m, 892 m, 925 m, 957 m, 973-977 m, 999 m, 1021-1025 m, 1137 m and 1158-1160 m (Figure 3.17). Especially the last measured lower resistivity value at around 1160 m does correlate to decreases in magnetic susceptibility and GR. Televiewer results also indicate many fractures around this depth section. The end depth of this decreased resistivity zone is beyond available depth data of the dual laterolog but a rise in sonic velocity implies that the fractured zone ends at 1162 m.
Below this depth, resistivity values increase consistently, leading to the conclusion that rhyolite goes into more resistive hard-rock environment. Nevertheless, at depths of 1590-1602 m and 1785-1805 m broader decrease in resistivity is observed, indicating fractured zones. All in all, shallow and deep resistivity measurements do fluctuate heavily for the deepest measured data, as seen on panel 3 in Figure 3.17. Unfortunately, due to missing televiewer images in the deepest 700 m of the rhyolite 1, decreases in resistivity cannot be matched properly with possible natural fractures, DIFs or borehole breakouts.

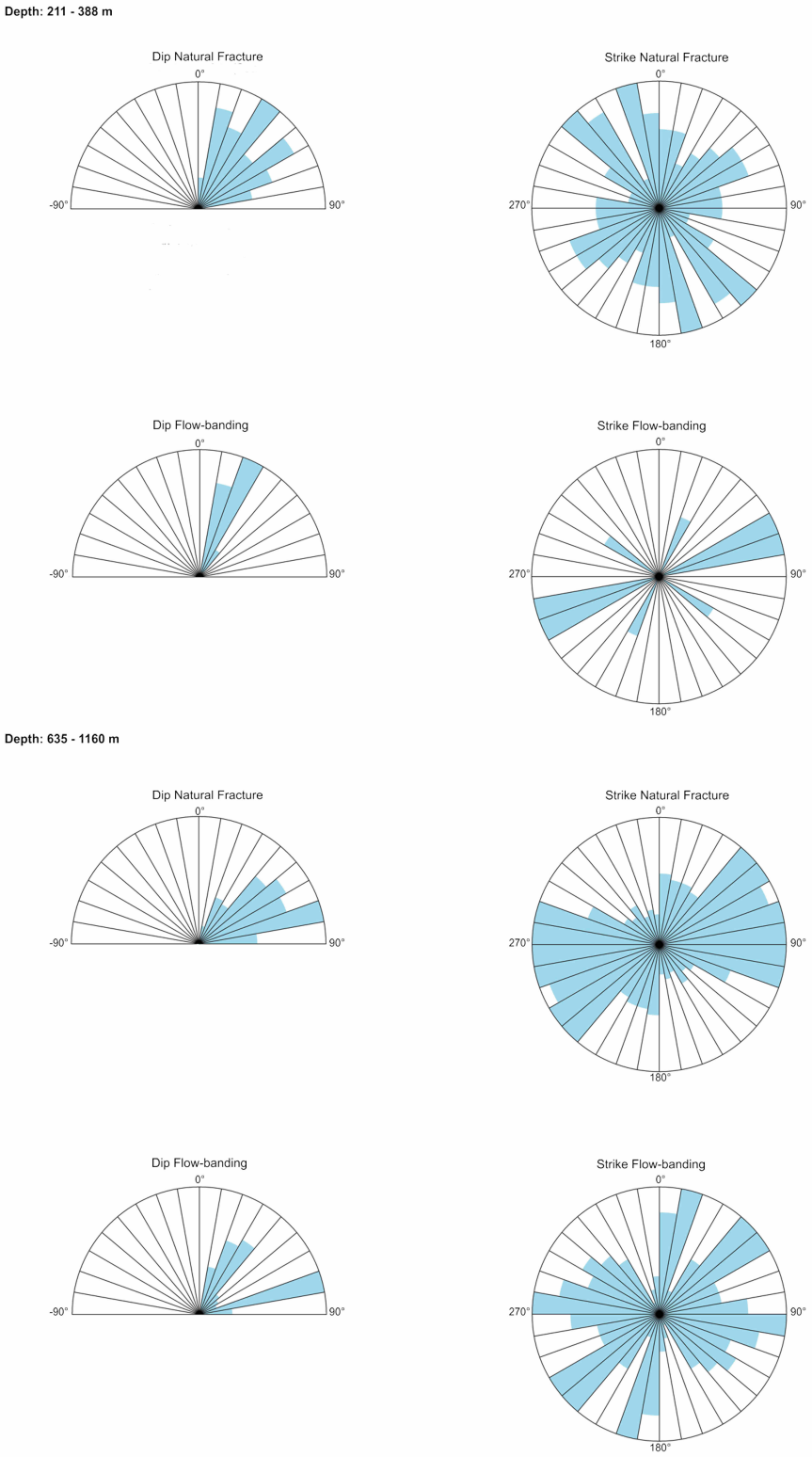

Fig. 3.16: Interpreted fractures and flow-bandings in form of rose diagrams in the Kimberly well for two depth sections. The left panel represents the dip and the right panel the strike of the planar features.

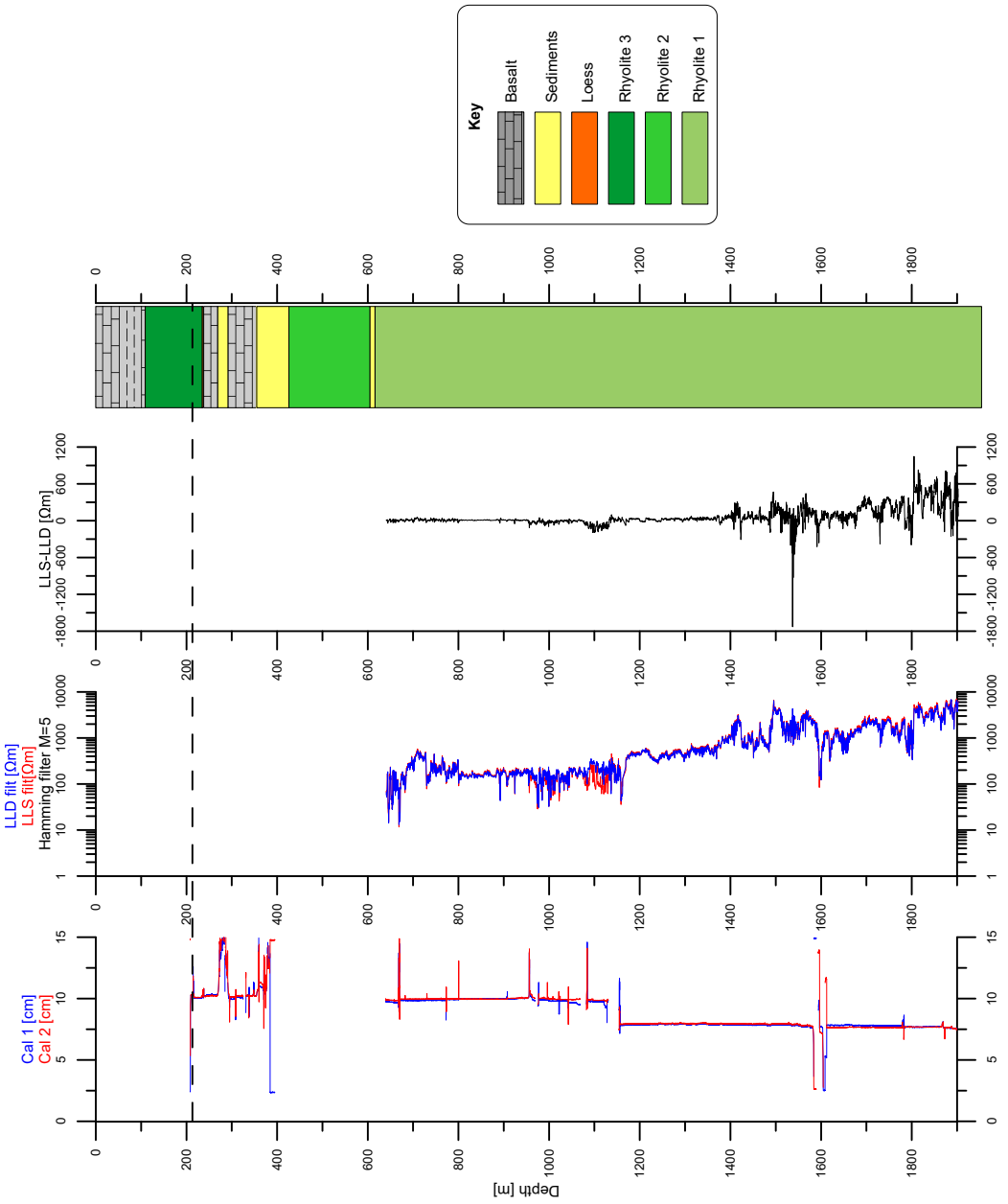

Fig. 3.17: Shallow and deep resistivity logs of the Kimberly well. Resistivity logs were filtered with a 5-point Hamming window and analysed for resistivity change between the two invasion depth measurements.

3.2.3 Acoustic Logging

The acoustic data was provided by the OSG support group in its processed form with compressional and shear wave velocities interpreted using three different processing methods. First arrival picking was done by processes offered in Geobase and WellCAD^{TM}, as well as by semblance analysis in WellCAD^{TM}. Therefore, reproducing the processing steps was difficult but all three results conclude to similar velocities at each depth position.

Within this thesis first arrival picking was performed again with the Seismic Data Processing software package VISTA^{TM}. Picking was often complicated at zones with decreasing and scattered transit times and lower amplitudes, which therefore sometimes needed to be erased to avoid misinterpretation. An extract of processing raw traces of near- and far-offset receivers and their associated interpretation is illustrated in Figure 3.18. Taking into account that arrival time (μs) increases with transmitter-receiver spacing, compressional, shear, and Stoneley waveforms were identified, presented on tracks 1 and 2 in Figure 3.18. In applying a cross-correlation, coherency technique ‚Semblance' the slowness ($\mu s/m$) from those two receiver traces was determined. The bands where the most similarities to an acoustic arrival time exist, are marked in a dark colour. Evaluating those dark bands on track 3, the coherent wave types are allocated towards compressional-, shear- and Stoneley wave.

Referring to the thick rhyolite 1 unit sampled between 625 and 1893, average P- and S-wave velocities are 4615 m/s and 2609 m/s, respectively. The average V_p/V_s ratio of 1.71 also proves the adequate quality of first arrival picking in this section. As FWS logs were only available between 197-285 m and 625-1893 m, velocity information for rhyolite 2 and partly basalt, sediment, and rhyolite 3 are lost. This was of bad hold conditions. An extensive analysis of seismic velocities for the Kimberly well will be therefore carried out in Chapter 4 including sonic velocities derived from zero-offset VSP.

Compressional and shear wave velocities for the 30 m basalt flow at 238 m are highly scattered. It can thus be concluded that some embeddings in form of fractured alteration zones modify the rock composition and therefore the velocity. Although velocity values are quite consistent for rhyolite 1, showing a slight increase of velocity with depth, at sections where borehole televiewer images exhibit broader fractured zones, velocity also substantially decreases. Major decreases and rapid changes in velocity are observed in zones at 665-671 m, 727-732 m, 972-977 m, 1076-1086 m, 1128-1162 m and 1593-1601 m.

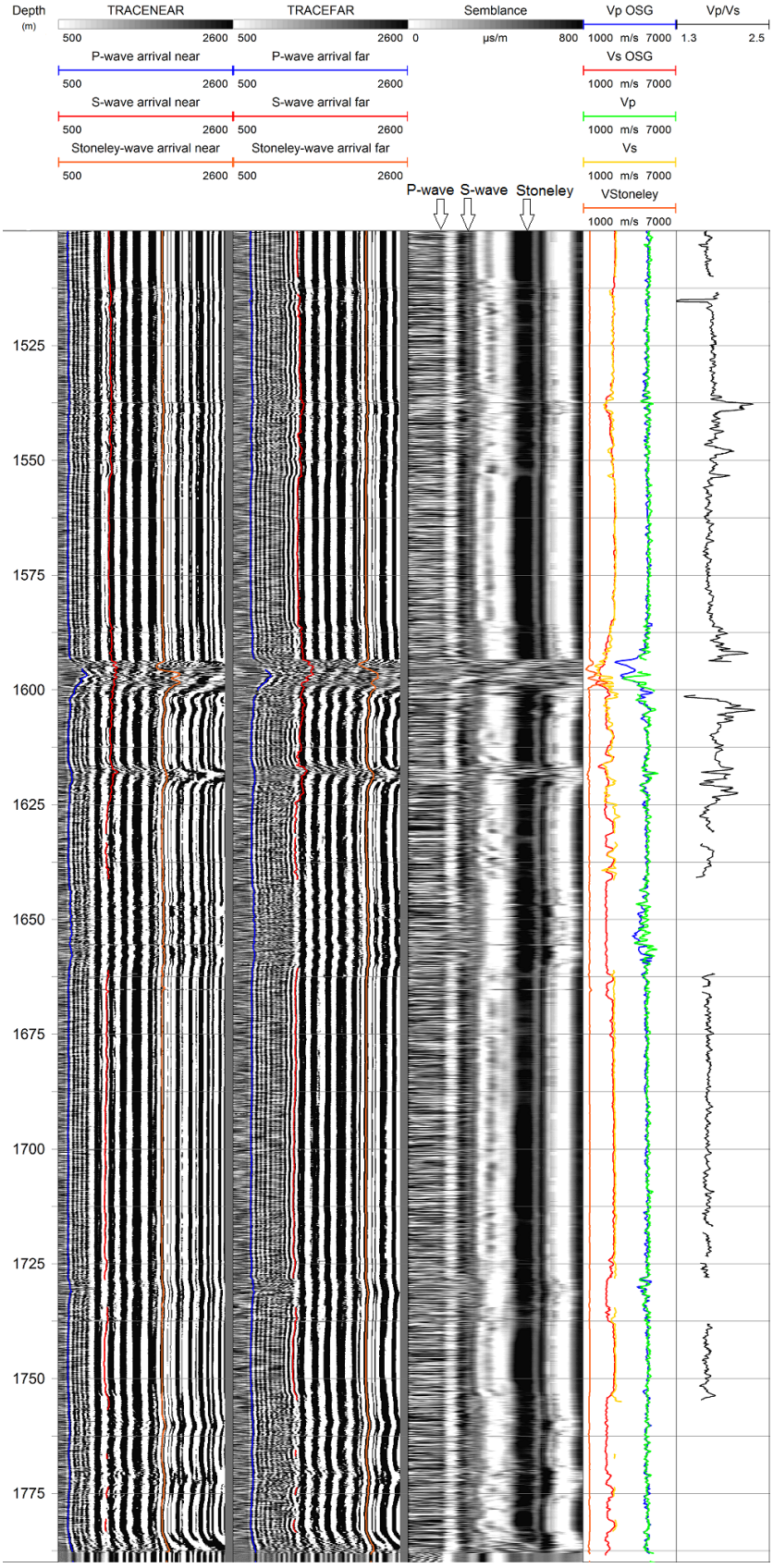

Fig. 3.18: Processed and interpreted FWS data between 1500 and 1800 m drilling depth for the Kimberly well. In particular a major fracture zone between 1593-1601 m is emphasized by strong decreases in compressional and shear wave velocity as well as changes in Stoneley wave velocity.

3.2.4 Radiogenic Heat Production

The main part of the Earth's surface heat production derives from the radioactive decay of the isotopes uranium, thorium, and potassium in the mantle and crust. According to Pollack & Chapman (1977) about 40% of the surface heat flow has its origin in the radiogenic heat production of the upper crust, so that the examination of this feature for the Kimberly well will provide another aspect for geothermal evaluation.

By using equation 3.3 for total gamma ray values between 616-1900 m, associated with the massive rhyolite tuff, the radiogenic head production yields a mean value of 3.33 $\mu W/m^3$. The more adapted approach by calculating the radiogenic heat production in terms of density and spectral gamma ray measurements [equation 3.4] resulted in a comparable rate of 3.03 $\mu W/m^3$.

As no direct density logging in the Kimberly well nor on the retrieved core was acquired, two rhyolite core samples were used to calculate the rock density on a laboratory scale. For this, the cores were cut in two cylindrical samples and mass, height and diameter were determined. The resultant rock density for rhyolite 3 sample no. 1 (109-236 m) yields a value of 2418.6 kg/m^3, for the deeper rhyolite 1 sample no. 2 (616-1956 m) rock density is 2469 kg/m^3.
Since spectral gamma ray measurements were only available for 616-1163 m and the sampled density is assumed to be consistent for the deep rhyolite section, the radiogenic heat generation needs to be seen as a reference value.

If the density changes by a value of 100 kg/m^3, then the radiogenic heat production will decrease/increase by an amount of 3.84%. Furthermore, by including the standard deviation of U, Th and K, radiogenic heat production for rhyolite 3 may be subjected to a maximum change of 28%. This strong change herein lies in the statistical fluctuations of the radioactive decay processes. Consequently, both radiogenic heat productions were estimated sufficient enough within statistical errors.

Figure 3.19 depicts the natural and spectral GR log and their corresponding radiogenic heat profiles. For the lithologic units, respective density values were either taken from the two core samples or from literature values given in Schön (1983).

Unfortunately, there are no published radiogenic heat production data for the Snake River Plain available; therefore it is not possible to draw any conclusion about the classification of these data. But the results lie in the range, where the continental heat production of igneous and metamorphic rocks with 2.5-3.5 $\mu W/m^3$ is assumed (Pasquale, Chiozzi, & Verdoya, 2014).

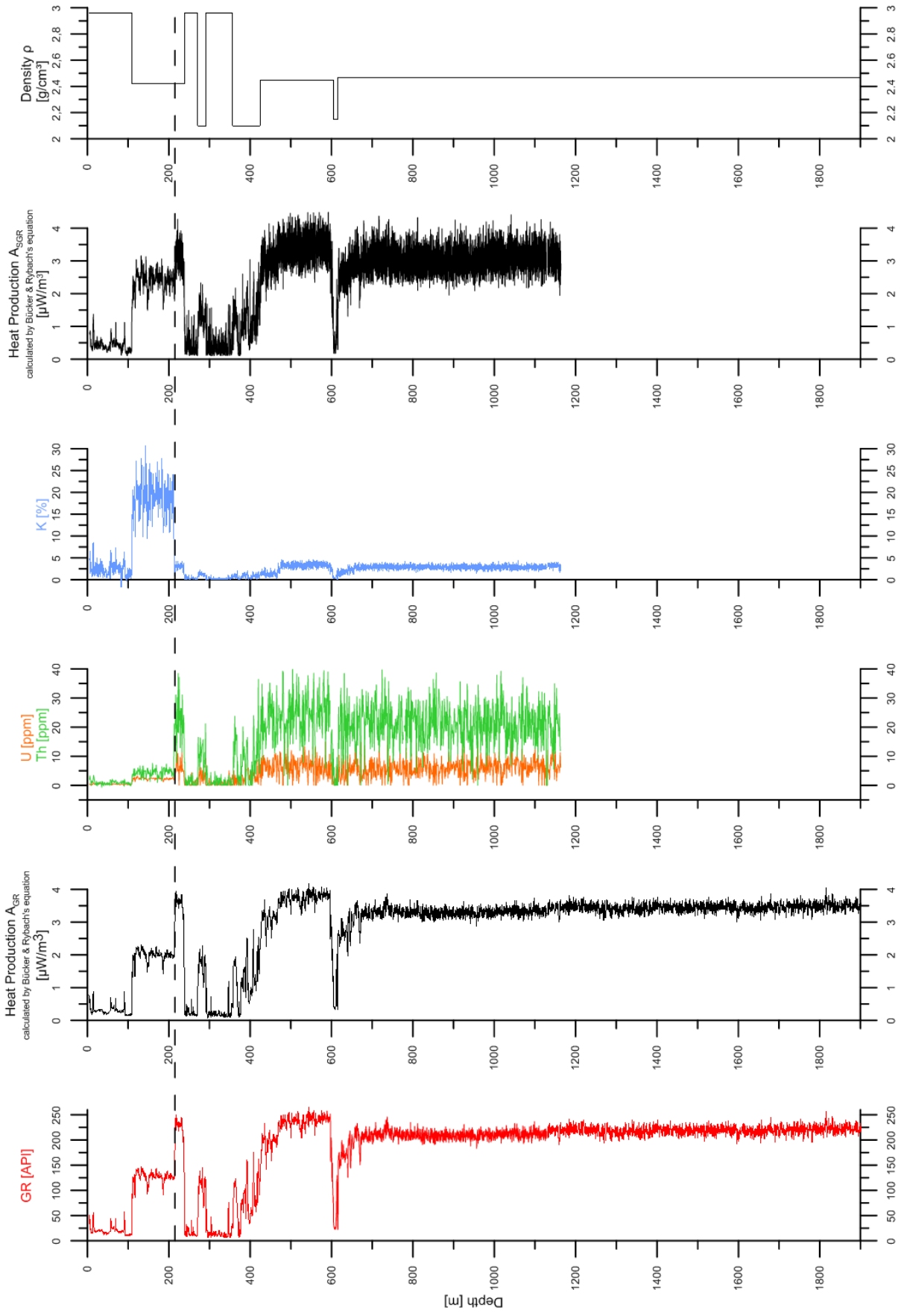

Fig. 3.19: Radiogenic heat production logs derived from total and spectral gamma logs, and density assumptions using Bücker and Rybach (1996) equations

3.2.5 Thermal Logging

The temperature values measured by the MS sonde were used to calculate the thermal gradient of the Kimberly well, showing an average thermal gradient for the entire logging depth of 15.1°C/km. The location of the well, in direct vicinity to the margin but still situated right above the Snake River aquifer, leads to a suppression of temperature (Shervais et al., 2011). This fact is shown in Figure 3.20 by a negative geothermal gradient in the upper 146 m of the well bore. Another argument for this immense negative geothermal gradient is the vesicular basalt above the water table, which exhales air during the day and inhales it at night. This theory was first pointed out by Brott, Blackwell & Mitchell (1976) , who noticed similar disturbances of the geothermal gradient in the upper hundred meters in other wells throughout the Snake River Plain penetrating basalt.

The geothermal gradient is not consistent for the entire well, instead it varies in several sections. Between 146 and 491 m the temperature increases from its minimum temperature of 18.4°C to 47.98°C again. Such a rising in temperature after passing the aquifer is also reflected in several wells throughout the Snake River Plain (Shervais et al., 2011). The spike at 491 m and the subsequent cooling cannot be assessed at this stage, since other geophysical logs do not indicate any anomaly at this section. With a relatively constant rising of temperature for the section between 549 and 1900 m, resulting in an ultimate temperature of 57.29°C, a thermal gradient of 9.2°C/km was calculated.

All in all, the temperature of 57.29°C at the total logging depth is still too low for geothermal power generation. But considering the calculated geothermal gradient of 15.1°C/km, a temperature of $\approx$ 85°C may be reached right before an exploration depth of about 4 km. This temperature is much closer for providing efficiency for the geothermal power plants.

As expected, the mud pressure of the MP-sonde does increase in a linear relationship constantly. However, the pressure gradient changes at three depth locations, which also correspond with caliper enlargements at 1150, 1586 to 1612 m and 1782 m. The pressure drop may be an indicator for a natural fracture for the lowest two anomalies.

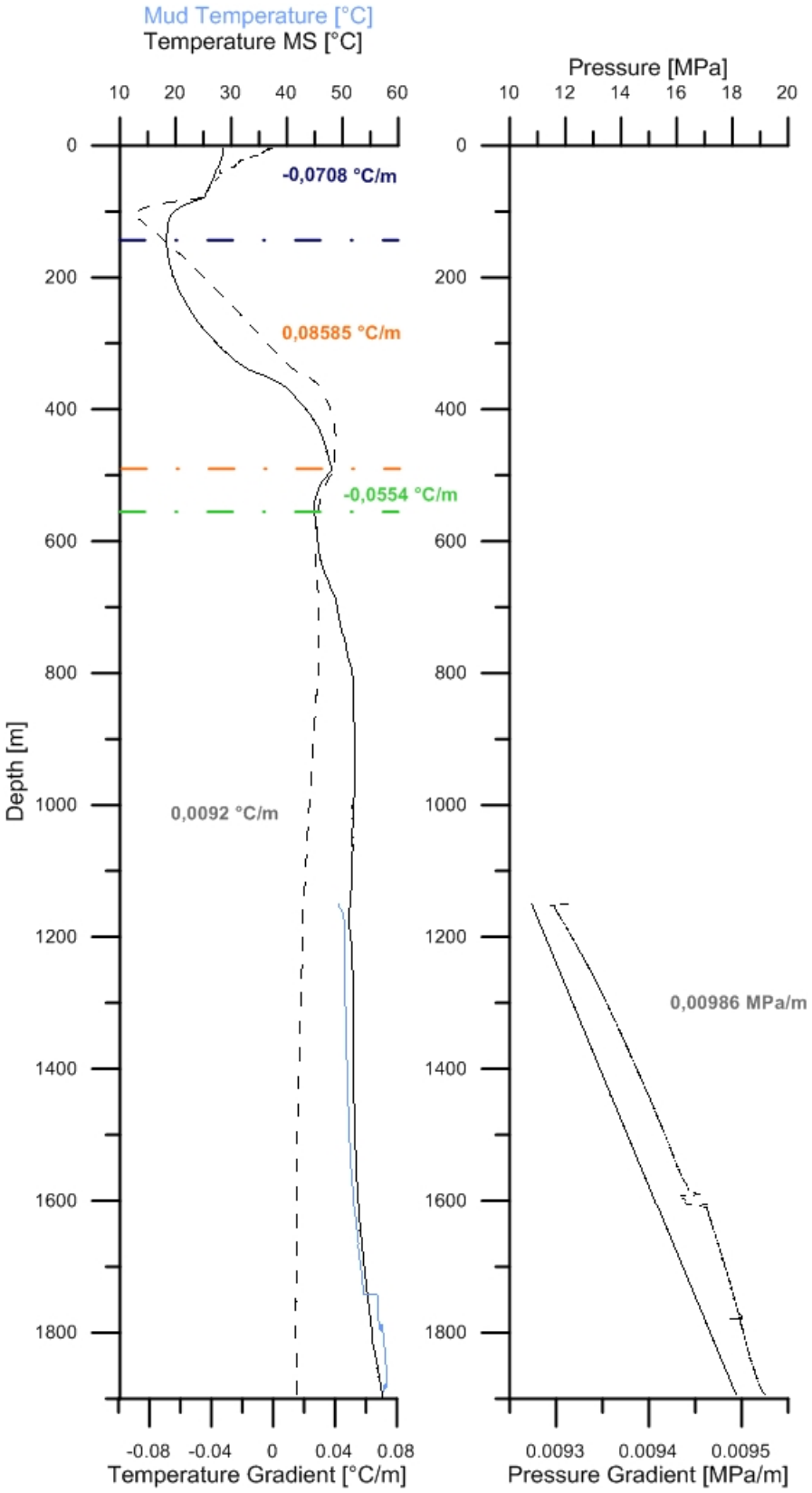

Fig. 3.20: Temperature and pressure profile at the Kimberly well. Dottet lines represent the temperature and pressure gradient profiles. For the sections with typical decreasing or increasing temperature behaviour, the average temperature gradient has been noted.

3.3 Summary

As part of the ICDP project HOTSPOT a broad suite of geophysical logs have been acquired at the Kimberly well. The interpretations on in-situ physical properties of the subsurface rocks represents a comprehensive study between the geophysical logs, core scans and the limited number of core boxes available at the University of Alberta.
The three main rock types of the Kimberly well are differentiated on the basis of their distinct geophysical response into basalt, sediment and rhyolite, the latter can be stratigraphically divided further into three geological units. The basalt sections are characterized by their low total gamma ray values and uranium and thorium concentrations. Especially the basalt layer in the topmost hundred meters reveals a temperature decrease in this zone, the presence of the Snake River Aquifer. The neutron measurement implies a decrease in saturation with depth for this rock formation. The youngest rhyolite unit, rhyolite 3, is typified by the highest occurring potassium concentrations and an increase in total gamma ray. Between the eruptive phases of the Twin Fall volcanism, fluvial and lacustrine sedimentary layers are intercalated with volcanic rocks. Their occurrence is not only supported by core photographs, but also, in particular, by high uranium, thorium concentrations and total gamma ray values. The rhyolite units 2 & 3, show constantly high total gamma ray values, whereas autobrecciation and hydrothermally altered areas at the begin and end of the flow units lead to a decrease of natural gamma radiation.

Zones with open fractures are defined by waveform attenuation in the FWS log and an increase in resistivity. For the Kimberly well, where coverage of both physical properties is provided, the following zones can be declared as fractures: 665-672 m, 972-977 m, 1158-1160, 1590-1602 m, 1782-1805 m. The latter three open fracture zones show in addition a decrease in mud pressure gradient and widening in the caliper that could result from an permeable open fracture. It needs to be noted that the mentioned fracture zones outline the area of brittle zones in which physical parameter changes are observed. The actual fractures are much more in small-scale dimensions. The orientation of natural fractures reveals a E-W respectively ENE-WSW strike regime. In a depth section of 211 to 388 m natural fractures are oriented with a mean strike azimuth of 185°. The FAC 40 imaged a part of the rhyolite 1 unit from 635 to 1160 m depth. In this section rheomorphic folding of the layered texture is represented through a varying degree of dip and a mean strike azimuth of 167°. In contrasts, sediments showed more weakly dipping features. Geologic events like strong volcanic activity with the collapse of the caldera induced changes in the stress regime of the Twin Falls volcanic province. That is the main reason to find orientation difference.

By probing a sample of the rhyolite 1 and 3 for density, we obtain an understanding of the radiogenic heat production around the Kimberly well. Based on the sampled density values, radiogenic heat production has been estimated to be around 3.03 $\mu W/m^3$, representing next to the geothermal heat production a sufficient enough high heat estimation just from radiogenic elements.

It emerged that televiewer logs can provide a clear image of fractures and validate fractures further on the basis of geophysical logs. But only with a precise analysis of the drilled cores we ultimately can close the cap between the geophysical log response and the mineralogical composition of the subsurface rocks.
The acoustic log especially helps in analysing the seismic properties of the processed vertical seismic profile.

Chapter 4
Zero-Offset Vertical Seismic Profile

In addition to the geophysical logging, which was discussed in the previous chapter, a vertical seismic profile (VSP) has been used to deduct a further detailed picture of the complex geology in this region. The completion of such a VSP survey shall help to gain an enhanced image of the subsurface near the borehole as well as identifying volcanic flow boundaries interbedded with sedimentary layers and how they correlate with previous known geological records. The interpretation is based on the response of upgoing and downgoing events since geophones are placed down the borehole beneath the Earth's surface.
The processing algorithm for VSP data comprises the important step of wavefield separation and the allocation of primary upgoing events for interpretation. In this chapter I describe a zero-offset VSP that consists of closely spaced measurements with a geophone string downhole. Hence, this chapter will concentrate on this kind of application and provide in the first section an overview of the measurement including the fundamentals of VSP, source-receiver geometry and its advantages. In the subsequent sections the data acquisition and the processing sequence up to the creation of a corridor stack will be presented in more detail.

4.1 Overview

The main concept of vertical seismic profiling is the placement of a seismic source at the surface to measure the seismic response with closely spaced geophones at various depths in the wellbore (Hardage, 1983).

The beginnings of vertical seismic profiling can be traced back to the 1950's in the Soviet Union, where geophysicists published the first comprehensive applications for seismic measurements in boreholes. But the foundation was not laid until 1974 with Gal'perin's book „Vertical Seismic Profiling and Its Exploration Potential". After this publication the awareness of the advantages of vertical seismic profiling was also raised in the Western World and grew from there on steadily (Hardage, 1983).

In comparison to surface seismics, where geophones are laterally positioned only on the surface, the geophones in a vertical seismic profile are positioned relative 90° to the Earth's surface as measured from the well head if the borehole is perfectly vertical (Hardage, 1983). Corresponding to the acquisition geometry and purposes of the survey, the surface source can be immediately adjacent or at a certain offset away from the well head. This leads to several borehole seismic acquisition geometries that include the zero-offset VSP with the source located near the rig, the far-offset VSP with one source located in a certain horizontal offset from the well location, the walk-away VSP with various source offsets in a line, and the 3D VSP with sources in a grid or spiral around the borehole. VSP surveys in deviated wells, where the sources are placed vertical above each receiver, have also been operated in the last few decades as well and are nowadays in the mining sector referred as "Downhole Seismic Imaging".

By means of the cross section in Figure 4.1 the convential VSP acquisition and principle shall be explained. The geophones are moved to a desired depth for which many single seismic shots are carried out. The requirement for VSP is the performance of at least one seismic shot for every geophone location. The traces recorded for each geophone level-source location

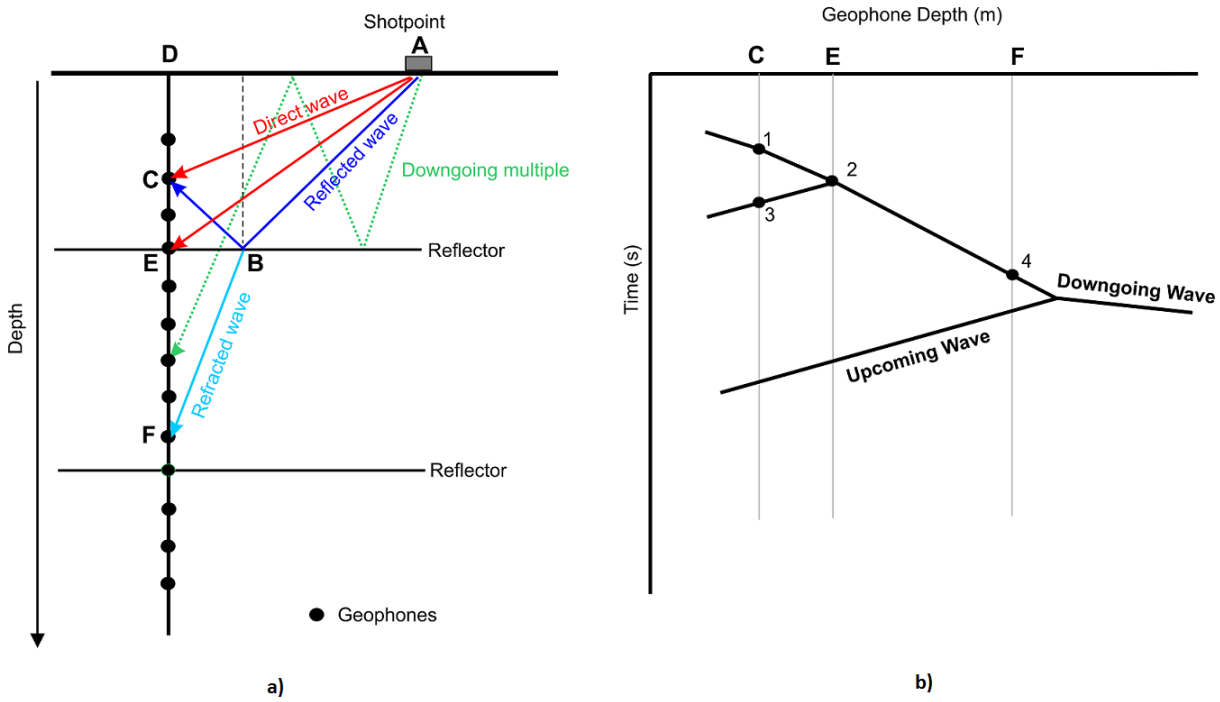

Fig. 4.1: Cross section of a VSP survey a) Ray paths and b) Associated traveltimes. Adapted from Yilmaz (2001).

combination are then edited and summed in order to reduce random noise. This procedure is repeated for every new depth location until a final z-t (depth-time) section is created (Figure 4.1 b)). Thereby each geophone location provides a trace on the VSP section. Figure 4.1 a) shows just a small simplified selection for the most common ray paths recorded during a VSP survey. The ray paths AC and AE are called direct waves or direct arrivals, whereas ABC is a reflection and ABF is a refraction. By transferring those ray paths into a z-t section shown in Figure 4.1 b), both direct arrivals and the refraction are assigned to the corresponding traces C, E and F. Because those events have only downgoing ray paths, they are therefore called downgoing waves. By contrast, segment BC shows a reversed direction, what leads to the conclusion, that this is an upgoing wave. Those two seismic events occur due to the fact that all geophones are lowered into the borehole. In this regard, surface seismic just records upgoing seismic events based on the horizontal acquisition geometry on the Earth surface for all receivers. Downgoing and upgoing waves coincide in point 2 on trace E since the direct wave and the reflection arrival of the interface crosscuts. This concludes that the geophone is positioned directly on an interface (Yilmaz, 2001).

Vertical seismic profiling shows similarities regarding the source and receiver geometry to check shot velocity surveys, however there are some major differences. The vertical spacing of geophones for velocity surveys extents over several hundred meters, whereas VSP data is recorded in geophone depth intervals of typically 10 to 25 m, although here a much closer spacing is employed. Moreover, to obtain a velocity survey just the first break times of the downhole signal are used, whereas for VSP the first breaks with the subsequently following up- and downgoing events are recorded (Beaumont & Foster, 1989). It must be taken into consideration that a VSP section represents events in one-way traveltime. When processing the events they are shifted to two-way traveltime and therefore temporally comparable with

surface seismic events.

In order to complete a successful VSP survey a few factors need to be taken into account. Necessarily a borehole with preferable vertical orientation must exist first. Experience showed that a rigidly cemented single casing leads to the smallest alteration of waveform character, which will be modified, when body waves propagate across the borehole formation interphase to the geophone. When circumstances make it possible, also an uncased, open borehole can be used for VSP measurements as long as the sondes can be well coupled to the borehole wall. The borehole diameter in this case can be determined by a caliper log, which helps to detect washouts. If the borehole diameter is too large, the so called ‚wave shadow side of the borehole' appears. Before VSP measurements begin the acquisition team needs to know if borehole obstructions exist.

When combining VSP with surface seismic to improve geological interpretation, the seismic source should be the same for both measurements. Because, as described before, for every lowered receiver in the borehole many shot wavelets at a certain fixed surface location must be generated, whose wavelet characteristics shall stay the same for the whole survey. This result can be achieved by using dynamite, impulsive surface sources or vibrators. Because seismic reflections are usually quite weak relative to the original incident wave, downgoing wavefields dominate a seismic section more than upgoing wavefields.
Receivers are from their construction more massive than normally used surface geophones, as well from their size as from their weight, to endure the high pressure of the deep drilled wells (Hardage, 1983). To obtain no spatial aliasing in the data, the single geophone stations should be less than half of the shortest wavelength of a seismic wavelet apart (Beaumont & Foster, 1989). However, due to larger survey areas and costs, industrial surveys cannot always afford these types of geophone spacings.
Higher-resolution subsurface images of VSP data can be created due to the reduced target-to-receiver path which leads to an improved lateral resolution. On the same subject the diameter of the Fresnel zone will be reduced, so that e.g. weakly reflecting interfaces can be determined better (Beaumont & Foster, 1989).

4.2 Data Acquisition

The zero-offset VSP at the Kimberly drill site was carried out on June 18th and 19th, 2011 by scientists of the University of Alberta and Boise State University. The seismic energy source IVI Minivib^{TM} (Industrial Vehicles International, Inc. in Tulsa, Oklahoma) was stationed with approximately 17 m offset from the borehole. This close positioning makes it possible, that ray paths travel almost parallel to the borehole and a vertical alignment of source-receiver can be assumed. For the survey the Sercel Slimwave® seismic receiver system, aquired by the GFZ-Potsdam and operated by the ICDP-OSG, was used to record the sweeps in 2 m depth intervals between 1870 m and 10 m upward. The borehole geophone chain comprises 4 geophone levels with 10 m spacing, whereupon every level consists of a 3-component 15 Hz borehole geophone. It was a deliberate decision to chose a more closely spaced receiver interval of 2 m, in contrast to normally logged VSP data with geophone depth intervals of 10 to 25 m, to enhance spatial resolution on seismic in-situ velocities (Schmitt et al., 2007). The generated seismic energy has a frequency bandwidth of 10-160 Hz, which travel in 14 s linear traper sweeps into the ground. Finally, we can plot the produced vertical profile as time versus depth section, as shown in Figure 4.1 b). To complete, all acquisition parameters are summarized below in Table 4.1.

Tab. 4.1: High-frequency VSP acquisition parameters for the Kimberly drill site.

Parameter	Zero-Offset VSP
Date of acquisition	18^{th} and 19^{th} June, 2011
Coordinates of well	42° 32.994'N, 114° 20.5749'W
Total drilled depth of well	1958 m
Source type	IVI Minivib^{TM}
Source elevation	1190 m
Sweep Frequencies	10 to 160 Hz linear
Peak Force per Unit	2720 kg
Offset distance	17 m
Receiver type	Sercel SlimWave® borehole geophone chain
Geophone spacing	10 m
Number of 3-C geophone sondes	4
Top measured depth (relative to KB)	10 m
Bottom measured depth (relative to KB)	1870 m
Sampling depth interval	2 m
Sweep length	14 s
Record length (correlated)	2 s
Sampling rate	0.5 ms

4.3 Data Processing

Processing of VSP data can not be broken down into a certain pattern with whom raw, unprocessed data are turned into an interpretive image of the subsurface around the borehole. It is more the case, due to various possibilities of source configurations and conditions of the well itself, that every processing step needs to be adjusted to the special drilling environment. The main challenge striking, when looking at a raw VSP section, is the dominant downgoing wavefield covering weaker reflections of the upgoing wavefield. Through different processing techniques, it is possible to undertake an analysis of those upgoing primary reflections, containing the main information about stratigraphic interfaces.
Initially, the data need to be prepared in the so called „Preprocessing stage". This step involves data quality check, geometry set up, trace editing, attenuation of both random and coherent noise, stacking as well as first arrivals picking with the resulting velocity analysis. The subsequent processing procedures consist of wavefield separation, deconvolution and generating a corridor stack (Figure 4.2). At the present time, the deconvolution has been left out.
The realization of all processing steps was made with the Seismic Data Processing software package VISTA^{TM}. If it is not indicated otherwise, all processing and analysis steps refer to the vertical component of the zero-offset VSP.

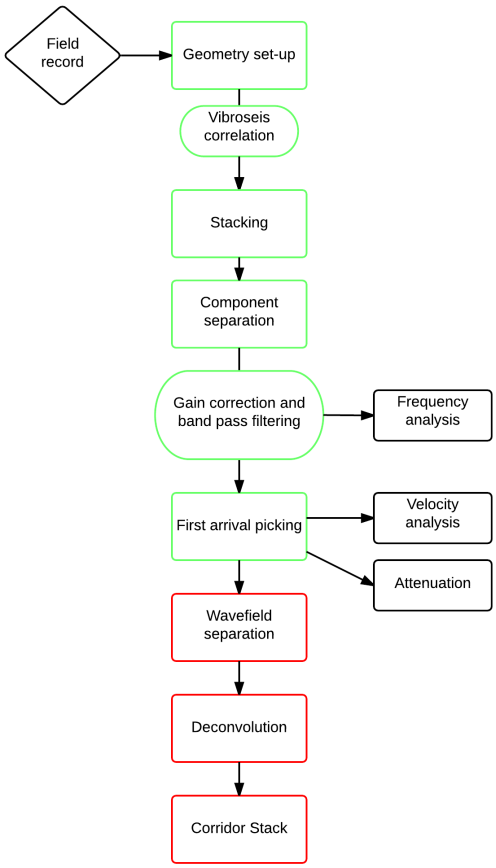

Fig. 4.2: Workflow for zero-offset VSP. Green squares symbolize preprocessing work flows and red squares characterize the processing sequences.

4.3.1 Preprocessing

Data Quality

The initial assessment of the data revealed good data quality in many areas implying that the geophones were rigidly bonded to the borehole wall. Should no appropriate geophone coupling be achieved, records become noisier as forces are not directed radial any more.
By analysing the frequency spectrum of the raw VSP data, before component separation and filtering have been applied, several prominent frequencies indicate surface cultural noise like mechanical and electrical noise. The peak frequencies of this harmonic noise can be assigned in the frequency-wavenumber (f-k) domain in Figure 4.3 as 180 Hz, 302 Hz, 423 Hz, 544 Hz. In order to avoid their influences, the data has been filtered with a frequency-wavenumber filter, after which only frequencies from 10-170 Hz are passed. This band width corresponds to the sweep frequencies of the seismic source, so that only the actual signal can be analysed. The raw zero-offset VSP data are contaminated also with a harmonic noise of 60 Hz, which is the power line frequency in North America. After separating in vertical and horizontal components, it happens that this particular frequency is not amplified any more, therefore a notch filter was not implemented.

In Figure 4.4, it is clearly evident that the strong amplitude downgoing wavefield overlies the weaker upgoing wavefield. Multiple upgoing wave modes can be recognized in the upper

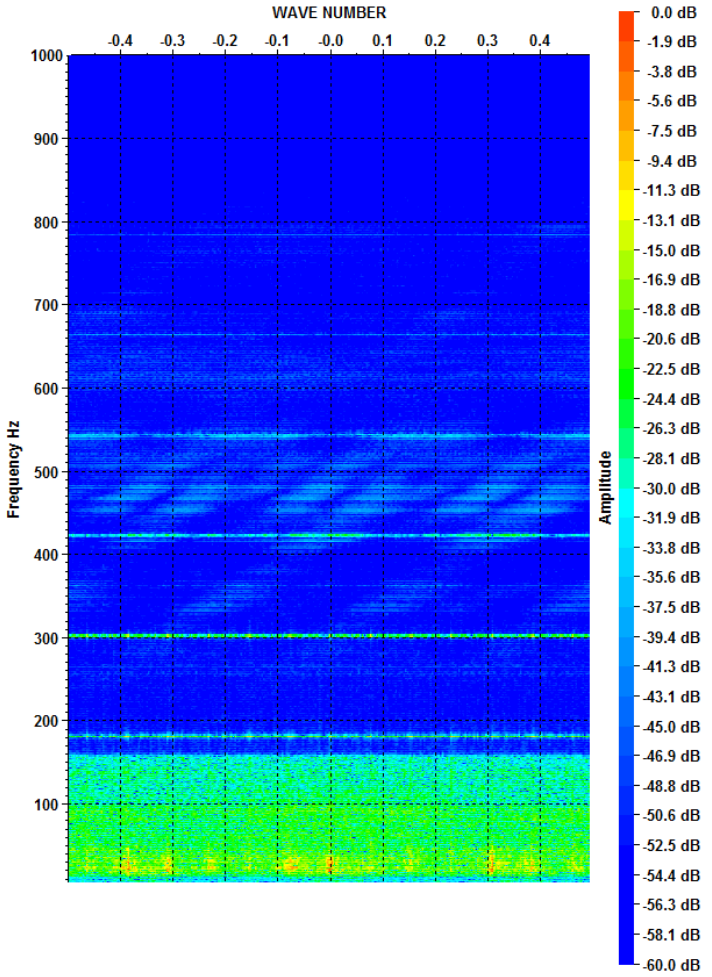

Fig. 4.3: Display of frequency-wavenumber of raw zero-offset VSP.

600 m of the borehole. In contrast to other VSP surveys, the display of the zero-offset VSP of Kimberly does not reveal clearly visible tube waves, so that the data set does not need to be analysed and removed by this type of low-velocity, high-amplitude events. Also S-wave can not be detected in the section. Through first arrival picking along the downgoing wave, we can compute a velocity profile for the borehole. But noisy traces in the upper 150 m and in a section between 1600 m to 1800 m made it difficult to determine accurate first arrival picking. At about 400 m depth the first arrival curve offsets suddenly by a primary reflection; this disturbs the first arrival times. The vertical component of the zero-offset VSP reflects the strongest amplitudes of the first arrival. However, in VSP the seismic wavelet is influenced by amplitude decay with increasing depth caused by spherical divergence, transmission losses, scattering, absorption and source-receiver directivity (Hardage, 1983). This context is displayed in the amplitude spectrum of various depth levels of the vertical VSP component in Figure 4.5. The vibroseis generated a broad high-frequency range, whose amplitudes decrease with increasing receiver depth. Thereby the amplitude decay behaves exponentially, meaning amplitudes attenuate in the upper hundred meters more than after a certain penetration depth (Figure 4.6). A first approximation for those reduced wavelet amplitudes is the application of an automatic gain function, which also helps to identify the direct arrival.

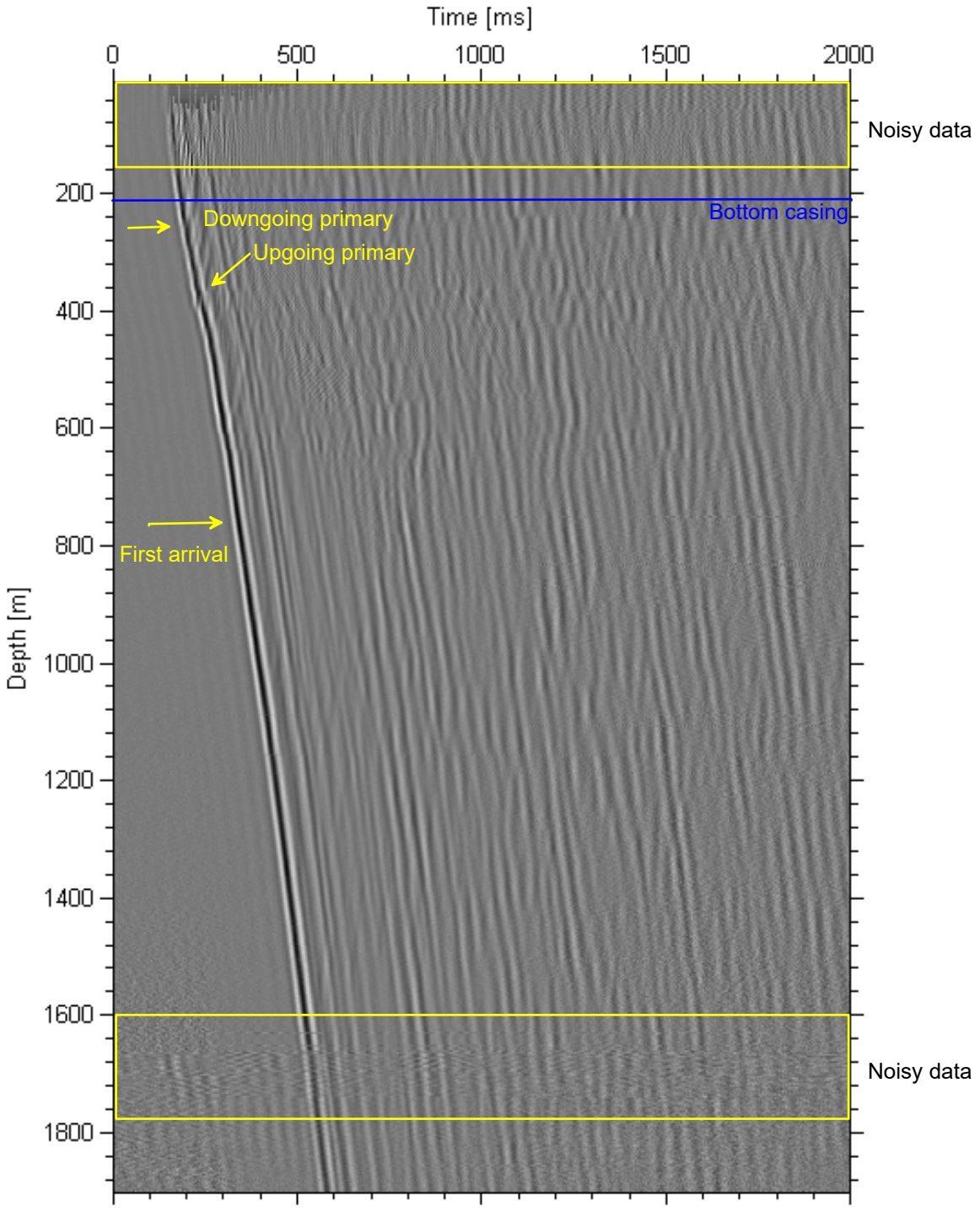

Fig. 4.4: Zero-offset vertical seismic profile after stacking traces at common depth and applying an automatic gain function.

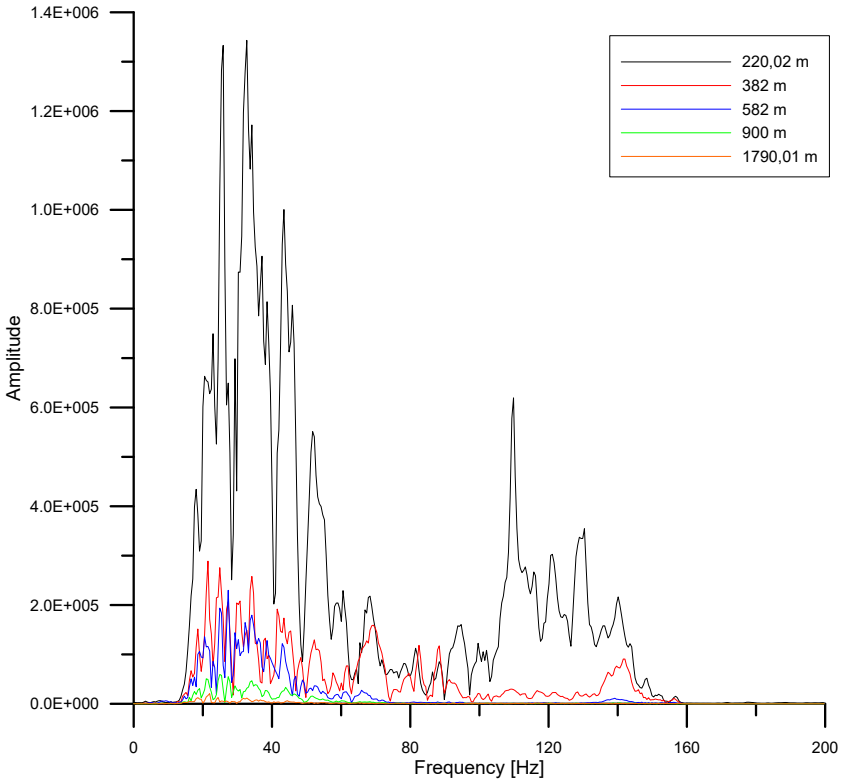

Fig. 4.5: Frequency spectrum at various depth of the vertical component of VSP data set. The data set was filtered with an f-k filter first.

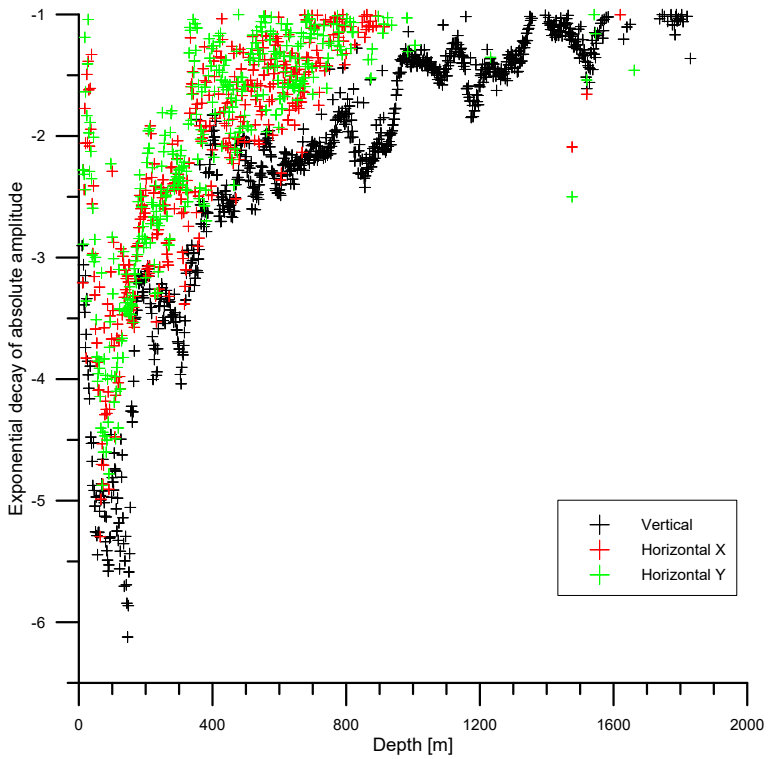

Fig. 4.6: Exponential amplitude decay for vertical (black), horizontal X (red), horizontal Y (green) component with depth. Figure displays raw data, where no filter has been applied.

Geometry Set-Up

In order to link the shot records with the coordinate information the ‚Geometry Window Display' in VISTA^{TM} was used. This ensures that every seismic trace is characterized through its own header information. For the Kimberly borehole the KB-elevation, the surface and shot datum as well as the source and borehole coordinates needed to be assigned.

Trace Editing, Stacking, Component separation

During the survey, many disturbances can cause noisy traces, which sometimes only can be eliminated afterwards. Therefore, it is very important to examine visually every recording regarding field notes and traces with anomalous amplitudes, which show unsuitable recordings. For the zero-offset, trace editing orientated mainly on field notes taken during the measurement. Observations like traffic noise and poor geophone coupling due to closed arms was modified again and muted from the data set. A successful outcome may obtained only when the processor has a comprehensive insight in the field work. Since this process relies partly on subjective assessments, a repeated inspection may be necessary several times. The task of trace editing is the improvement of the signal-to-noise ratio resulting in an enhanced image of the reflections. In addition, for obtaining a better signal-to-noise ratio, stacking has been applied. For every receiver level, four surface source sweeps have been fired, which shall be combined now for the receiver depth accordingly. First, the three-component (3-C) VSP data is separated in its X,Y and Z component and subsequent all traces at constant recording depth for the zero-offset VSP are stacked. This processing flow is monitored in Appendix B. Vibroseis correlation has been left out because the provided SEG-Y files were already correlated. However, the flow was used to image the input sweep.

First Break Picking

After successful editing and stacking, first arrival picking has been conducted. In order to achieve accurate first break times, manual picking on the vertical component is the best method to omit noisy traces. In preparation for it, an automatic gain function and band pass filter have been applied. Ormsby band pass filter (20-25-45-50) was used to enhance the first arrival with prominent frequencies of 30-40 Hz. Increased amplitudes correspond to this frequency range which was determined by analysing Figure 4.5. Search-mode option zero-crossing has been chosen, because wavelets are presented in zero-phase after correlation. Despite those filtering procedures, noisy traces in the shallowest 42 m and in a depth section between 1600-1800 m could not been eased. If traces in this areas show major deviations to actual possible first break times, they are excluded in first break picking. Despite the previously named depth sections first breaks could be picked clearly. The picked first break times of the vertical zero-offset component are illustrated in Figure 4.7.

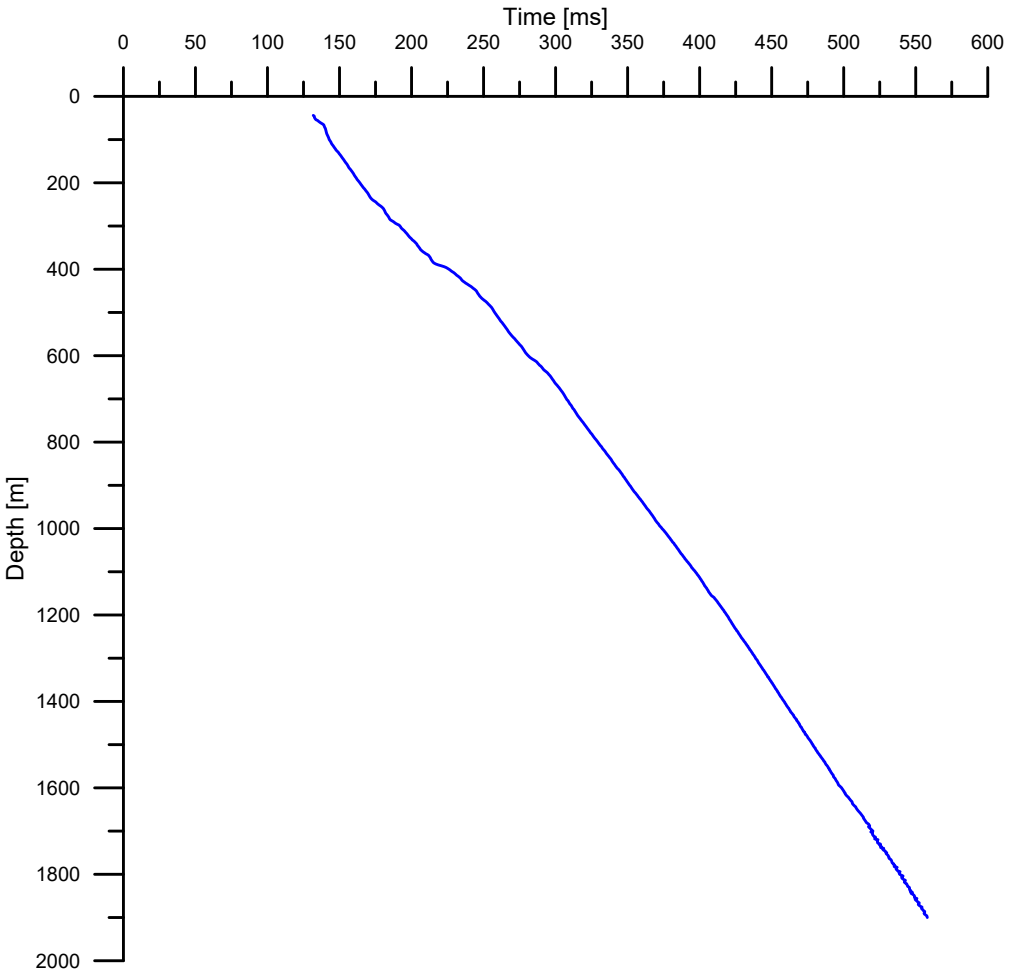

Fig. 4.7: First breaks picks of zero-offset VSP data displayed as time-depth curve.

4.3.2 Wavefield Separation

Wavefield separation is one of the most important steps in processing VSP data because only in this way we can isolate the weaker in amplitude upgoing wave modes from the prominent downgoing wavefield. As in surface seismics the reflected seismic energy is recorded, respectively, in VSP the upgoing events represent reflections at interfaces. Over the last three decades numerical techniques have been developed to separate VSP wave modes that include:

- Frequency-wavenumber filtering, e.g. (Hardage, 1983; Hinds, 1996)
- τ-p filtering, e.g. Moon et al., 1986; Hinds, 1996) = Radon
- Median filtering, e.g. (Hardage, 1983; Stewart, 1985)
- K-L filtering, e.g. (Hinds, 1996)

Within this work, median filtering was employed on the Kimberly data set showing optimal separation. The choice for a certain filtering method derives with the problems encountered in the dataset, thus problems like tube waves, random noise or SV contamination need to be treated with different filtering methods (Hinds, 1996).

Median filtering is a method used to smooth data by taking the middle value of an ascending-sequence of data samples and shifting this filter in a designed window over the input data (Hardage, 1983; Stewart, 1985). Mathematical the median represents the value of the (N+1)/2 position after rearranging all data samples in an ascending order and characterizes in this regard the value, which corresponds with the minimal distance from all other data samples in terms of the L1 norm. Median filtering is based on a non-linear process meaning that the filter output is not directly proportional to the input data vector. The smoothing property helps to remove noise spikes and let step functions (e.g. waves modes indicating abrupt discontinuities) pass while preserving the input signal. The function as despiker is obvious since the ascending order of data values, will always place the spike at the end of the sequence. The implementation of step functions is reflected in VSP data as upgoing reflections, since impedance interfaces operate as boundaries below which no reflections occur. The advantage of this method is maintaining the sample position in space and time by amplifying the upgoing events (Hardage, 1983).

Wavefield separation by median filtering comprises the subtraction of the downgoing wavefield from the original field recorded and is summarized in theory in Figure 4.8. The procedure is reproduced in the same order for the zero-offset VSP of the Kimberly borehole in Figure 4.9. First the process ‚Flatten' is used, which shifts all traces to a negative arbitrary time datum and aligns the downgoing modes vertically regarding their firstbreak picks. In the case of the Kimberly data set, downgoing events are flattened to 200 ms (Figure 4.9b)). The amplitudes of the vertical first arrival are equalized for the main peak by applying the constant value of the maximum amplitude. The advantage of scaling is that the initial waveforms are as uniform as possible. An RMS scaling over the entire downgoing pulse led to slight alterations of the wavefields, therefore the maximum amplitude was chosen as superior method. Scaling is a precondition before applying the median filter that slides in a designed window along the depth axis for every time point. As the size of the filter, a 29-point median filter was chosen to attenuate upgoing events and helps capturing smoothed and amplified downgoing events. The length of the median filter plays an essential role in matters of the effectness for rejecting upgoing modes. In the search for an adequate filter length, the 29-point median filter could enhance substantially more downgoing modes, especially within deeper receiver

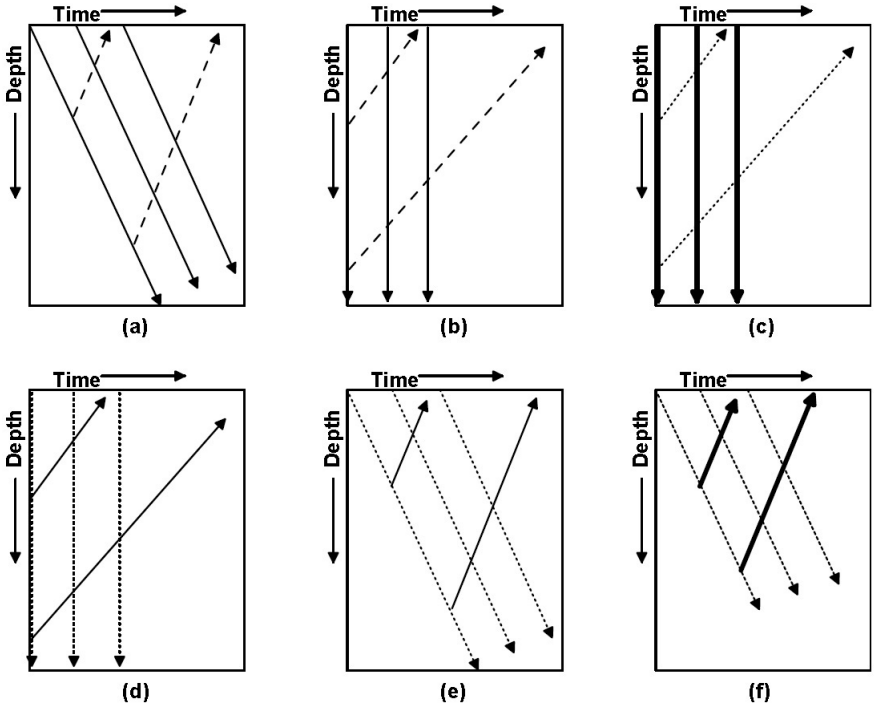

Fig. 4.8: Median filtering scheme to separate downgoing and upgoing wave. a) Raw VSP data displayed in depth-time format. b)Vertical alignment of downgoing events c) Apply median filter to enhance and smooth downgoing events. d) Arithmetic subtraction of data set D from data set A to attenuate downgoing events. e) Data is shifted back to original times. f) Applying another median filter to emphasize upgoing events. Adapted from Hardage (1983).

depth levels, than a 19-point median filter. In general, the smoothing effect will increase by selecting more traces according to the filter length but attenuation with a shorter filter length was too strong in the case of the Kimberly data set. By subtracting the generated median filtered downgoing wavefield from the original flattened wavefield, the upgoing wavefield is as the difference produced. The flattening process will be reversed by firstbreak shifting back. This leads to the upgoing wavefield in field recorded time and can be extended to a display of two-way traveltime by deflattening twice. Finally, a further 9-point median filter helps to enhance upgoing events.

When applying a median filter the effect of the window length and the first break times on the data set need to be considered. Generally, smoothing of the data increases with an increase in the number of traces over which the median filter is applied. Nevertheless, the median filter should still be long enough to cover the desired waveform which is to be rejected. Furthermore, the accurate picking of first break times is important to vertically align the phases properly. Otherwise static time shifts will lead to incoherency in the downgoing events (Hardage, 1983).

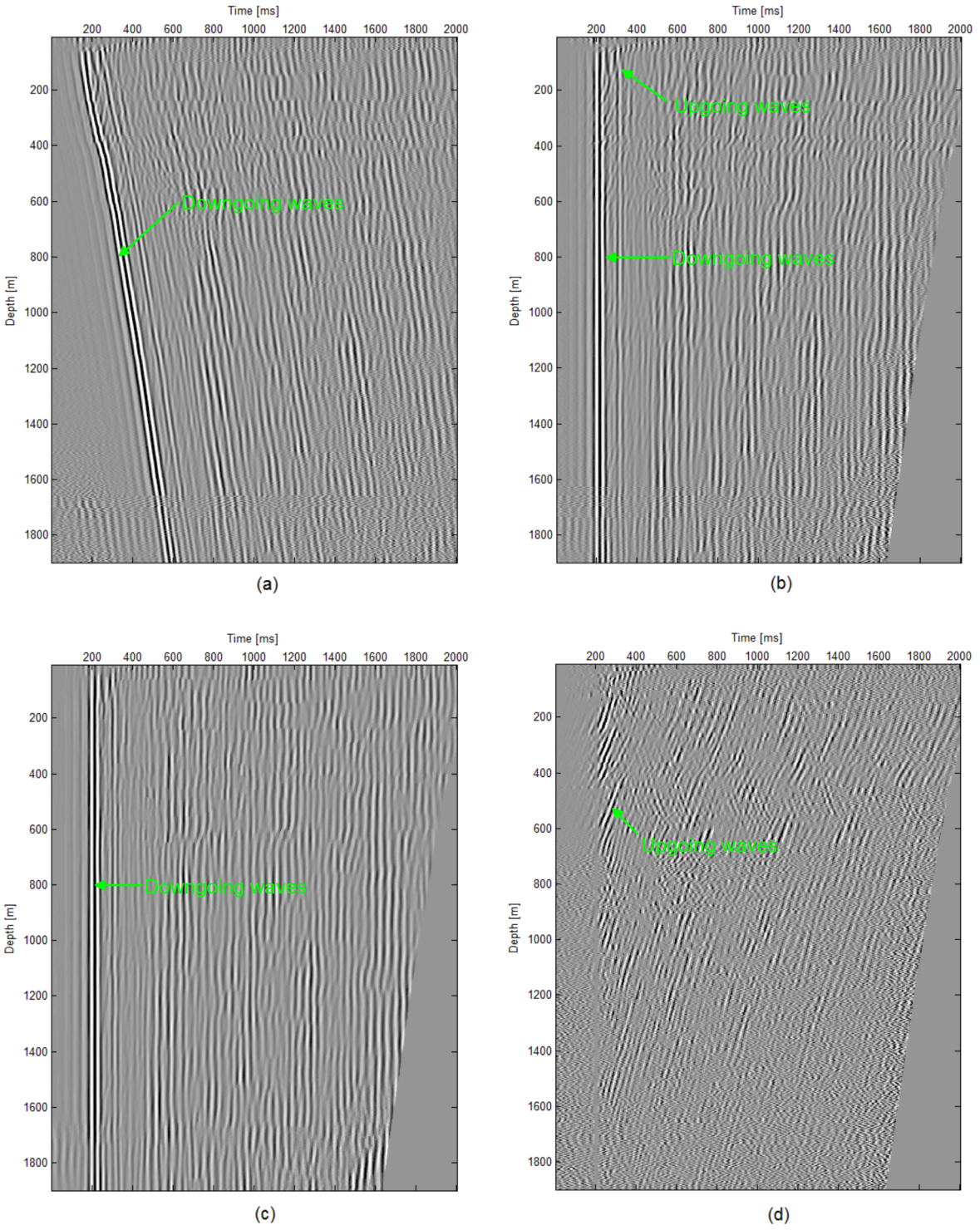

Fig. 4.9: Wavefield separation for zero-offset VSP data collected at the Kimberly well using the vertical component. (a)Vertical component after filtering. (b) Scaled downgoing waves are flattened at 200 ms and enhanced with a 29-point median filter in (c). Through subtraction upgoing waves are gained in (d).

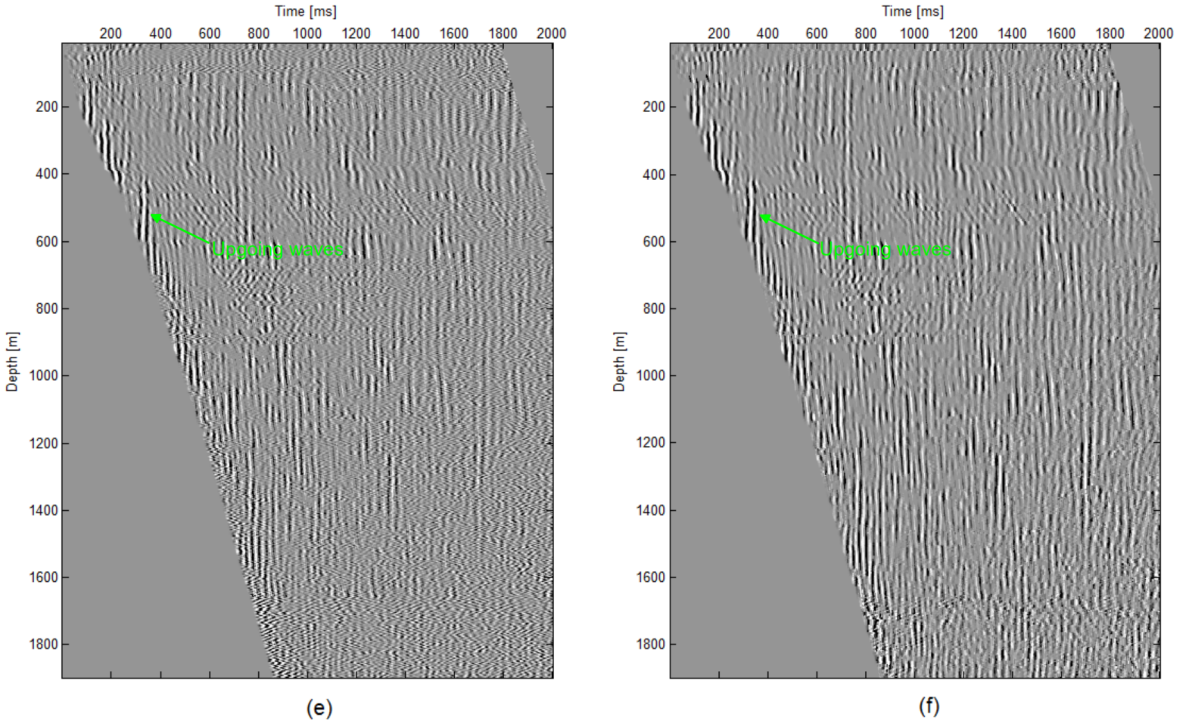

Fig. 4.10: Wavefield separation for zero-offset VSP data collected at the Kimberly well using the vertical component. (e) Upgoing waves are shifted back to their original time and are displayed in two-way travel time. (f) A further 5-point median filter emphasizes the upgoing events.

4.3.3 Corridor Stack

A corridor stack is a vertical summation procedure, where the traces in an upgoing vertical seismic profile are summed over a specified data window, known as corridor, along their first-break times. This yields a single trace of the primary reflection events in two-way travel time and is called outside corridor (Sheriff, 2002). Through time delays between primary reflection events and their associated upgoing multiples, the outside corridor is predominately free of upgoing multiples. Whereas the remaining stacked portion produces an inside corridor where both multiples and primary events are retained. The basic principle behind the use of the outside and inside corridor stack is presented in Figure 4.11.

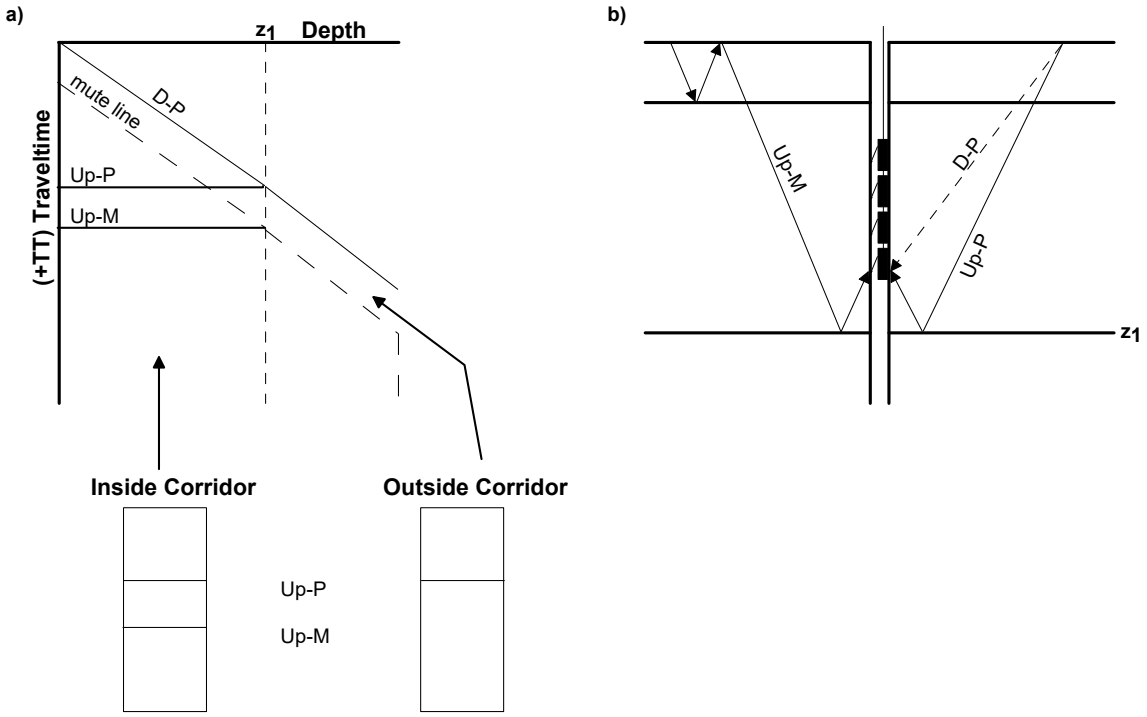

Fig. 4.11: Schematic creation of the inside and outside corridor stack. a) Flattened upgoing wave events are shown in a depth-traveltime plot in +TT time. For the outside corridor stack a window is selected along the downgoing primary (D-P). Upgoing primary (Up-P) intersects the first-break curve, whereas the upgoing multiple (Up-M) does not intersect the first-break curve as it is recorded later in time. b) Illustration of ray paths for both primary and multiple events. Adapted from Hinds, Anderson & Kuzmiski (1996).

The top of a generating interface is represented by the downgoing waves in -TT time, the bottom generating interface is revealed by upgoing waves in +TT time. The interbed multiple is recorded later time than the primary event as it travels between those interfaces (Hinds, 1996). However, corridor stacking is based on the assumption that the interfaces are horizontal and flat.

The processing flow used to create an outside, inside and full corridor stack is provided in Appendix B. Figure 4.12 shows the 25 ms corridor from the first break time that is used to generate the outside corridor stack. For the deepest 10 traces no window was applied. The size of window on which the outside corridor is isolated plays an important role due to the entrapment of multiples. If the window is too large multiples may be included in the outside corridor. But if the size of the applied window is too small, distortions on the primary events are also reflected in the stack.

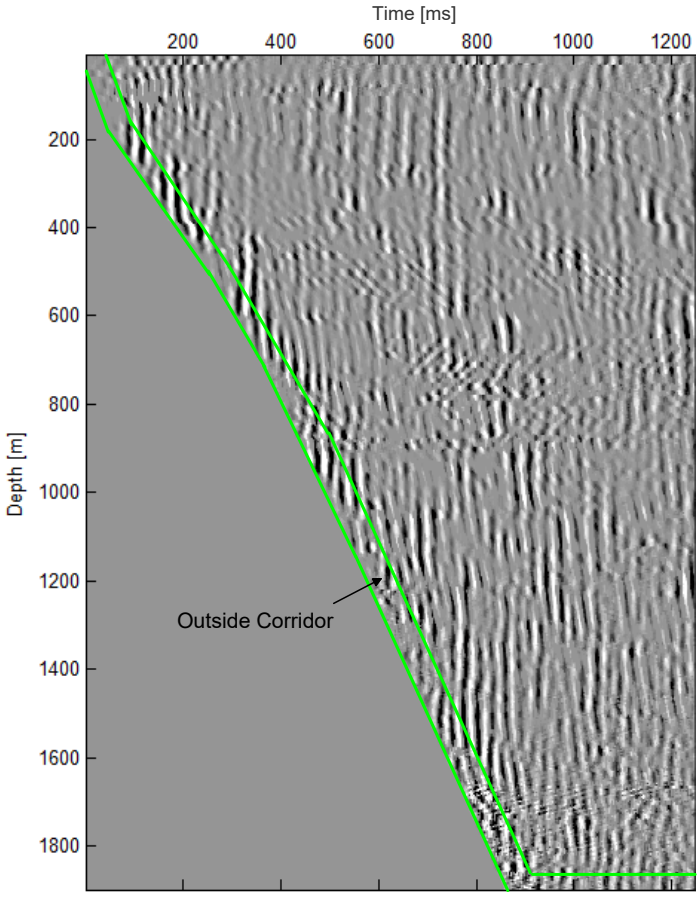

Fig. 4.12: Zoomed upgoing wavefield in +TT time with a 25 ms outside corridor zone. Below this zone the data is muted.

For this reason, two window sizes are chosen to compare the resulting stacks on those effects in Figure 4.13. All three panels for every window are the same over the depth of interest. For display purpose the corridor traces are plotted repeatedly 10 times. The 25 ms window depicts the primary reflections of the uppermost subsurface rock interfaces more accurate than the larger window of 100 ms due to their size. Primary events appear on all three panels at around 100 ms, 180 ms, 220 m, 340 ms and 550 ms. As multiples do not intersect the first break time curve and are therefore not represented in the outside corridor stack, one multiple at 720 ms is identified. As the first break time curve ends at 850 ms, no further information can be gained.

The conduction of a corridor stack can help to improve structural and lithologic interpretation of surface seismic data based on the representation of zero offset and surface seismic data in two-way traveltime. This tie may also help to identify and finally remove multiples in surface seismic.

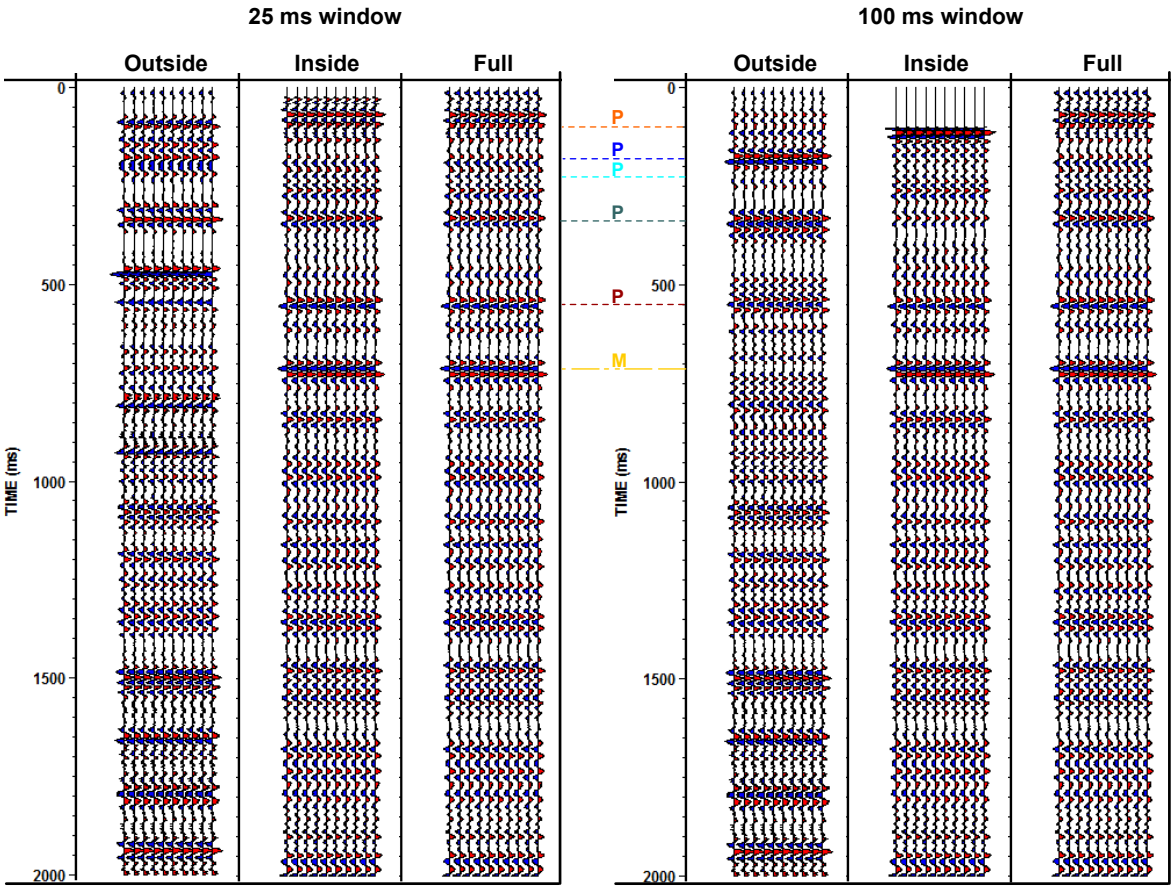

Fig. 4.13: Outside, inside and full corridor stack for a 25 ms and 100 ms window of the upgoing events after median filtering

4.4 Data Analysis

The processed zero-offset vertical seismic profile is the subject to analyse the velocity of the subsurface rocks at the Kimberly well, to extract information which assist in the interpretation of the borehole logs.

The first break times picked along the first arrival curve in section 4.3.1 are used to calculate the in-situ P-wave interval velocities (Figure 4.14). A linear least square fit of the picked arrival times with different window lengths of 10, 25 and 50 points was used to calculate the interval velocities and a fitting slope. In Figure 4.14, it is clearly seen, that with increasing window length, corresponding to depth intervals of 20 m, 50 m and 100 m, a smoothing of interval velocities was reached. But using larger intervals in the velocity calculations leads to a reduced resolution. Moreover, the linear slope and the confidence intervals are smoothed as well. Confidence intervals feature a 95 % change for holding the maximum and minimum values of the interval velocities. Looking at the interval velocities calculated with 10 depth points (i.e. 20 m), more detailed velocity information are revealed.

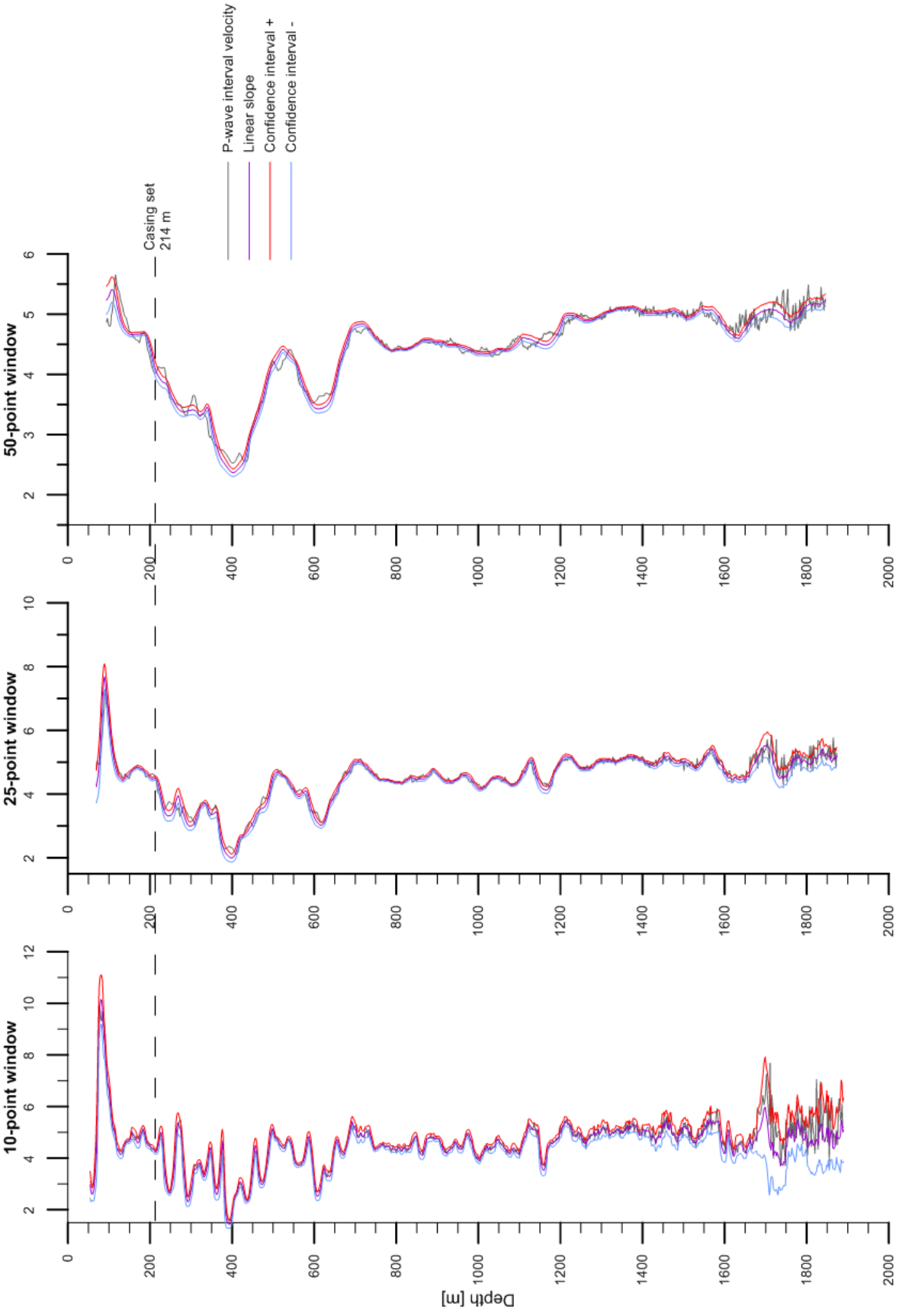

Fig. 4.14: P-wave interval velocities calculated from first break times of zero-offset VSP with different sampling ranges.

To support P-wave interval velocities, sonic log measurements in the form of a full waveform sonic were carried out. Sonic logging runs at a frequency of about 20 kHz and differs substantially from frequencies used to get VSP velocities (Schmitt et al., 2007). Resultant, both measurements lead to different frequency-dependent rock property and scaling effects.
In order to compare both in-situ velocity measurements, a variety of smoothing methods for the sonic curve are used. First, a simple arithmetic mean was applied as follows:

$$v_A(z) = \frac{\sum v_p(z_i)}{N} \tag{4.1}$$

As a long-wavelength approximation Backus average was used.

$$v_B(z) = \left[\frac{\sum v_p^{-2}(z_i)}{N}\right]^{-1/2} \tag{4.2}$$

And to cover high-frequencies, the harmonic average was applied on sonic velocities as well.

$$v_w(z) = \frac{N}{\sum v_p^{-1}(z_i)} \tag{4.3}$$

In all equations, N stands for the number of contiguous sonic log samples over a certain depth interval centered on a specific depths (z) (Schmitt et al., 2007).
In the same way as for the measured VSP velocities, different window length have been applied on the sonic velocity log. The results are represented in Figure 4.15. A window length of 50 depth points (i.e. 5 m) represents the best smoothing fit for sonic P-wave velocities. Based on the small depth sampling interval of 0.1 m of the FWS sonde, the interval velocities show significant variation. Although the sampling of the VSP data was much greater, minor fluctuations in the first break times, may cause variations below the sampling interval.

Along with the P-wave velocities, velocities for S- and Stoneley-waves were picked on the full waveform sonic. Finally, it was examined if the arithmetic mean, the Backus average and the harmonic average of the sonic P-wave lie within the confidence interval of the measured VSP velocities. As seen in the middle panel of Figure 4.16, it is proven that both interval velocities match one another except for quick velocity changes, where fractured zones lead to noisy data.
The difference between sonic log transit time and VSP interval velocities is based on rock composition, lateral inhomogeneity, attenuation and difference in wave propagation characteristics (Stewart, Huddleston, & Kan, 1984). Stewart et al. (1984) defined the time residual between VSP travel time and sonic log transit time as drift. The drift is positive if the seismic times are greater than the sonic transit times; negative drifts indicate higher sonic transit times than VSP times. Figure 4.16 reveals an increase in velocity with depth below 800 m.

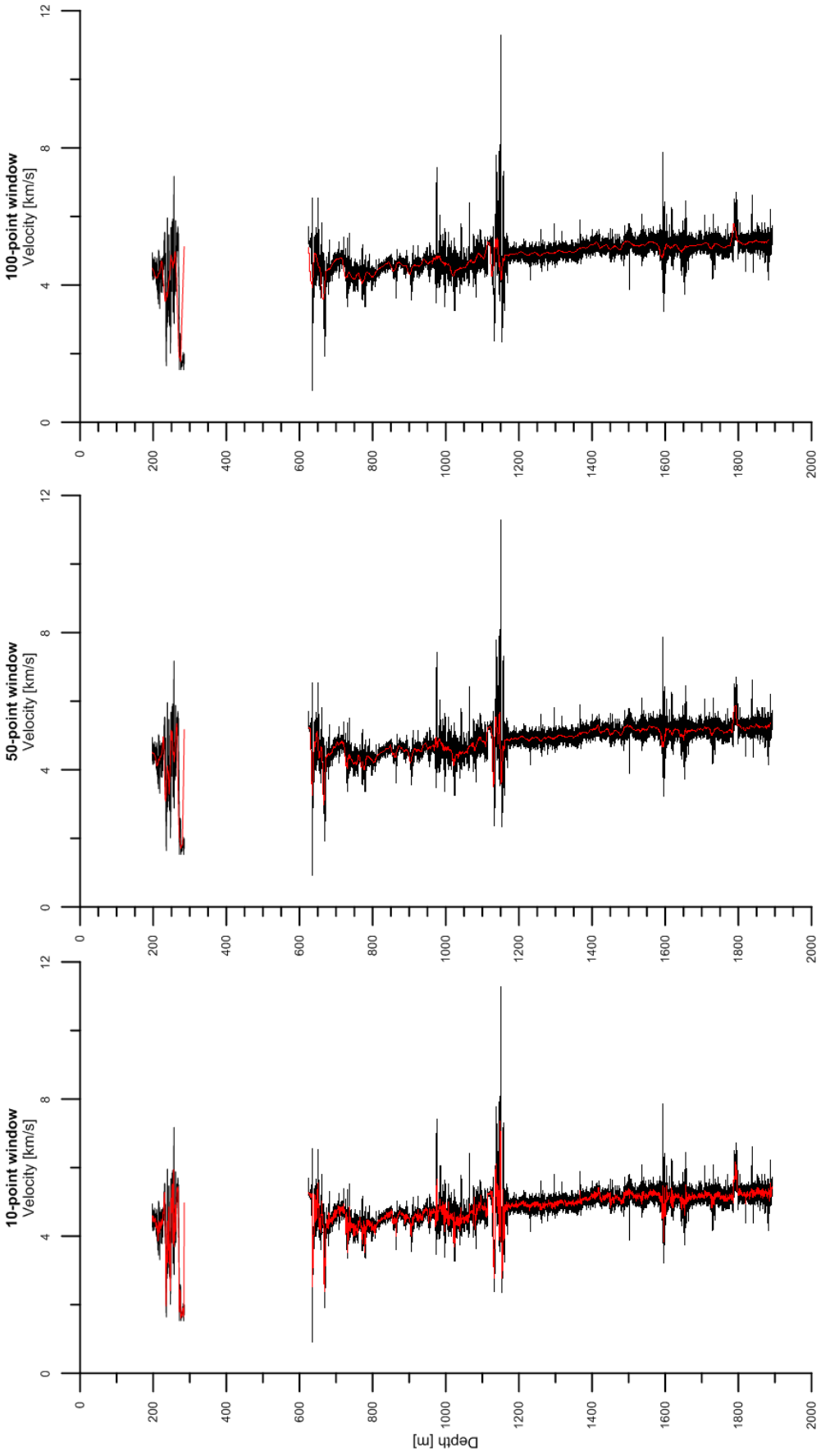

Fig. 4.15: Averaged sonic log P-wave velocities with arithmetic mean smoothing average for different window lengths.

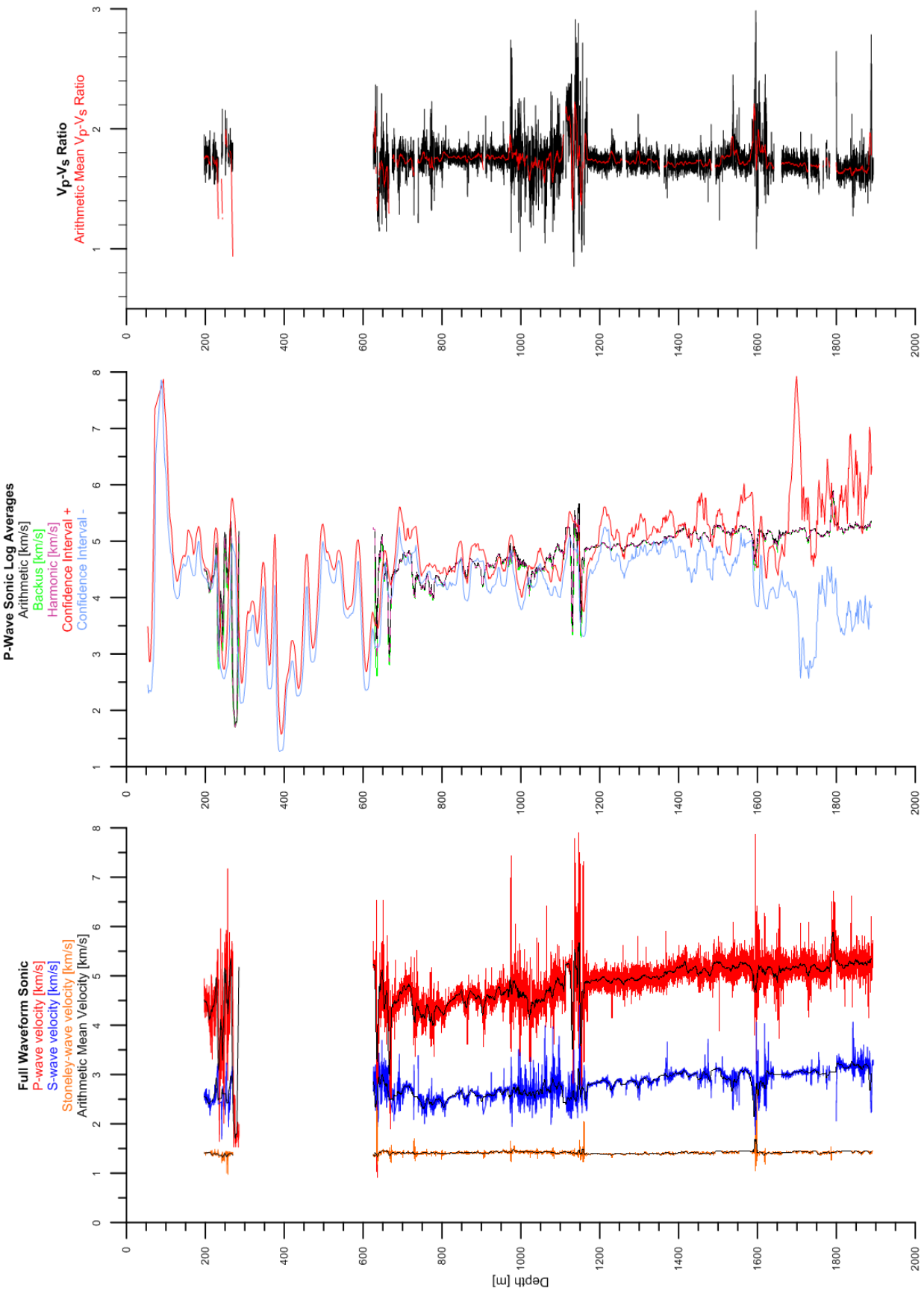

Fig. 4.16: Velocities of full waveform sonic and P-wave of VSP for comparison.

4.5 Summary

To obtain knowledge about flow boundaries in the subsurface of the Kimberly borehole a zero-offset vertical seismic profile was performed. The workflow including wavefield separation and the generation of a corridor stack are completed under the focus of identifying primary upgoing events and analysing acoustic rock properties. Except for first 150 m and some traces between 1600-1800 m depth the seismic section reveals good data quality. The calculated interval velocities of the first break curve which envelope the arithmetic P-wave sonic velocities match well (Fig. 4.17). The huge velocity increase in the first 100 m of the borehole is related to the high velocity basalt and possible picking errors of the first arrival due to noisy data. Strong changes in interval velocities correlate to lithologic changes and therefore an change in the acoustic properties. Although the interval velocity for the deepest rhyolite is relatively constant, the wide confidence interval of the interval velocities from the zero-offset data and smaller velocity decreases imply fractures in this unit.
The identified primary events and one multiple from the corridor stack can be correlated to changes in subsurface rocks. The summary plot comprising lithology, upgoing primary events after median filtering and the velocity profile, represents how the previous known geologic results match with responses from zero-offset VSP and sonic logging. The most apparent reflections are caused between rhyolite 3 and the lower basalt formation, at the basalt and sediment contact and at the sediment-rhyolite 2,1 contact. The prominent primary event at 550 ms seems to correspond to a fracture zone that is characterized by a decrease in velocity as well. The primary events outlined in Figure 4.17 can be subjected to errors of $\pm$ 20 ms.

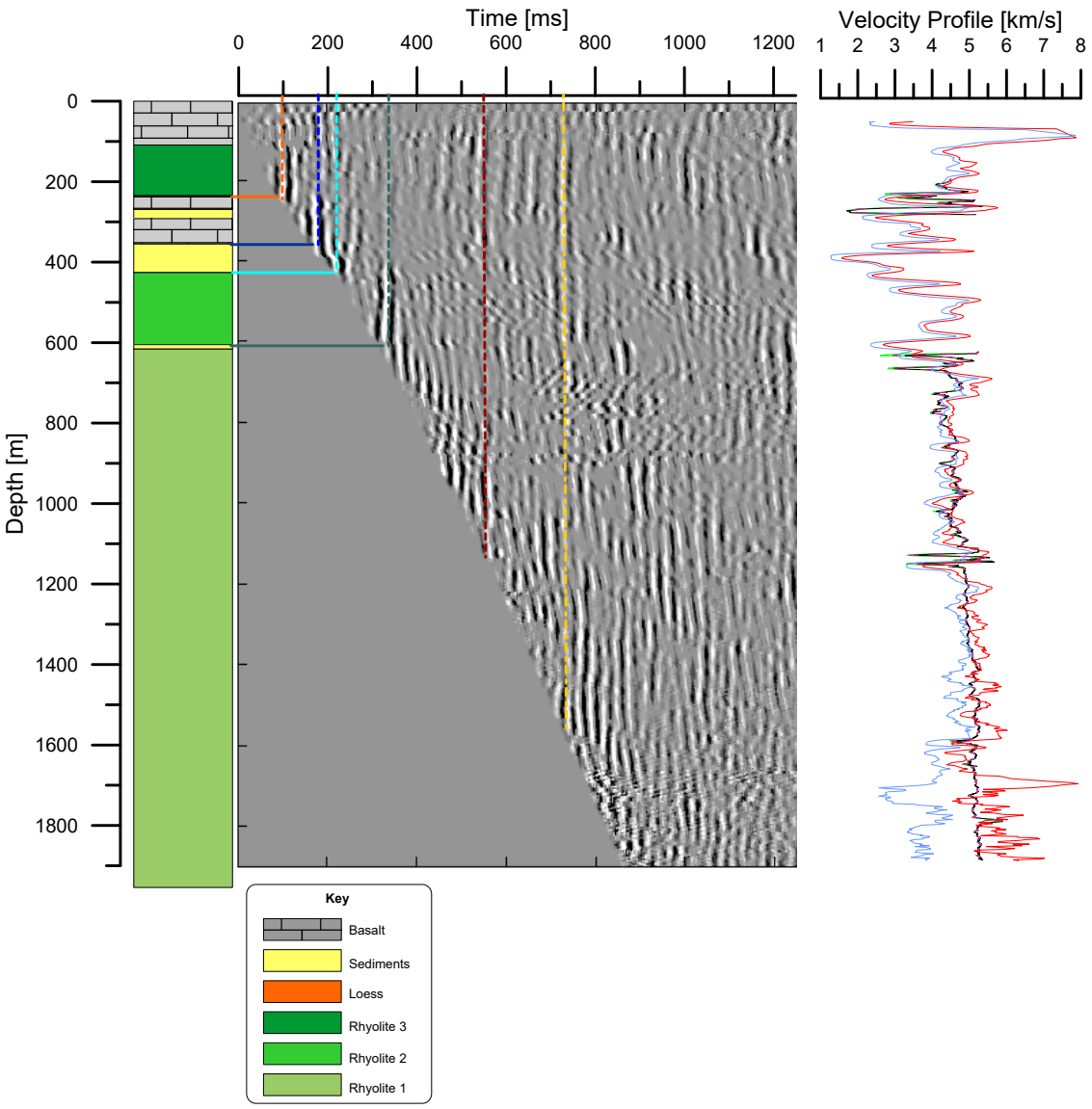

Fig. 4.17: Comprehensive overview on the results of the zero-offset VSP data processing and velocity analysis. Velocity display shows arithmetic sonic interval velocities (black) with corresponding confidence interval of the VSP velocities. The middle panel display the upgoing events generated after median filtering. Outlines of primary events are plotted with one identified multiple (yellow) at 720 ms. The velocity profile represents the confidence intervals of the VSP interval velocities and the arithmetic sonic velocity.

Chapter 5
Walk-Away Vertical Seismic Profile

A walk-away vertical seismic profile was acquired at the Kimberly well at 8 different receiver chain depths to obtain a better understanding for the different geological units and for possible seismic velocity anisotropy. Those anisotropic effects are related to directional variations of seismic velocities by fractures. Walk-away VSP surveys are conducted to specifically analyse objectives like amplitude versus offset, fracture detection and 2-D structural imaging. In comparison to the zero-offset VSP, the source of a walk-away VSP is stationed over several offsets along a line. If acquisition geometry is azimuthal orientated, estimates of dipping events are another objective to be examined. The processing workflow of such a kind of far-offset geometry will be directed towards a hodogram analysis to polarize the downgoing and upgoing P-wave energy.

5.1 Data Acquisition

The walk-away data acquisition at the Kimberly well involved the high-frequency Minivib as the seismic energy source, whereas shots were fired at a 4 m interval along the road adjacent to the Kimberly borehole for a length of about 0.48 km. The shot station number 2151 is the closest to the Kimberly borehole. The Sercel Slim Wave receiver array consisted of a 4 3-C geophones, which were spaced 10 m apart and placed at 8 different receiver depths. The first geophone of each chain was placed at 262 m, 562 m, 862 m, 1062 m, 1262 m, 1462 m, 1662 m and 1866 m depth. Just like for the zero-offset, the seismic source employed a 14 s linear taper sweep generated by frequencies of 10-160 Hz, which yields after correlation a 2 s traces sampled at 0.5 ms. Figure 5.1 summarizes the field geometry for the walk-away VSP at the Kimberly well with an approximate source-receiver offset distance of -90 to 397 m.

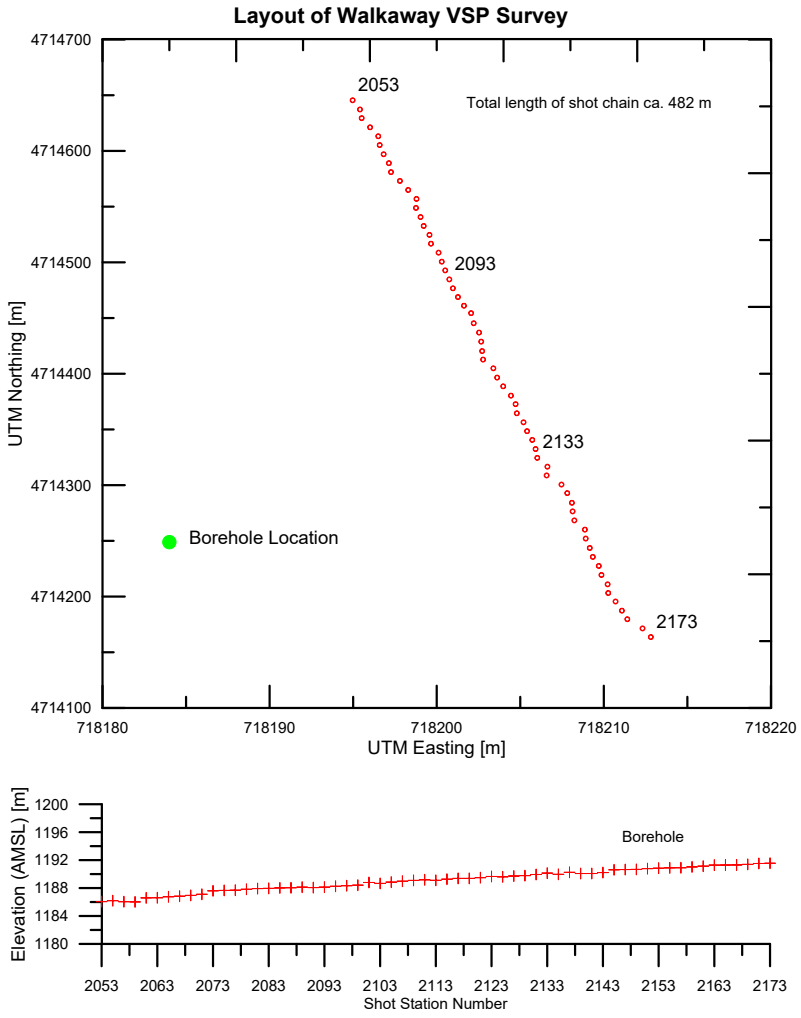

Fig. 5.1: Acquisition of the walk-away VSP along a road adjacent to the Kimberly borehole. The lower graph plots the elevation for each shot station.

5.2 Data Processing

In the same manner as for the zero-offset VSP data, the SEG-Y files for the different receiver depths were loaded in the VISTA^{TM} seismic data processing software package and were processed. The workflow for the walk-away VSP data of the Kimberly borehole involved geometry set-up, check of data quality, component separation, first break picking as well as hodogram rotation to separation downgoing- and upgoing events.

As the road on which the source was moved represents line no. 2 of the surface seismic survey, locations of the shot stations are the same. The coordinates of the shot stations help to set up the walk-away VSP geometry with source-receiver offsets. The data quality is mainly good, instead at deeper receiver depths where poor coupling results in a few noisy traces.

Component Separation and First Break Picking

The use of three-component geophones is a condition to perform walk-away vertical seismic profiling surveys, for example when nearly vertical rock faults are tried to be imaged. The target of the walk-away geometry is to image the changes of the so caused reflected and transmitted wavefields via two orthogonal and one vertical geophone (Hinds, 1996). After stacking, the data was separated according to the trace header in its X,Y and Z component by performing flow commands listed in Appendix B. In Figure 5.2 all three components for the 562 m deep receiver are shown. Each component contains 60 traces, which is why resolution is limited. Displays for the other receiver depths are deposited on the CD that is included in this thesis.

On all three components first arrivals can be identified and are picked along the first strongest arrival peak. Figure 5.3 presents all first arrival picks for every receiver chain. The travel-time curves should be hyperbolas as the arrival times of reflections from an interface at a certain depth are functions of source-receiver offset. But only for the first receiver depths starting at 262 and 562 m depth moveout with offset is noticeable. Moreover, large static time shifts in a repeatable pattern occur over the whole range of receivers. At the borehole location two-way travel time static shifts of nearly 30 ms are observed (Liberty, Schmitt, & Shervais, 2014). Liberty et al. (2014) stated that these static effects should be addressed with advanced seismic processing methods, like a refraction static analysis with tomography methods. For this purpose, it was tried to pick the first arrival of the surface seismic data along line 2 in the GeoTomo seismic tomography package and apply a static correction method. Due to the volcanic environment of the surface resulting in large velocity and density contrasts, no satisfied picking was possible and static correction therefore failed. Although first break picks should be analysed further and corrected, the processing workflow was continued and a hodogram analysis was performed.

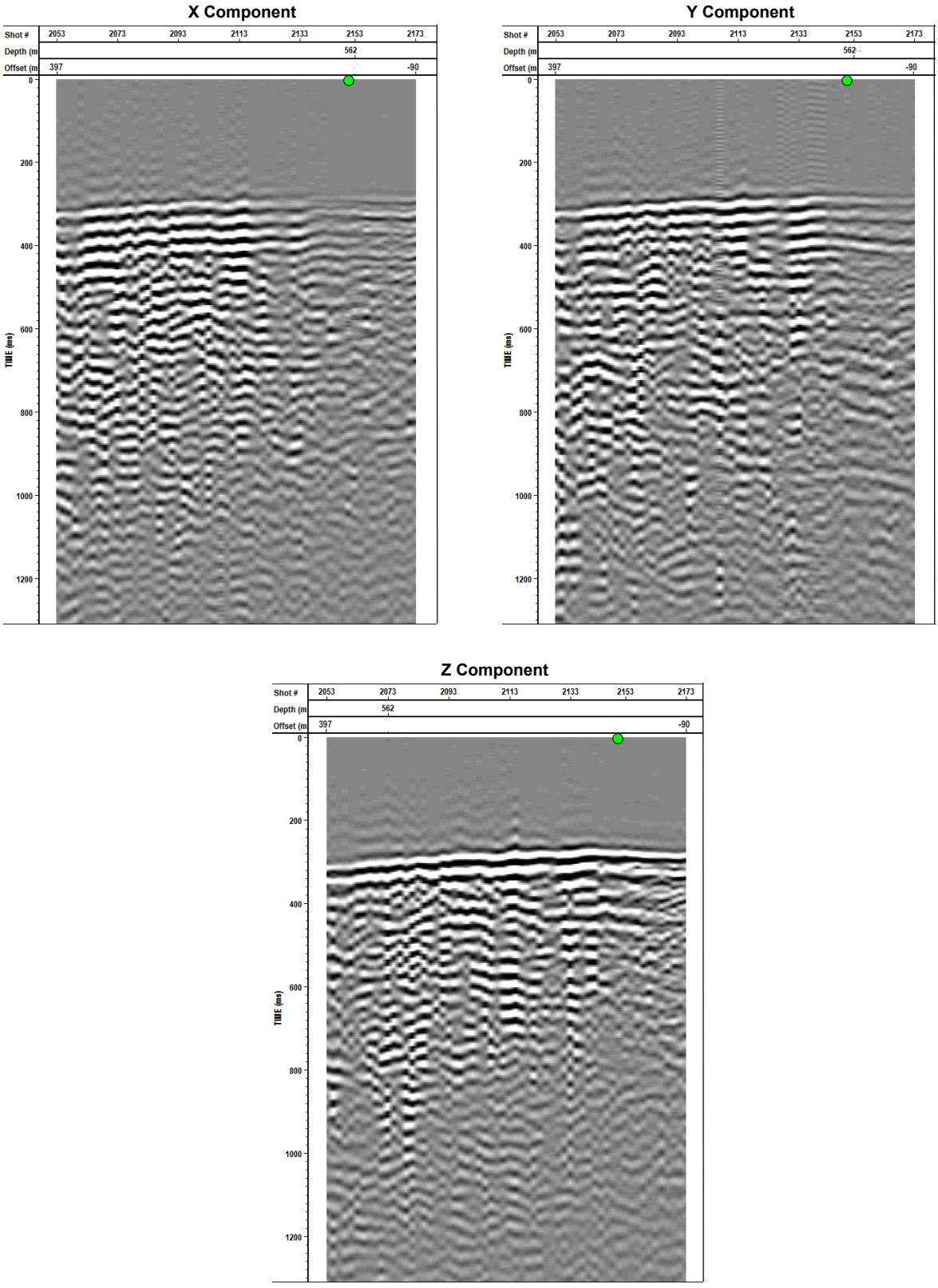

Fig. 5.2: Three component display of the walk-away vertical seismic profile at 562 m depth in common receiver gather. All three panels were zoomed for better display. Green circle represents the surface location of the Kimberly borehole.

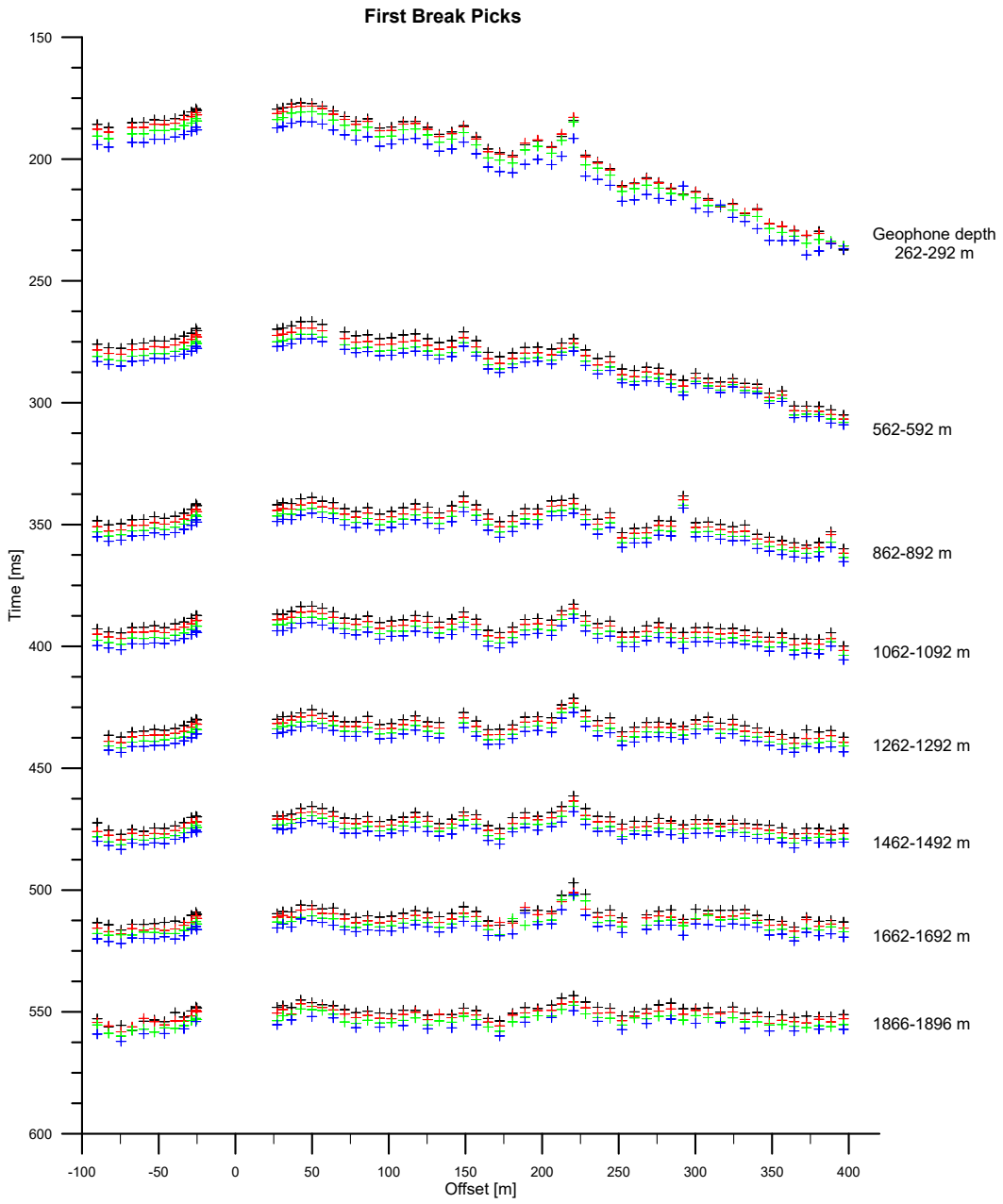

Fig. 5.3: First arrival picks of the Kimberly walk-away VSP data. For every receiver chain, different marker colours are used to represent first to fourth geophone. Static time shifts appear on the whole range of receiver depths and reduce data quality.

Hodogram Analysis

While acquiring the vertical seismic profile data the geophones rotate when moving to the next receiver depths; this has effects on the directional recordings of horizontally (SH) and vertically (SV) shear waves, and compressional P-wave energy. The hodogram analysis polarizes the data channels to isolate those varying amounts of energy events (Hinds, 1996). By using a hodogram, a plot of motion of a point as a function of time, determines the direction of wave energy and the orientation of the receivers (Sheriff, 2002). The hodogram analysis comprises two rotations to isolate downgoing and upgoing P-wave events. In the first rotation the horizontal X-Y plane is orientated inline towards the source and is referred to the radial component HMAX. The orthogonal component of the first rotation is called HMIN. On the HMAX panel SV and P-wave energy is polarized.
The second rotation separates the P and SV waves by polarization on the Z and the HMAX data to yield Z' and HMAX' as output data. Whereas the HMAX' data panel contains upgoing SV and downgoing P-wave energy, predominately downgoing SV and upgoing P-wave energy is represented in the Z' data panel (Hinds, 1996). The rotation procedure is visualized in Figure 5.4. Figure 5.5 displays the two-step hodogram analysis for the data set where receivers are positioned at 562 m depth. All other receiver depths with there corresponding hodogram rotation are deposited on the enclosed CD. Despite visible static time shifts downgoing P-wave energy is extract on the Z' data panel. Vertically polarized shear-wave energy does not emerge on the data panels. The deeper the receivers are positioned in depth the less energy is recorded and the identification of events is complicated.

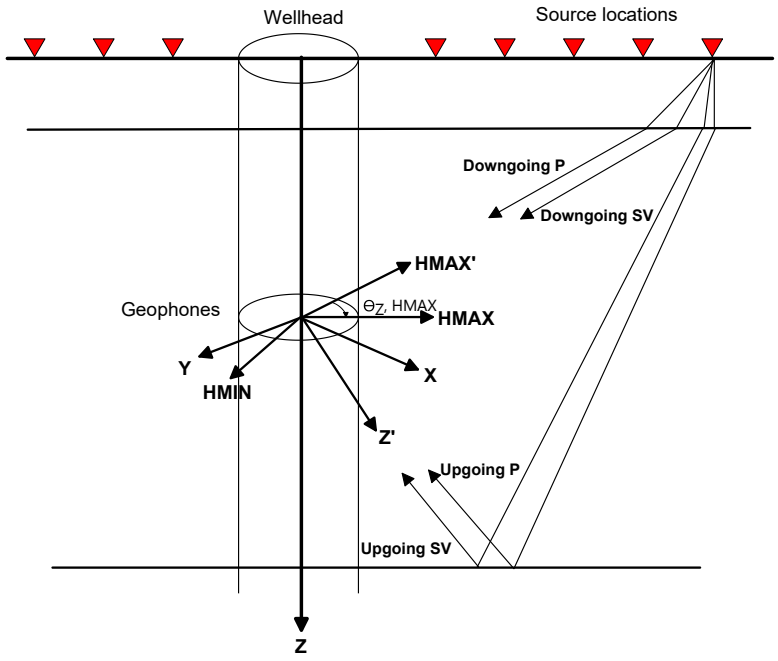

Fig. 5.4: Field layout of a walk-away VSP survey with an orthogonal coordinate system of the local X,Y,Z geophones. Through a two-step rotation procedure the data is rotated into new planes HMAX, HMIN, HMAX' and Z'. The resultant planes contain polarized P- and SV-energy. Adapted from Hinds et al. (1996).

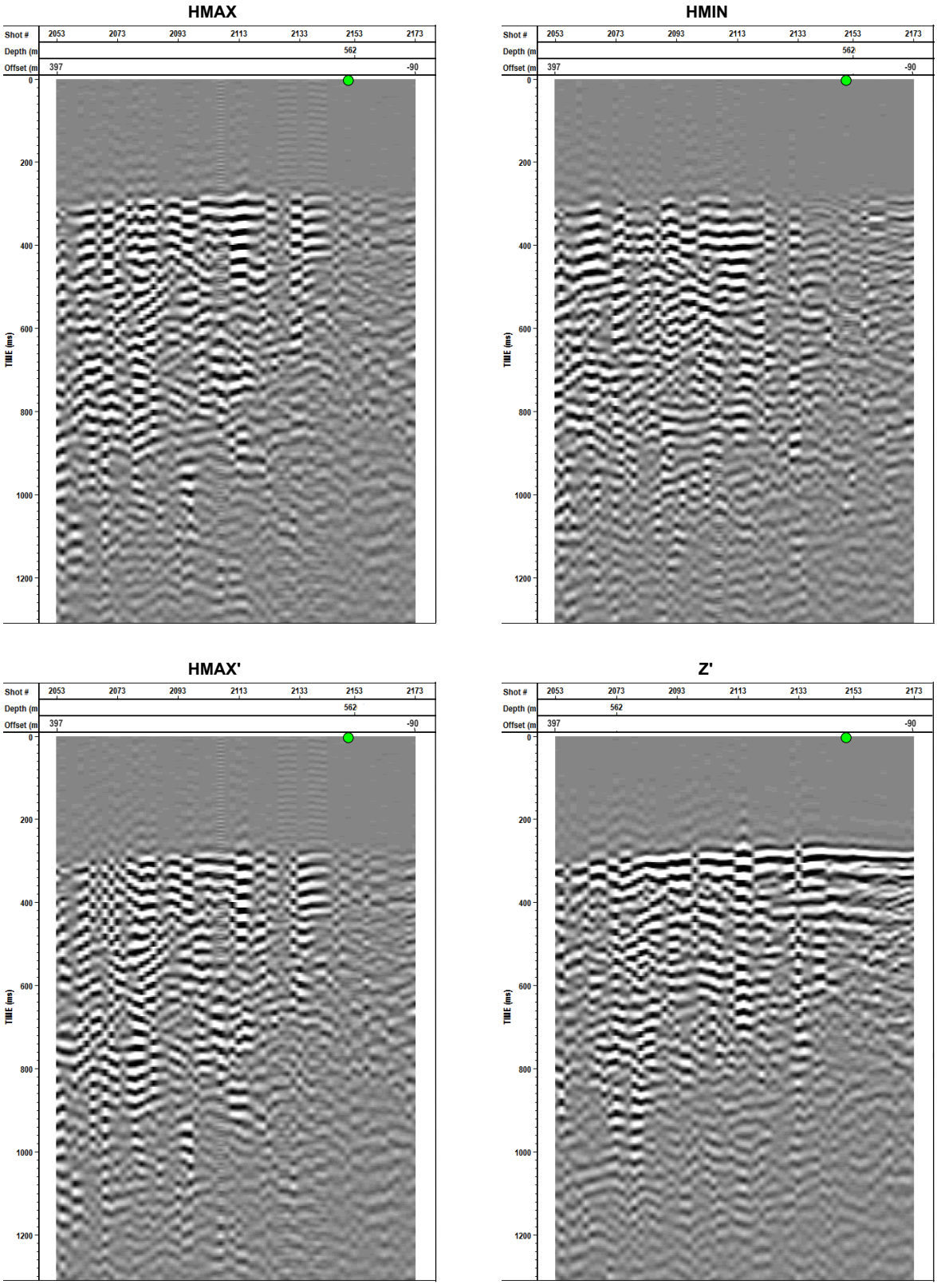

Fig. 5.5: First rotation is performed by both horizontal (X and Y) receivers at 562 m depth to yield the outputs of HMAX and HMIN in the upper two panels. The second rotation is performed by inputting the horizontal radial component HMAX and the vertical Z component at 562 m depth to receive HMAX' and the transverse Z' component in the lower panel. All four panels were zoomed for better display. Green circle represents the surface location of the Kimberly borehole.

5.3 Summary

A walk-away vertical seismic profile survey along a road adjacent to the Kimberly borehole was conducted and processed with focus on first arrival picking and hodogram analysis. As traveltime curves reveal large time shifts which correspond to near-surface effects, a detailed velocity analysis was not possible. Attempts to correct static time shifts are only successful if an accurate velocity model is generated, which improves the seismic imaging results. A major impediment is the missing density and velocity information for the top basalt. The interval velocities of the zero-offset VSP already demonstrated large changes in velocity for this section. If the static shifts are removed, hodogram displays of the HMAX, HMIN, HMAX' and Z' component will improve and can be analysed for anisotropy further.

Chapter 6
Conclusions

Geothermal power generation is already an essential component in Idaho's energy economy. But with projects like HOTSPOT scientists seek ways to find areas which, due to their high geothermal gradient and geologic history, are promising and which can be used extensively for geothermal power generation. An important component for such a feasibility study is a deep borehole that offers an unique image of the subsurface. Such a comprehensive study is designed to characterize the subsurface by integrating seismic with borehole measurements. It shall be exploited if the subsurface rocks are fractured and if this fractured rock has an enhanced fluid potential and my serve as an environment for the development of a geothermal system.

Within the project HOTSPOT, three drill sites are selected across the Snake River Plain to investigate the geothermal energy resource at depth utilizing geological, geochemical and geophysical techniques. The Kimberly drill site located at the southwest margin of the Twin Falls volcanic center in the town of Kimberly, Idaho, USA is the focus of this thesis. The vertical well was completed in June 2011 to a depth of 1956 m, providing insight in the volcanic stratigraphy of basalt and rhyolite interbedded with sediments. The project included two 2-D surface seismic lines, two types of vertical seismic profiling (VSP) and borehole log measurements. The scope of this thesis involves further processing and interpretation of vertical seismic profiling data and borehole logs.
As there is only a limited amount of Kimberly core boxes available to analyse at the University of Alberta, the thesis focuses on the geophysical well log data available. Geophysical well logs assist in exploring permeable pathways and fractures by analysing the in-situ rock properties of the geological formations. This also includes acoustic responses of the rock properties which help with processing and interpretation of surface and borehole seismic surveys. The following section summarizes the key observations from the geophysical logs at the Kimberly well.

Although the types of rocks were determined during the logging program via core sampling, the responses of the spectral gamma ray log helped in delimiting the various volcanic and sedimentary rock formations. In the section above the casing (213 m) where no rock samples were acquired the interface of basalt and rhyolite 3 is mapped. The subsequent successions of interbedded basalt and sediment are correlated to changes in natural gamma ray and magnetic susceptibility. A distinctive response of increase provides the neutron log for the topmost basalt, concluding that the texture is of a vesicular state.
The radiogenic heat production of the drill site was calculated by two approaches. The responses of natural gamma ray log estimated a radiogenic heat generation of 3.33 $\mu W/m^3$ and the second approach yielded a value of 3.03 $\mu W/m^3$ by including spectral gamma ray measurements and density values. Thereby, density values were concluded from literature values and two probes of rhyolite 1 and 3 in the laboratory. Due to $\rho_{Rhyolite1} = 2469\ kg/m^3$ and $\rho_{Rhyolite3} = 2418.6\ kg/m^3$ we gained knowledge of the density in the most prominent rhyolite 1 section. The values of the calculated radiogenic heat production offer an optimistic view for geothermal power generation.
Anomalous changes in the caliper, the resistivity of the dual laterolog, magnetic susceptibility and the transit time of the full waveform sonic log revealed a number of localized natural frac-

tures. Especially, fracture zones around 1128-1162 m, 1590-1602 m and 1785-1805 m emerge in the more consistent hard rock environment. Natural fractures in the top of the rhyolite 1 reveal many fluctuations of the analysed physical parameters due to a brittle texture and fissures. In this case, the fracture zones are considered to be highly porous, open fractures since a decrease in neutron log corresponds to a higher hydrogen content and higher porosity of the formation. For the full waveform sonic a fracture zone always accompanies with attenuation of the waveform.
The time picks of the full waveform sonic log revealed average P-,S- and Stoneley wave velocities of 4.87 km/s, 2.81 km/s, and 1.42 km/s respectively in 625-1892 m depth associated with the ryholite 1. Over the same depth section the V_p/V_s ratio of the velocity profile is 1.73.

With the help of the televiewer log, natural fractures, drilling induced fractures, and borehole breakouts were tried to localize. Sedimentary and basaltic units (211-388 m depth) obtained weakly dipping events of a mean dip angle of 40.6° as well as a mean strike azimuth of 185.3°. In rhyolite 1 between 635-1128 m natural fractures with an average dip of 57.2° and a mean strike azimuth of 167.4° are visible. In addition, layering and bedding in both sections were observed, resulting in a smaller dipping angle. But drilling induced fractures and borehole breakouts have not yet been identified because only an alignment to the same features on the actual cores can ensure the presumption. Nevertheless, various changes in the dip angle over the whole rhyolite 1 unit indicate rheomorphic folding with changes in stress direction. Although image data is not available for the entire borehole, with a combination of the conventional geophysical logs it is possible to analyse and interpret a number of fracture zones. It must be noted that the fractured zones are classified by direct interpretations of the image logs and indirectly by observations made from the conventional geophysical logs.

A zero-offset vertical seismic profile was acquired to establish a time-depth relation of the volcanic flow boundaries. Despite the large seismic velocity and density contrast between the thin sediment interbeds and volcanic rocks it was possible to image the interfaces of the formations due to their impedance contrast. By generating a corridor stack it was possible to distinguish between reflectors and multiples. The analysis of the seismic velocity profiles from both full waveform sonic and first break picks of the VSP does not only prove useful for seismic processing but also for interpretation of low velocity zones which could indicate fracture zones. The seismic velocities show an increase with depth caused by an increase in pressure from overburden.

The walk-away vertical seismic profile was collected along line 2 of the surface seismic profile at 8 different receiver depths. Large time shifts superimpose the data, which affect the first arrival picking and the subsequent processing of the data. A hodogram analysis should helped with determining the anisotropy in the borehole but as static time shifts could not have been erased by tomography at this stage, no further processing was done.

Future work should include the extension of geophysical logs and the coverage of the walk-away vertical seismic profile. By performing density measurements in the borehole, information about the formation bulk density could be determined and consequently values of the formations porosity could be derived. Density measurements are useful for generating a synthetic seismogram and therefore for comparing the corridor stack with the synthetic response. In the processing routine of the zero-offset VSP, the deconvolution step should be supplemented to erase multiples from the data set. A further feature to be analysed could be the attenuation behaviour of the first arrival with depth.
It would be advisable for the walk-away VSP to extend the offset of the layout to image

the subsurface more precise. The technique behind the paper of Schijns, Heinonen, Schmitt, Heikkinen, and Kukkonen (2009) is an application in which static time shift corrections could be implemented. This also requires reprocessing of the surface seismic data on line 2. As a final step a migration, or a so called common depth point transformation (VSP-CDP), could follow to map the reflections in terms of the VSP geometry and the input velocity model. Finally I would like to conclude, that an ultimate interpretation can only be performed when a merger of comprehensive measurements is done. Further measurements would help to enhance the results and to image a broader area of the borehole.

Implications from the previous stated conclusions for geothermal exploration imply that deeper drilling into the rhyolite is required to reach higher temperatures of at least 85°C. Moreover, fractures identified in borehole logs and seismic velocity profiles provide assistance when developing a geothermal power plant by functioning as fluid pathways between injection and production well.

References

Allaby, M. (2008). *A dictionary of earth sciences: Autobrecciated lava* (3rd ed.). Oxford and New York. Retrieved from http://www.oxfordreference.com/view/10.1093/oi/authority.20110810104412649

ALT sàrl. (2002). *Fac40 televiewer: Notes on use and operation.* Retrieved from http://hazzazi-sa.somee.com/FAC40_OpMan.pdf

Bates, R. L., & Jackson, J. A. (1984). *Dictionary of geological terms* (3. ed. ed.). New York - London etc: Doubleday.

Beaumont, E. A., & Foster, N. H. (1989). *Geophysics ii: Tools for seismic interpretation* (Vol. no. 13). Tulsa, Okla.: American Association of Petroleum Geologists.

Bigelow, E. L. (1995). *Introduction to wireline log analysis.* Houston, Texas: Baker Atlas.

Blackwell, D. D. (1989). Regional implications of heat flow of the snake river plain, northwestern united states. *Tectonophysics*, *164*(2-4), 323–343. doi: 10.1016/0040-1951(89)90025-5

Bonnichsen, B., & Godchaux, M. M. (2002). Late miocene, pliocene, and pleistocene geology of southwestern idaho with emphasis on basalts in the bruneau-jarbidge, twin falls, and western snake river plain regions. In *Bonnichsen, b., white, c.m., mccurry, m. (eds), tectonic and magmatic evolution of the snake river plain volcanic province: Idaho geological survey 30* (Vol. 30, pp. 233–312). Moscow, Id.: Idaho Geological Survey, University of Idaho.

Bonnichsen, B., White, C., & McCurry, M. O. (2002). *Tectonic and magmatic evolution of the snake river plain volcanic province* (Vol. 30). Moscow, Id.: Idaho Geological Survey, University of Idaho.

Branney, M. J., Bonnichsen, B., Andrews, G. D. M., Ellis, B., & Barry, T. L., McCurry, M. (2008). 'snake river (sr)-type' volcanism at the yellowstone hotspot track: distinctive products from unusial high-temperature silicic super-eruptions. *Bulletin of Volcanolgy*, *70*, 293–314.

Branney, M. J., Bonnichsen, B., Andrews, G. D. M., Ellis, B., Barry, T. L., & McCurry, M. (2008). 'snake river (sr)-type' volcanism at the yellowstone hotspot track: Distinctive products from unusual, high-temperature silicic super-eruptions. *Bulletin of Volcanology*, *70*(3), 293–314. doi: 10.1007/s00445-007-0140-7

Brott, C. A., Blackwell, D. D., & Ziagos, J. P. (1981). Thermal and tectonic implications of heat flow in the eastern snake river plain, idaho. *Journal of Geophysical Research*, *86*(B12), 11709. doi: 10.1029/JB086iB12p11709

Brott, C. A., Blackwell, D.D. & Mitchell, J.C. (1976). *Geothermal investigations in idaho: Heat flow in the snake river plain region, southern idaho.*

Bücker, C., & Rybach, L. (1996). A simple method to determine heat production from gamma-ray logs. *Marine and Petroleum Geology*, *13*(4), 373–375. doi: 10.1016/0264-8172(95)00089-5

Christiansen, E. H., McCurry, M., Bindeman, I., Champion, D., Knott, T., Branney, M. J., ... Shervais, J. (n.d.). *Rhyolites in the kimberly drill core, project hotspot: First intraccaldera ignimbrite from the central snake river plain, idaho?* San Francisco.

DOSECC. (n.d.). News for the continental scientific drilling community. *DOSECC*, *7*(2).

Ellis, D. V., & Singer, J. M. (2007). *Well logging for earth scientists* (2nd ed.). Dordrecht, The Netherlands: Springer.

Fleischmann, D. J. (2006). *Geothermal development needs in idaho.* Retrieved from http://geo-energy.org/reports/Idaho%20Geothermal%20Report.pdf

Geologic field trips to the basin and range, rocky mountains, snake river plain, and terranes of the u.s. cordillera. (2011). Geological Society of America.

Grey, L. d., & Link, P. (n.d.). *Digital geology of idaho: Snake river plain aquifer.* Retrieved from http://geology.isu.edu/Digital_Geology_Idaho/Module15/mod15.htm

Haase, A. B. (n.d.). *Q-estimation from uncorrelated vibroseis vsp model data.* Calgary.

Hajnal, Z., White, D. J., Reilkoff, B., Adam, E., Bellefleur, G., Koch, R., Powell, B., & Annesley, I. R. (n.d.). *Exteck iv sub-project 1: Seismic studies at the mcarthur river mining camp: Summary of investigations 2001.*

Hallenburg, J. K. (1984). *Geophysical logging for mineral and engineering applications.* Tulsa, Oklahoma: PennWell Books.

Hanan, B. B., Shervais, J. W., & Vetter, S. K. (2008). Yellowstone plume–continental lithosphere interaction beneath the snake river plain. *Geology*, *36*(1), 51. doi: 10.1130/G23935A.1

Hardage, B. A. (1983). *Vertical seismic profiling: Part a: Principles* (Vol. Volume 14A). London: Geophysical Press.

Helm-Clark, C. M., Rodgers, D. W., & Smith, R. P. (2004). Borehole geophysical techniques to define stratigraphy, alteration and aquifers in basalt. *Journal of Applied Geophysics*, *55*(1-2), 3–38. doi: 10.1016/j.jappgeo.2003.06.003

Hinds, R. C. (1996). *Vsp interpretive processing: Theory and practice* (Open File Publication No.3 ed.). Tulsa, Oklahoma: Society of Exploration Geophysicists.

Hughes, S. S., & McCurry, M. (2002). Bulk major and trace element evidence of a time-space evolution of snake river plain rhyolites, idaho. In *Bonnichsen, b., white, c.m., mccurry m. (eds) tectonic and magmatic evolution of the snake river plain volcanic province: Idaho geological survey bulletin 30* (Vol. Idaho Geological Survey Bulletin 30, pp. 161–176).

Hughes, S. S., Wettmore, P. H., & Casper, J. L. (2002). Evolution of quaternary tholeiitic basalt eruptive centers on the eastern snake river plain, idaho. In *Bonnichsen, b., white, c.m., mccurry, m. (eds), tectonic and magmatic evolution of the snake river plain volcanic province: Idaho geological survey bulletin 30* (pp. 363–385).

Humphreys, E. D., Dueker, K., G., Schutt, D. L., & Smith, R. B. (2000). Beneath yellowstone: Evaluation plume and nonplume models using teleseismic images of the upper mantle. *Geological Society of America*, *10*(12).

Idaho State University. (n.d.). *Gis training and research center.* Retrieved from http://giscenter.isu.edu/Data/index.htm

Johnson, R. W. (1989). *Intraplate volcanism in eastern australia and new zealand.* Cambridge, UK: Cambridge University Press.

Käppler, R. (2014). *Bohrlochgeophysik (pdf document).* Freiberg. Retrieved from http://tu-freiberg.de/geophysik/teaching/bohrlochgeophysik

Knott, T., Branney, M. J., Christiansen, E. H., Reichow, M., McCurry, M., & Shervais, J. (n.d.). *Drilling a 'super-volcano': volcanology of the proximal rhyolitic volcanic succession in the hotspot deep drill hole, idaho, yellowstone hot-spot track* (No. V13D-2649). San Francisco.

Krammer, K. (1990). Magnetic susceptibility log measured in hole395a, leg 109. *Proceedings of the Ocean Drilling Program, Scientific Results*, *106*(109), 231–235.

Kück, J. (n.d.). *Icdp-osg at gfz - downhole logging srsdp kimberly 2011.*

Kück, J. (18.03.2015). *Personal communications.*

Leeman, W. P. (1982). *Development of the snake river plain-yellowstone plateau province,*

idaho and wyoming: An overview and petrologic model. Moscow, Idaho: Cenozoic Geology of Idaho. Retrieved from `http://geology.isu.edu/Digital_Geology_Idaho/papers/B-26Ch3-2.pdf`

Leeman, W. P., Annen, C., & Dufek, J. (2008). Snake river plain - yellowstone silicic volcanism: implications for magma genesis and magma fluxes. *Geological Society, London, Special Publications*, *304*(1), 235–259. doi: 10.1144/SP304.12

Liberty, L. M., Schmitt, D. R., & Shervais, J. W. (n.d.). *Seismic imaging through volcanic rocks of the snake river plain, idaho: Icdp project hotspot: Paper presented at society of exploration geophysicists 82nd annual meeting, society of exploration geophysicists las vegas.*

Moon, W., Carswell, A., Tang, R., & Dilliston, C. (1986). Radon transform wave field separation for vertical seismic profiling data. , *51*(4), 940–947. doi: 10.1190/1.1442151

Mwenifumbo, C. J., & Mwenifumbo, A. L. (2012). Borehole geophysical logging in the flin flon mining camp. *Geological Survey of Canada, Open File 6547*. doi: 10.4095/291534

Nielson, D. L., & Shervais, J. W. (2014). *Conceptual model for snake river plain geothermal systems based on slim-hole exploration at mountain home, idaho.*

Nielson, D. L., Delahunty, C., Shervais, J. W. (2012). Geothermal systems in the snake river plain, idaho, characterized by the hotspot project. *Geothermal Resources Council Transactions*, *36*, 727–730.

Pasquale, V., Chiozzi, P., & Verdoya, M. (2014). *Geothermics: Heat flow in the lithosphere.* Cham [u.a.]: Springer. doi: 10.1007/978-3-319-02511-7

Patlan, E. (n.d.). *Drilling induced fracture (dif) characterization and stress pattern analysis of the southern mcmurdo sound (sms) core, victoria land basin, antarctica.* El Paso.

Pierce, K. L., Morgan, L. A., & Saltus, R. W. (2002). Yellowstine plume heas: Postulated tectonic relations to the vancouver slab, continental boundaries, and climate. In *Bonnichsen, b., white, c.m., mccurry, m. (eds.), tectonic and magmatic evolution of the snake river plain volcanic province: Idaho geological survey bulletin 30* (pp. 5–33).

Pujol, J., Fuller, B. N., & Smithson, S. B. (1989). Interpretation of a vertical seismic profile conducted in the columbia plateau basalts. *Geophysics*(54(10)), 1258–1266. doi: 10.1190/1.1442585

Reinecker, J. (2003). *Borehole breakout analysis from four-arm caliper logs.*

Rodgers, D. W., Ore, H. T., Bobo, R.T., McQuarrie, N., & Zentner, N. (2002). Extension and subsidence of the eastern snake river plain, idaho. In *Bonnichsen, b., white c.m., mccurry, m. (eds.), tectonic and magmatic evolution of the snake river plain volcanic province: Idaho geological survey bulletin 30* (pp. 121–155).

Schijns, H., Heinonen, S., Schmitt, D. R., Heikkinen, P., & Kukkonen, I. T. (2009). Seismic refraction traveltime inversion for static corrections in a glaciated shield rock environment: A case study. *Geophysical Prospecting*, *57*(6), 997–1008. doi: 10.1111/j.1365-2478.2009.00798.x

Schlumberger. (1991). *Log interpretation principles/applications* (3rd ed.). Houston, Texas: Schlumberger Educational Services.

Schmitt, D. R. (2007). In situ seismic measurements in borehole lb-08a in the bosumtwi impact structure, ghana: Preliminary interpretion. *Meteoritics & Planetary Science*, *42*(4/5), 755–768.

Schön, J. (1983). *Petrophysik: physikalische eigenschaften von gesteinen und mineralen.* Berlin: Akademie-Verlag.

Schön, J. H. (2011). *Physical properties of rocks - a workbook: Handbook of petroleum exploration and production* (8th ed.). Oxford, UK: Elsevier.

Shazly, T. F., & Tarabees, E. (2013). Using of dual laterolog to detect fracture parameters for nubia sandstone formation in rudeis-sidri area, gulf of suez, egypt. *Egyptian Journal of Petroleum*, *22*, 313–319. doi: 10.1016/j.ejpe.2013.08.001

Sheriff, R. E. (2002). *Encyclopedic dictionary of applied geophysics* (4th ed.). Tulsa, Oklahoma: Society of Exploration Geophysicists. doi: 10.1190/1.9781560802969

Shervais, J. W. (2001). *Intermediate depth drilling of the snake river plain in support of earthscope: Tracking the yellowstone plume through space and time.*

Shervais, J. W., Shroff, G., Vetter, S. K., Matthews, S., Hanan, B. B., & McGee, J. (2002). Origin and evolution of the western snake river plain: Implications from stratigraphy, faulting, and the geochemistry of basalts near mountain home, idaho. In *Bonnichsen, b., white, c.m., mccurry, m. (eds), tectonic and magmatic evolution of the snake river plain volcanic province: Idaho geological survey 30* (pp. 343–361).

Shervais, J. W., Vetter, S. K., & Hanan, B. B. (2006). A layered mafic sill complex beneath the easter snake river plain: Evidence from cyclic geochemical variations in basalt. *Geology*(v.34), 365–368.

Shervais, J. W., & Vetter, S. K. (2009). High-k alkali basalts of the western snake river plain (idaho): Abrupt transition from tholeiitic to mildly alkaline plume-derived basalts, western snake river plain, idaho. *Journal of Volcanology and Geothermal Research*, *188*(1-3), 141–152. doi: 10.1016/j.jvolgeores.2009.01.023

Shervais, J. W., Evans, J. P., Christiansen, E. J., Schmitt, D. R., Liberty, L. M., Blackwell, D. D., Glen, J. M., Kessler, J. E., Potter, K. E., Jean, M. M., Sant, C. J., & Freeman, T. G. (2011). Hotsport: the snake river geothermal drilling project - an overview. *Geothermal Resources Council Transactions*, *35*.

Shervais, J. W., Kauffmann, J. D., Gillerman, V. S., Othberg, K. L., Vetter, S.K., Hobson, V. R., Zarnetske, M., Cooke, M. F., Matthews, S. H., & Hanan, B. B. (2005). Basaltic volcanism of the central and western snake river plain: A guide to field relations between twin falls and moutain home, idaho. *Geological Society of America*, *Field Guide 6*.

Shervais, J. W., Schmitt, D. R., Nielson, D., Evans, J. P., Christiansen, E. H., Morgan, L., Shanks, W. C. P., Prokopenko, A. A., Lachmar, T., Liberty, L. M., Blackwell, D. D., Glen, J. M., Champion, D., Potter, K. E., Kessler, J. A. (2013). First results from hotspot: The snake river plain scientific drilling project, idaho, usa. *Scientific Drilling*(15), 36–45. doi: 10.2204/iodp.sd.15.06.2013

Shervais, W. J., Shroff, G., Vetter, S. K., Matthews, S., Hanan, B. B., & McGee, J. J. (2002b). Origin and evolution of the western snake river plain: Implications from stratigraphy, faulting, and the geochemistry of basalts near mountain home, idaho. *Geological Society of America*, *31/4*(A55).

Smith, R. P. (2004). Geologic setting of the snake river plain aquifer and vadose zone. *Vadose Zone Journal*, *3*(1), 47–58. doi: 10.2113/3.1.47

SMU Geothermal Lab. (2011). *Geothermal map of north america.* Retrieved from `http://www.smu.edu/Dedman/Academics/Programs/GeothermalLab/DataMaps/GeothermalMapofNorthAmerica`

Stewart, R. R. (1985). Median filtering: Review and a new f/k analogue design. *Journal of the Canadian Society of Exploration Geophysicist*, *21*(1), 54–63.

Stewart, R. R., Huddleston, P. D., & Kan, T. K. (1984). Seismic versus sonic velocities: A vertical seismic profiling study. *Geophysics*, *49*(8), 1153–1168. doi: 10.1190/1.1441745

Street, L.V., & Detar, R. E. (n.d.). *Geothermal investigations in idaho: Geothermal resource analysis in twin falls county, idaho.*

Tingay, M., Reinecker, J., & Müller, B. (2008). Borehole breakout and drilling-induced

fracture analysis from image logs: World stress map project guideline: Image logs. , 1–8.

U.S. Environmental Protection Agency. (2015). *Sole source aquifer protection program in epa region 10.* Retrieved from `http://yosemite.epa.gov/r10/water.nsf/Sole+Source+Aquifers/Overview/`

Wikipedia. (2010). *Snake river plain.* Retrieved from `http://de.wikipedia.org/wiki/Datei:Snake_river_plain.png`

Williams, J. H., & Johnson, C. D. (2004). Acoustic and optical borehole-wall imaging for fractured-rock aquifer studies. *Journal of Applied Geophysics*(55), 151–159.

Wood, S. H., & Clemens, D. M. (2002). Geologic and tectonic history of the western snake river plain, idaho and oregon. In *Bonnichsen, b., white, c.m., mccurry, m. (eds), tectonic and magmatic evolution of the snake river plain volcanic province: Idaho geological survey bulletin 30* (pp. 69–103).

Yilmaz, Ö. (2001). *Seismic data analysis: Processing, inversion, and interpretation of seismic data* (Second Edition ed.). Tulsa, Oklahoma: Society of Exploration Geophysicists.

Appendix

A ICDP-OSG Logging List

The following table gives a summary of the job report created during the borehole logging. It should be noted that this logging list has been sorted by log type and subsequently for file number and acquisition date. This table does not include erroneous loggings as they were pointed out in the job report. Furthermore, loggings with a downward logging direction were not included as they are not used for measurements.

Logging team: Christian Carnein, Jochem Kück, Matxalen Rey Abasolo, Martin Töpfer. VSP group (University of Alberta participants): Dr. Douglas Schmitt, Lucas Duerksen, Randy Kofman, Brendan deMilliano, Ross Bishop, Brendan Snow.

File Name	Log Type	Parameters	Acquisition Date	Start Depth (m)	End Depth (m)	Remarks
003	TS1-MP-DIP	Tmud,P, dipmeter	06/17/2011	1899	1610	Casing at 1130 m, Main
005				1609	1591	Main
006				1587	1153	Main
-	SlimWave^{TM} 4 Geophones	VSP Zero-Offset	06/18-06/19/2011	1870	10	tralala positions, seismic source: U of A Minivib^{TM}
-		VSP Walk-Away	06/19-06/20/2011	1866	262	Seismic source: U of A Minivib^{TM}
010	TS1-BS	Vp,Vs,FWS	06/19/2011	1600	1275	Main
011				1325	1275	Repeat
012				1280	1120	Main
029			06/22/2011	1900	1747	CAN error, new log
030				1800	1116	CAN error, 7.5m/min
046			06/24/2011	1131	968	
047				1032	627	Main
055	TS2-BS	Vp,Vs,FWS	06/24/2011	288	199	
056				288	206	
014	TS1-DLL	Resistivity	06/19/2011	1162	1128	Main/Repeat
015				1163	1125	Main/Repeat
021			06/21/2011	1903.9	1608.9	Main, Casing(HQ) at 1130 m, Casing(NQ) at 1621 m
022				1608.9	21.8	
026				1680	1164	Main, Casing(HQ) at 1130 m, Casing(NQ) at 1168 m
034			06/23/2011	1131	627	Main

File Name	Log Type	Parameters	Acquisition Date	Start Depth (m)	End Depth (m)	Remarks
017	TS1-SGR-MS	GR,K,Th, U,MSUS	06/19/2011	1164	1128	Repeat
018				1164	7	Main
019	TS1-MS	GR,MSUS	06/20/2011	1900	3	Main, Downward measurement, Casing(HQ) at 1130 m, Casing(NQ) at 1621 m
048			06/24/2011	271	250	Casing at 215 m
049				586	210	
023	TS2-MS	GR,MSUS	06/21/2011	0	1050	Downward measurement, Casing(HQ) at 1130 m, Casing(NQ) at 1621 m
024				1050	1680	Downward measurement
025				1680	-	
031			06/23/2011	3	1134	Downward measurement, Casing (HQ) at 637 m
032				1131	623	Main, GR(TS2)=1.16667 GR(TS1)
027	FAC40	Acoustic televiewer	06/22/2011	1150	1131	Casing(HQ) at 1130 m
028				1161	1130	
029				1160	1130	
045			06/23/2011	1130	636	
050			06/24/2011	284	280	
051				388	212	
035	TS1-DIP	CALI, orientation, dipmeter, FTOT	06/23/2011	601	-	stationary, caliper inside casing
036				1130	1082	Sonde stuck
039				1070	976	
041				696	640	
052			06/24/2011	260	240	
053				396	331	
054				326	210	
057				0	-	stationary, surface measurement of total magnetic field

Depth reference:	Top of pipe drive
Elevation reference above ground:	1.75 m
Type of fluid in hole:	Bentonite mud
1.Casing:	213 m
2.Casing(HQ=98 mm):	1130 m - varying
3.Casing(NQ=77 mm):	varying
Drilling method in open hole section:	Diamond Core Bit
Cable type/owner:	3/16" 4-conductor / GFZ
Winch type/owner:	MW2000 / GFZ

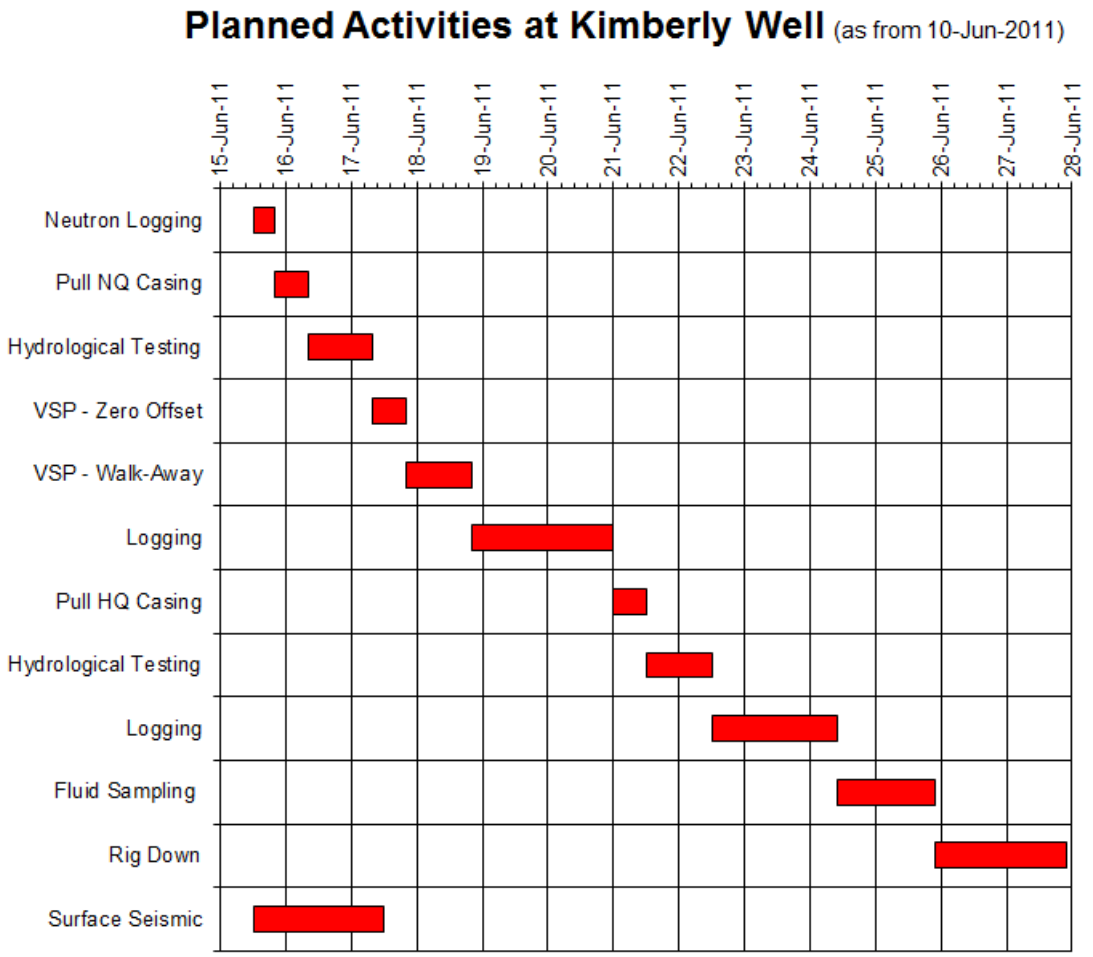

Fig. .1: Summary of borehole activities at the Kimberly drill site, as they were planned 10-June-2011

B Processing flows

These tables compile the used flow commands of the commercial processing software VISTA^{TM} for both zero-offset and walk-away VSP.

Vibroseis Correlation

Step	Process	Rationale	Flow commands in VISTA^{TM}
1	Load in zero-offset VSP		Input
2	Vibroseis Correlation	Correlate input trace stream with sweep Sweep Channel #:1 Sweep Length: 14000 ms	VibCorr
3	Output correlated traces		Output

Component Separation and Stacking

Step	Process	Rationale	Flow commands in VISTA^{TM}
1	Load in zero-offset VSP		Input
2	Data Selection	Data trace selection identifies the component of the geophone. The selection is made in 'Data/Header Selection spreadsheet' by Vertical component=TRACE_ID_Code=12 Horizontal components= TRACE_ID_Code=13 and TRACE_ID_Code=14	SelData
3	Stack traces at constant recording depth	Change the sort order to Main Sort Key=DEPTH_RECV	Sort Alter
4	Output separated and sorted VSP		Output

Wavefield Separation - Median Filter

Step	Process	Rationale	Flow commands in VISTA™
1	Input Data	Vertical stacked component	Input
2	Apply f-k filter	Remove harmonic noise below and above source signal frequencies Load in f-k filter file created from f-k Spectrum Design Window	FK_Filter
3	Apply bandpass	Bandpass (20-25-45-50) to enhance first arrival	OrmsbyBP
4	Flatten to header event	Vertical component is flattened to 200 ms, whereas the header event is DATA_FIRSTBREAK	Flatten
5	Apply windowed scale to first arrivals	Apply a constant value of the header value DATA_MAXAMPLITUDE to equalize amplitudes, scaling is a requirement for the application of the median filter	Apply Constant Value
6	Apply median filter	Set to a median filter with 29 points (traces) to compute the downgoing pulse, signal enhancement	Alpha trim mean (ATM) Filter
7	Output downgoing wavefield	Flattened Downgoing (-TT)	Output
8	Substract result of step 6 from result of step 5	Substract the downgoing wavefield from the upgoing wavefield	SubInput
9	Apply median filter	Set to a median filter with 9 points (traces) to enhance the upgoing wavefield	Alpha trim mean (ATM) filter
10	Output upgoing wavefield	Flattened Upgoing (-TT)	Output

Statics Removal - Time shift back to original times

Step	Process	Rationale	Flow commands in VISTA™
1	Input Data	Restore flattened Upgoing (-TT) or Downgoing (-TT) data	Input
2	Mute data traces	Mute by Header value VWUSER_3=200 ms	MuteTrc
3	Flatten to header event	The selected header value VWUSER_1=DATA_FIRSTBREAK - VWUSER_3 has been flattened to 0 ms.	Flatten
4	Apply a bulk shift static	Apply a time shift that is approximately the same as the firstbreak times to all traces of the data set. Time static: -140 ms Negative Shift for Upward Static	BulkShift
5	Flatten to header event	The selected header value VWUSER_2=DATA_FIRSTBREAK - 140 ms has been flattened to 0 ms.	Flatten
6	Output Pseudo-Two-Way-Travel time vertical component	Upgoing (TT) or Downgoing (TT)	Output

Corridor Stack

Step	Process	Rationale	Flow commands in VISTA™
1	Input Data	Median filtered Upgoing (TT) data	Input
2	Mute data traces	Apply a Bottom Mute Header for Outside Corridor Stack with the value of VWUSER_4=2*VWUSER_2 + 100 ms. Apply a Top Mute Header for Inside Corridor Stack with the value of VWUSER_4. For the Full Corridor Stack no muting is required.	MuteTrc
3	VSP Stack	Stacking all traces of corridor muted upgoing wavefield Replicate Output Traces: 10	VSPStk
4	Output Corridor Stack	Output Inside and Outside as well as Full Corridor Stack	Output

Stacking and Component Separation of Walk-Away VSP data

Step	Process	Rationale	Flow commands in VISTA™
1	Load in walk-away VSP data for every receiver chain		Input
2	Sort traces for constant shot point number	Change the sort order to Main Sort Key=SHOT_POINT_NO	SortAlter
3	Common header stack	Stacking traces received in sorted order and normalized by 1/(N+X).	HeadStk
4	Data Selection	Data trace selection identifies the component of the geophone. The selection is made in 'Data/Header Selection spreadsheet' by Vertical component=TRACE_ID_Code=12 Horizontal components= TRACE_ID_Code=13 and TRACE_ID_Code=14	SelData
5	Sort stacked and separated data	Change the sort order to Main Sort Key=CHANNEL_NO	SortAlter
6	Output stacked and sorted components of walk-away VSP data	Raw Vertical, Raw X, Raw Y for every depth of the receiver chain	Output

Eidesstattliche Erklärung

Ich versichere, dass ich diese Arbeit selbstständig verfasst und keine anderen Hilfsmittel als die angegebenen benutzt habe. Die Stellen der Arbeit, die anderen Werken dem Wortlaut oder dem Sinn nach entnommen sind, habe ich in jedem einzelnen Fall unter Angabe der Quelle als Entlehnung kenntlich gemacht. Diese Versicherung bezieht sich auch auf die bildlichen Darstellungen.

3rd December 2015 Franziska Naumann

Declaration

I hereby declare that I completed this work without any improper help from a third party and without using any aids other than those cited. All ideas derived directly or indirectly from other sources are identified as such. This declaration also refers to the representation of figures and visual material.

3rd December 2015 Franziska Naumann